Doctoral Dissertation
Doctoral Program in Mechanical Engineering (36th Cycle)

Pyroshock Testing

A Theoretical and Experimental Investigation for the Qualification of Aerospace Equipment

By

Luca Viale

******

Supervisor(s):
Prof. Alessandro Fasana, Supervisor

Doctoral Examination Committee:
Prof. Marco Cammalleri, Referee, University of Palermo
Prof. Walter D'Ambrogio, Referee, University of L'Aquila

Politecnico di Torino
2024

Declaration

I hereby declare that the contents and organization of this dissertation constitute my own original work and does not compromise in any way the rights of third parties, including those relating to the security of personal data.

Luca Viale

Turin, May 20, 2024

* This dissertation is presented in partial fulfillment of the requirements for **Ph.D. degree** in the Graduate School of Politecnico di Torino (ScuDo).

To my family

Acknowledgments

My doctoral journey and this resulting work would not have been possible without the many people who have supported me over the years. I am sincerely grateful for their invaluable assistance throughout the course of my doctoral research.

First and foremost, I am deeply thankful to my supervisor, Prof. Alessandro Fasana, for his guidance, encouragement, and unwavering support. His expertise, insightful feedback, and mentorship have been fundamental during these years and in shaping this thesis. Along with Prof. Luigi Garibaldi and Prof. Stefano Marchesiello, they have been both professional and human role models, welcoming me and fostering my passion for this work.

I express my sincere gratitude to Prof. Gunnar Tibert, his research group, and the technical staff at KTH for hosting me and supporting me during part of this journey.

I am also indebted to Prof. Marco Cammalleri and Prof. Walter D'Ambrogio for their constructive feedback on this thesis.

I am grateful to my colleagues, who are above all friends. In addition to their intellectual exchange and encouragement, they provide me with affection, joy and support every day. A special thanks to Alessandro for his constant companionship and assistance.

I am deeply thankful to my friends, relatives, and all the people I hold dear, who have been close to me despite the distance, and in some cases, are no longer with me. Thank you for your support, understanding, and encouragement during the ups and downs.

Last but certainly not least, a heartfelt thank you to my family. Thank you for your unconditional love, the values you have instilled in me, your sacrifices, your unwavering belief in me, and for being role models and a constant example to me.

Abstract

Spacecraft and associated onboard equipment undergo substantial dynamic loading during various mission phases. The activation of pyrotechnic devices induces severe high-frequency shocks transmitted throughout the entire structure, also known as "pyroshocks". These shocks could potentially lead to mission failure and inflict safety-critical damages. Consequently, verification tests for aerospace equipment are necessary to prove the resistance of the equipment to impulsive loads.

Qualification requirements are typically expressed in terms of the shock response spectrum acceleration, and they can easily vary since distinct launch vehicles induce different shock response spectrum profiles. Laboratory tests thus aim to replicate real conditions of a shock environment while ensuring repeatability and safety. To achieve this, the majority of test facilities often exploit impacting objects (e.g., hammers or projectiles) launched onto resonant plates, which in turn support the component under examination.

Recent studies have increasingly focused on developing numerical analyses to predict the shock responses of these structures. Currently, the calibration process relies on empirical techniques causing substantial costs and downtime. This PhD thesis delineates several objectives, aiming to introduce innovative approaches to pyroshock testing from both theoretical and experimental perspectives. In addition to an initial literature review that entirely describes the state of the art, the main contributions of this work are outlined below.

Firstly, a novel approach developed in the frequency domain has been introduced. On this basis, effective parametric models have been developed both for the simulation of pyroshock tests and for the optimization of the design of test facilities. These models demonstrate notable accuracy and flexibility, effortlessly and efficiently satisfying the variable SRS requirements. This operational efficiency

translates into reduced calibration times, entailing significant economic benefits. The proposed models exhibit varying degrees of complexity and computation times. They range from a multi-degree of freedom system model to the implementation of an embedded computer-aided design modeler, integrated with a finite element solver, and a genetic algorithm optimizer. Insights into contact mechanics for defining impulses and various optimizations to enhance test performance are encompassed.

Secondly, an extensive dataset has been gathered to facilitate a comprehensive exploration of parameters in shock tests employing a resonant plate. These data were acquired at the Marcus Wallenberg Laboratory for Sound and Vibration Research (MWL) in collaboration with the KTH Royal Institute of Technology. This dataset has enabled an investigation into the influence of experimental configurations on test outcomes, specifically in terms of the shock response spectrum. Furthermore, these data have been crucial in validating predictive models employing a digital twin. The research incorporates an in-depth analysis of shock physics, involving a comparative assessment between simulated and measured force profiles. This comparative study provides valuable insights into the complexities of shock dynamics.

Finally, the last contribution concerns the design and development of the Politecnico di Torino test facility. Taking advantage of the developed models and acquired knowledge, a specialized test facility for conducting pyroshock tests with resonant plates has been successfully designed. The key components of this test facility include a structural portal frame to uphold the resonant plate and an excitation apparatus, which can take the form of either a pneumatic gun or a pendulum. This test facility stands as the application of the outcomes of the previous research, allowing the controlled experimental simulation of pyroshock tests.

Contents

List of Figures

List of Tables

List of Acronyms

ADC	Analog to Digital Converter
BC	Boundary Condition
CAD	Computer-Aided Design
COR	Coefficient Of Restitution
DFT	Discrete Fourier Transform
DOE	Design Of Experiments
FE(A)	Finite Element (Analysis)
FE(M)	Finite Element (Method)
(F)FT	(Fast) Fourier Transform
FOS	Factor Of Safety
FRF	Frequency Response Function
GA	Genetic Algorithms
I(F)FT	Inverse (Fast) Fourier Transform
IIR	Infinite Impulse Response
IP	In-Plane
IRF	Impulse Response Function
MAE	Mean Absolute Error
MALE	Mean Absolute Logarithmic Error
MAPE	Mean Absolute Percentage Error
MDOF	Multi-Degree-Of-Freedom
ML	Machine Learning
MSE	Mean Square Error
OFAT	One-Factor-at-A-Time
OOP	Out-Of-Plane
RMSE	Root Mean Square Error
RMSLE	Root Mean Squared Logarithmic Error
SDOF	Single-Degree-Of-Freedom
SEA	Statistical Energy Analysis

SMAPE	Symmetric Mean Absolute Percentage Error
SF	Safety Factor
SRS	Shock Response Spectrum
TSEA	Transient Statistical Energy Analysis
VMSS	Virtual Mode Synthesis and Simulation

Nomenclature

The following conventions for nomenclature are embraced, unless explicitly stated otherwise:

- Matrices and vectors are denoted in boldface.
- Matrices are represented by capital letters, while vectors use lowercase letters.
- Signals in the time domain are indicated by lowercase letters, while their frequency-domain equivalents are denoted by the corresponding capital letters.

Specific symbols are defined within each chapter. Commonly adopted symbols:

c	Damping coefficient
d	Diameter
dt	Time resolution
$df, d\omega$	Frequency resolution
e	Coefficient of restitution
E	Young's modulus
$f(t), F(\omega)$	Force
$F^*(\omega)$	Force with unitary momentum
f_s	Sampling frequency
G	Shear modulus
$h(t)$	Impulse response
H	Mesh dimension
I	Moment of inertia
k	Stiffness
m	Mass
n, N	Number of elements
p	Momentum
Q	Damping ratio

R	Radius of curvature
t	Time
T	Transmissibility
u	Velocity
W	Energy
$x(t), X(\omega)$	Displacement, position
$\dot{x}(t), \dot{X}(\omega)$	Velocity
$\ddot{x}(t), \ddot{X}(\omega)$	Acceleration
α	Receptance
Δp	Change of momentum
Δt	Time interval
ζ	Damping ratio
$\theta, \dot{\theta}, \ddot{\theta}$	Angular position, velocity, and acceleration
λ	Wavelength
μ	Friction coefficient
ν	Poisson's ratio
ρ	Density
σ	Yield stress
τ	Pulse duration
ω	Frequency
Ω	Excitation frequency
Ω_c	Natural frequency of the c-th SDOF in the SRS calculation
$\bullet_i$	Subscript referring to the anvil plate (input)
$\bullet_{min}$	Subscript indicating the minimum
$\bullet_{MAX}$	Subscript indicating the maximum
$\bullet_p$	Subscript referring to the resonant plate
$\bullet_s$	Subscript referring to the impacting body
$\bullet_{SRS}$	Subscript indicating the SRS
$\bullet_{\%}$	Subscript referring to percentage indicators

Chapter 1

Introduction

In the aerospace and defense fields, pyrotechnic devices, employing high-energy or explosive materials, play a pivotal role in executing crucial mechanical functions. These devices are essential in initiating flight sequences during missions, enabling the release of different spacecraft stages, boosters, cargo satellites, separation of structural subsystems, and deployment of various attachments. However, the activation of explosive charges or pyrotechnic devices in general induces a transient mechanical response in structural elements, especially in the proximity to the energy release zone. This phenomenon, commonly referred to as pyrotechnic shock or pyroshock, is distinguished by its impulsive nature and high-frequency response content. These characteristic pyroshocks often lead to damages to electronic components but infrequently result in structural failures. Indeed, crystalline and ceramic materials, prevalent in optical and electronic systems, exhibit an high sensitivity to excitations within the 2-4 kHz frequencies band [1]. Damages to these materials can result in the failure of space missions. Hence, experimental simulations of pyroshocks are fundamental for characterizing and verifying components in order to ensure the reliability and functionality of aerospace and defense equipment.

The selection of methods and excitation structures for simulating shocks depends on the specific type of shock to be replicated, on test requirements, and on other influencing factors. Among these methods, resonant plates subjected to impact from typically metallic objects, such as pendulum, hammer, dropping mass, projectile, or actuator, stand out as the most widely adopted and efficient test rigs for pyroshock simulation. This approach improves the effectiveness of more

restrictive methods like electrodynamic shakers and even presents some advantages with respect to pyrotechnic devices themselves. Resonant plates provide a flexible solution, exposing the object under test to mid- and far-field shocks. The generation of effects similar to the stresses induced by a pyroshock makes resonant plates a superior choice for achieving realistic and comprehensive simulations.

1.1 Objectives

Despite the growing interest in the pyroshock topic, numerous aspects require further investigation. A systematic analysis of the literature revealed a few studies focusing on both numerical and experimental simulation of pyroshocks. Nevertheless, many techniques for simulating pyroshocks still require extensive trial-and-error processes to achieve accurate test conditions and the desired Shock Response Spectrum (SRS) profile [2,3]. In addition to the inherent technical challenges associated with plate tuning, it is necessary to remember that test requirements may vary based on the specific characteristics of the pyroshock to simulate. The combination of these factors requires a significant effort in tuning and preparing the experimental setup, consequently increasing downtime and costs.

In this context, standards provide guidelines and specifications for reliably and repeatably conducting pyroshock tests. However, nowadays there is no standardized procedure for executing the tests and predicting the effects caused by shocks. Experimentally, most studies in the literature utilize a plate as a resonant fixture to simulate the pyroshock environment. Nevertheless, numerous parameters influencing the test results remain complex and challenging to manage. These include the geometry, dimensions, and material of the resonant fixture, impact and measurement locations, excitation typology, mass, velocity, geometry, and material of the impacting body. Concerning numerical simulation, the state-of-the-art appears less defined compared to the experimental field. Indeed, various approaches exist, primarily classified into Finite Element-based (FE) models and Statistical Energy Analysis (SEA). Methods belonging to the former category are typically developed in the time domain, extracting the transient response of the mechanical system to the impulse. On the other hand, the latter category usually involves frequency domain approaches.

For all these reasons, this PhD thesis encompasses several objectives. In addition to providing an overview of the field of pyroshock simulation and analyzing recent studies on this topic, this thesis aims to propose new approaches in both numerical and experimental simulation. Numerical methods have been developed

mainly in the frequency domain. The mechanical system was developed with popular computational models for structures, such as Multi-Degree of Freedom (MDOF) or FE models. This approach allows for reaching accurate results while maintaining short computation times. These numerical models prove to be essential for setting up the experimental apparatus, eliminating the need for numerous trial-and-error iterations and, consequently, reducing costs and downtime. Beyond predicting the SRS, these numerical methods have been adapted to address the so-called inverse problem, i.e., the optimal design of the experimental test bench. The results of this optimization process are highly beneficial for defining and designing an experimental test facility. With these outcomes and the collection of a full factorial dataset for an in-depth investigation of impact tests, it became feasible to design a test facility to be installed at the Politecnico di Torino.

In summary, the main objectives and original contributions of this thesis can be grouped into:

- Novel numerical models for simulating pyroshock tests and for predicting the SRS. These proposed approaches originally contribute to the existing literature, providing significant advantages in terms of accuracy, shortened computation times, and cost reduction through efficient tuning.
- Proposal of numerical models, currently absent in the literature, to optimally design test benches for experimental pyroshock simulation.
- Collection of a dataset containing impact tests in various experimental configurations, allowing not only the validation of numerical models but also the investigation of parameter effects.
- Proposal of a test facility for experimental pyroshock simulation, contributing to the establishment of a specialized laboratory at the Politecnico di Torino.

1.2 Outline

The present thesis is structured as follows.

In Chapter 2 a general overview of pyroshocks is presented. The definition of impulsive phenomena and the classification of shocks is introduced to the reader. Furthermore, the SRS is presented: SRS is the most commonly used representation to describe the frequency contents of shocks and the main tool that will be used in this thesis to analyze the results.

In Chapter 3 a state-of-the-art is proposed to survey the scientific literature. In particular, studies inherent to simulation models and experimental setups are gathered, given that this thesis deals with the pyroshock phenomenon both from an analytical, numerical, and experimental point of view. Finally, a reference to the state of the art in the field of contact theory is proposed.

In Chapter 4 a novel semi-analytical model to describe pyroshock tests entirely in the frequency domain is proposed. Together with this first approach, useful for subsequent numerical models, an in-depth analysis of the convolutional method is also presented.

In Chapter 5 all the numerical models developed for the simulation of pyroshock tests are reported, from the more straightforward MDOF model to the more comprehensive FE-based model. In addition to the description of these models and of their numerous parameters, their validation through a comparison with experimental data is presented.

In Chapter 6 the developed pyroshock simulation methods are exploited to solve the inverse problem, i.e. the design and optimization of the experimental setup. In particular, optimization techniques by means of Genetic Algorithms (GA) are proposed for the plate design together with investigations on the influence of shape, dimensions, and measurement-impact positions on the results in terms of SRS acceleration.

In Chapter 7 a large dataset is proposed to allow a full parameters exploration of shock tests with a resonant plate. Data were acquired at the Marcus Wallenberg Laboratory (MWL) for sound and vibration research of the KTH Royal Institute of Technology, during a collaboration under the supervision of Prof. Gunnar Tibert. In addition to a detailed description of this dataset, an analysis of the influence of the experimental configurations, further validation of the predictive model, and an in-depth analysis of the shock physics are presented.

In Chapter 8 the design of a system for the experimental simulation of pyroshock proposed in the laboratories of the Politecnico di Torino is mentioned.

In Chapter 9 conclusions are drawn. The main contributions of this doctoral thesis are also included, together with the directions for future developments.

Chapter 2

Pyroshock: A General Overview

Throughout their operational lifespan, space equipment is subjected to various types of loads, including high-frequency shocks [4]. In particular, pyrotechnic devices find common applications in aerospace, utilizing high-energy or explosive materials, hence earning the name “pyroshock”. These devices play a crucial role in executing essential mechanical functions, facilitating the initiation of flight sequences across different mission phases, such as launch, orbit, and return.

Pyrotechnic devices are also fundamental in tasks like releasing spacecraft stages, boosters, cabins, satellites, and other structural subsystems. Their utilization offers several advantages, ensuring satisfactory efficiency, high reliability, and the proper connection of structures before separation. However, the activation of pyrotechnic devices induces a transient mechanical response in the structural elements in proximity to the explosion or energy release area. This phenomenon is characterized by its brief duration, high amplitude values of acceleration response, and substantial high-frequency content [5]. Given these characteristics, coupled with the strategies of launch vehicle manufacturers aiming to minimize spacecraft mass and associated costs by reducing damping materials, pyroshocks can lead to deformations and damage to the structure. Electronic components and precision equipment, particularly those comprising crystalline and ceramic materials, are vulnerable to these shocks. As safety-critical elements for space missions, these materials are highly sensitive to both shocks and high-frequency excitations [1].

For these reasons, it is necessary to subject space equipment to shock tests for qualification, ensuring its resistance against induced stresses. Moreover, with the rapid technological progress in the aerospace and defense industry and the continuous evolution of spacecrafts, missions now incorporate an increasing array of diverse pyrotechnic devices. This amplifies the significance of validation testing, making it an indispensable tool in the aerospace equipment qualification process.

The primary methodologies employed for characterizing and verifying components involve experimental simulations of pyroshocks. Traditionally, these simulations relied on explosive charges. However, present laboratory settings commonly utilize bullets, pendulums, or hammers in impact testing machines to enhance repeatability and safety. Among the diverse excitation methods and structures, resonant plates emerge as the most widely used and effective means of simulating pyroshocks. These plates enable the exposure of the object under test to responses similar to those generated by a real pyroshock.

The shocks, induced by the impact of a typically metallic object on the resonant plate, necessitate the generation of a spectrum capable of satisfying the specified test requirements. Numerous technical standards, such as Method 517 in MIL-STD-810F [6] and the IEST RP Pyroshock Testing Technique [7], offer guidelines for delineating these requirements. This study specifically complies with the 7003 standards presented by NASA [8].

Shocks are typically measured through a time-domain acceleration signal. However, interpreting their time histories leads to challenges in trying to quantify, classify, and compare various impulses. Consequently, the SRS [9] serves as the prevalent tool for characterizing and comparing the frequency contents of pyroshock tests. It also describes the specifications of impact tests within the aerospace industry, although alternative methods have been proposed for component shock qualification [10]. The maxi-max SRS is adopted in most cases, denoting the absolute maximum response in terms of acceleration. This is measured according to a standardized set of mass-spring-damper systems with a Single Degree Of Freedom (SDOF) each. These systems are synchronized at natural frequencies to achieve a frequency resolution of 1/24 octave, accompanied by a damping coefficient $\zeta_{SRS} = 0.05$. Pertinent details on the SRS will be described in Subsection 2.2.

The previously mentioned guidelines generally facilitate the definition of requirements for pyroshock simulations in terms of SRS with associated tolerance limits. These requirements typically depend on the three most critical frequencies:

the minimum and maximum frequencies (around 100 Hz and 10 kHz, respectively) and the knee frequency (usually falling between 500-1500 Hz). Test specification curves often exhibit amplitudes characterized by a positive slope at low frequencies, followed by an approximately constant level at higher frequencies, as shown in Figure 1. The amplitude values are determined based on the structural characteristics of the spacecraft and the nature of the explosions. These levels may vary even for the same launch system by changing the mounting position of the equipment with respect to the launcher. In the literature, there exist additional guidelines concerning the definition of tolerances, such as the experimental standard ESA ECSS [11]. The ECSS-E-ST-10-03C specifically limits the SRS within a tolerance range spanning +6 dB to -3 dB relative to the nominal spectrum.

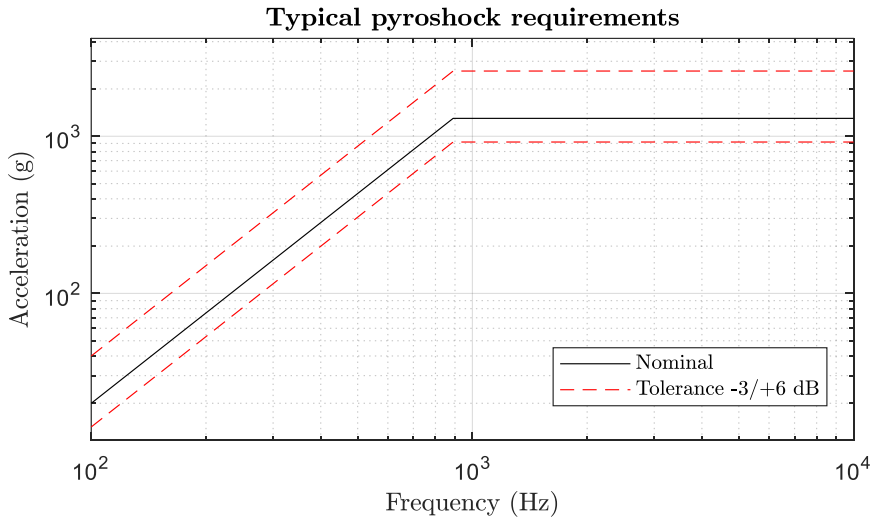

Figure 1. Typical pyroshock requirements qualitatively defined according to the guidelines depicted by the standards and taking into account the constitutive spacecraft characteristics.

Nowadays, the predominant approach for achieving the correct test conditions and the desired SRS profile in pyroshock simulation techniques primarily involves defining the experimental setup through empirical methods, requiring a substantial amount of trial-and-error iterations [2,3]. It is worth noting that the diverse experimental configurations employing resonant plates vary significantly. Factors such as dimensions, materials, orientation, and boundary conditions of the plate, together with numerous parameters inherent to other elements in the experimental system (including the impacting body and the object under test), contribute to this variation. Introducing an anvil plate may also be considered to modify impact characteristics and prevent plastic deformation of the resonant plate. The challenges in establishing

qualification tests using trial-and-error techniques are further complicated by the many combinations of involved parameters. In addition to these purely technical complexities associated with test tuning, test requirements may vary based on spacecraft construction characteristics and the specific pyroshock attributes to simulate. The combination of all these factors results in a substantial burden in terms of downtime and costs for the preparing and tuning the test facility.

2.1 Pyroshock Definition

A shock is a localized, transient mechanical impact characterized by its brevity, high frequency, and considerable amplitude, presenting a prominent initial slope. The shock propagation is exhibited through tension-compression, flexural, or shear waves, involving complex phenomena like reflection, dissipation, and diffraction at boundary conditions or mechanical disjunctions. The rapid attenuation of high-frequency waves, attributable to damping in materials and dissipation in joints, makes these waves more noticeable at the origin of the shock measurement time history and near the shock source. Waves are subjected to reflection at boundary conditions and internal interfaces, generating a modal response within the system. On the contrary, longer wavelength responses may propagate at various points within the structure, even far from the origin of the shock.

Several factors characterize the peculiar nature of these acceleration transients: (1) the nature of the pyrotechnic source, (2) the structure's geometry and properties, and (3) the distance from the source. In this regard, several technical standards provide guidelines for determining test requirements. Method 517 in MIL-STD-810F [6] and the IEST RP Pyroshock Testing Technique [7] are mentioned among the best known and used standards. For instance, NASA-STD-7003 [8] classifies pyroshocks in three categories based on the distance between the source and the point of interest. These categories are characterized by different spectral contents and are defined as follows:

- *Near-field*: characterized by a relevant spectral content reaching frequencies higher than 10 kHz and peak accelerations above 10^5 g. For good practice, sensitive hardware should ideally be situated at a considerable distance from potential shock zones during the design phase. Consequently, the requirements for simulation tests primarily emphasize the mid- and far-field categories;
- *Mid-field*: the frequency band interested by the mid-field shocks is included in the range 3-10 kHz with accelerations of the magnitude order

of 10^4 g. The mid-field content is mainly caused by wave propagation and structural resonances;

- *Far-field*: it regards frequencies below 3 kHz and accelerations with peak values lower than 10^3 g, caused by structural resonances.

In accordance with the outlined guiding principles, simulations are conducted to straightforwardly derive a three-point SRS alongside associated tolerance limits. These three points are typically defined by the three most critical frequencies: the minimum, maximum, and knee frequencies. As illustrated in Figure 1, test specifications typically exhibit amplitudes with a positive slope at low frequencies, succeeded by a constant level at higher frequencies. Amplitude values, in the range of 10^2 to 10^3 g, vary depending on spacecraft construction characteristics, explosion types, and equipment positioning. The literature provides guidelines for tolerance selection, often referring to the ESA ECSS experimental standard [11]. This standard restricts the SRS within a tolerance range of +6 dB to -3 dB relative to the nominal spectrum.

2.2 Shock Response Spectrum

The way a system responds to a shock is often described as the time history of a parameter that reflects the system's motion. Nevertheless, a shock measurement presented as a time history is not immediately applicable for engineering purposes, such as comparing shock severities, evaluating frequency contents, or understanding its effect on components. In the case of a simple system, the magnitudes of response peaks can be summarized as a function of its natural frequency at a particular level of damping. This specific representation is commonly known as SRS.

The SRS is employed to characterize a standardized dynamical system's response to a shock. This computational tool proves to be fundamental in estimating the severity or potential damage caused by a shock. Consequently, the SRS facilitates the comparison of diverse shocks and establishes equivalence criteria between a measured transient environment and a laboratory-simulated counterpart. The methodology involves applying a time history as a base excitation to an array of SDOF systems. Subsequently, the temporal maximum response is calculated for each SDOF, providing a comprehensive understanding of the shock's impact. It is worth noting that the SRS can be defined for various input or response parameters, such as displacement, velocity, or acceleration. In aerospace applications, the input transient is typically defined in terms of acceleration. Each SDOF's natural frequency (Ω_c) is treated as an independent variable in the calculation, with a

conventionally assumed consistent damping value (5%) for every SDOF. The versatility of the shock response spectrum calculation allows for the use of any unique set of natural frequencies, although a typical approach involves a bandwidth division, such as 1/24 octave.

It is worth noting that the computation of the SRS exhibits nonlinearity and non-bijectivity. Specifically, the SRS of the sum of time signals does not correspond to the sum of the SRS computed on individual time signals, indicating a nonlinear relationship. Additionally, this non-bijective nature results in the definitive loss of certain information, such as phase or effective duration details. These characteristics highlight the limitations of the SRS tool. Moreover, real systems deviate from the standardized system, introducing complexities. Damage manifestation may be attributed to eigenmode amplification, further complicating the comprehensive representation of the signal frequency content. These discrepancies highlight the need for a correct interpretation of SRS outcomes and the weaknesses in describing completely the dynamics of real-world scenarios [12].

There exist different manners to compute the SRS. The standard ISO 18431 [13] describes methods for the digital calculation of a SRS, starting from an accelerometric signal and using digital filters. Indeed, several methods in the time domain can be employed to obtain the time response of a mechanical system to a generic excitation, including the Duhamel integral, also known as the convolution integral. This method is well-established in the literature but entails a high computational burden. However, the convolution integral can be employed to derive a recursive algorithm, such as a digital filter, leading to a computationally convenient solution.

Digital models of analog filters and other continuous systems are valuable in situations aiming to duplicate or replace the continuous system with an equivalent discrete system. The accuracy of the model is measured in terms of the error resulting from the discretization of the continuous signal. It is generally assumed that Analog-to-Digital Converters (ADCs) produce impulse samples at synchronized time points. Depending on the adopted model, discretization errors can vary under the same specified input conditions. It is challenging to assert which model provides maximum overall accuracy, as it depends on multiple factors such as the type of input signal and the sampling frequency. In [14], some methods for simulating continuous transfer functions are compared to demonstrate their quality. The most well-known models include the impulse invariant, step invariant, and ramp invariant methods.

Initially, most calculations to derive the SRS were based on the impulse invariant digital filter. To mitigate the significant aliasing associated with this method, David Smallwood [15] suggested the alternative use of a ramp-invariant digital filter in 1981. In several studies [16–18], Ahlin provided an overview of using digital filters to simulate the forced response of mechanical systems, leading to the definition of the digital filter proposed by the ISO 18431 standard. The filter coefficients for various types of shock-response spectra are provided, along with recommendations for an appropriate sampling frequency. The impulse invariant and ramp invariant filters belong to a family of filters based on the convolution integral. The convolution integral of the response to a given acceleration $\ddot{x}(t)$ of a set of independent SDOF mass-damper-spring oscillators (representing the SRS definition, as schematized in Figure 2), basing on their impulse response $h(t)$. Considering that the acceleration response of each SDOF system is $\ddot{x}_{SRS}^{\Omega_c}(t)$ in the definition of SRS calculation, the generic convolution integral may be expressed as:

$$\ddot{x}_{SRS}^{\Omega_c}(t) = \int_0^t \ddot{x}(\tau) \cdot h(t-\tau)\, d\tau \tag{1}$$

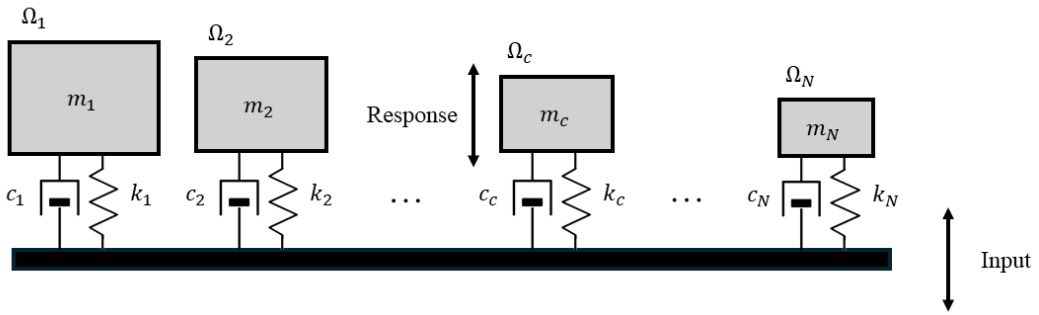

Figure 2. Representation of the array of independent SDOF mass-damper-spring systems defined for the SRS computation.

The convolution integral is subsequently converted into a series due to the digitized nature of the data. Moreover, this series undergoes transformation into a digital recursive filtering relationship to enhance computational efficiency. The ISO 18431 standard initiates the process from the SDOF system transfer function $G(s)$ to derive the filter coefficients. The Laplace transfer function is expressed as follows:

$$G(s) = \frac{a_2(s)}{a_1(s)} = \frac{cs + k}{ms^2 + cs + k} \tag{2}$$

where $a_1(s)$ and $a_2(s)$ are the given and the response accelerations, respectively. The corresponding digital filter can be derived from this transfer function by considering different sampling methods. These methods enable the transformation of a continuous-time signal into a discrete-time signal. In general, approximating continuous signals in a discrete domain can be understood as a convolution between the signal and specific kernel functions. The most well-known methods and their respective kernel functions are illustrated in Figure 3.

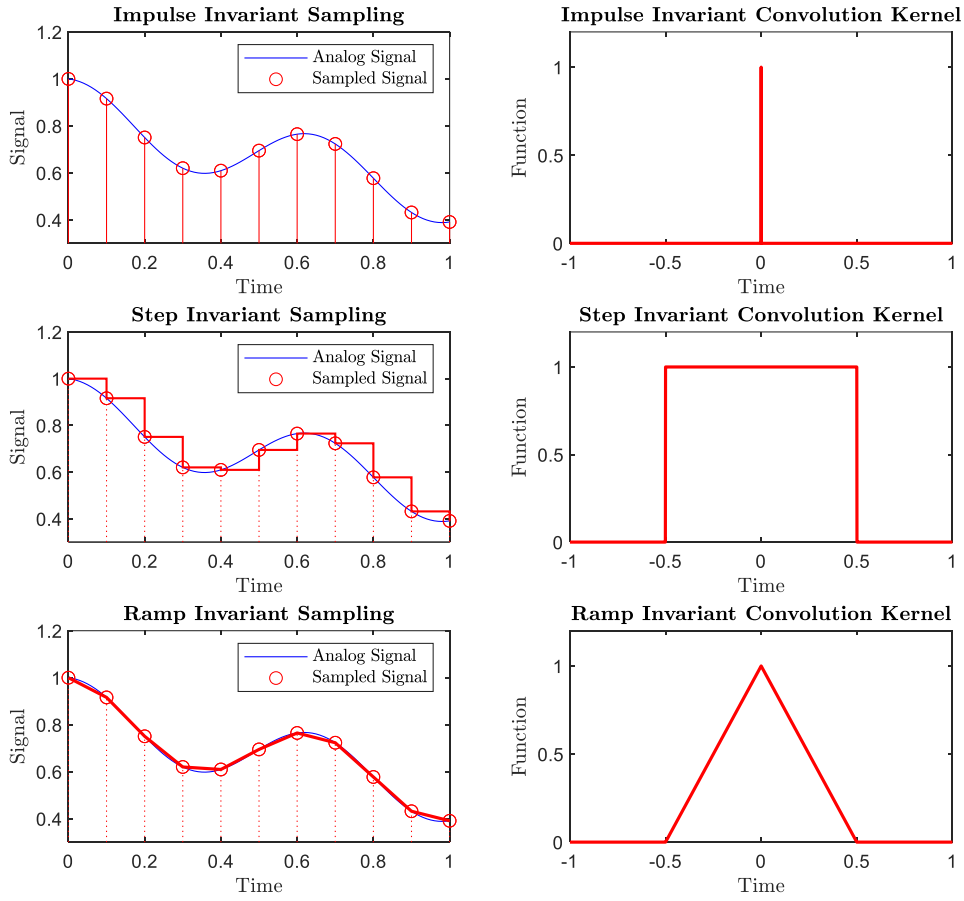

Figure 3. Different methods to approximate an analog signal in a sampling time step and related convolution kernels for different digital filters.

However, this method introduces frequency distortion, as the infinite frequency interval of the continuous system is mapped onto the finite frequency interval of the discrete system [19]. Indeed, despite the presence of anti-aliasing low-pass filters, it is impossible to completely avoid aliasing, which is the phenomenon whereby multiple analog signals can correspond to the same sampled signal, making them indistinguishable. Hence, since a signal requires a sampling process to be discretized, any sampled signal contains aliasing. However, the choice of a proper kernel function for signal sampling might reduce, or rather, convert the aliasing error. Specifically, convolving the signal with kernel functions in the time domain corresponds to multiplying their respective spectra in the frequency domain. The Fourier transforms of the different kernel functions determine whether the obtained bias and phase errors are more or less beneficial depending on the specific application. For the case under analysis, namely the response of mechanical systems to shocks, the approximation called the ramp invariant method [17,20] has been proved to be the best way to mitigate the frequency distortion. This is the reason why the ISO 18431-4 Standard adopts the ramp invariant method. This method, initially proposed by Smallwood [21] and re-elaborated by Ahlin, was preferred to the previous Kelly-Richman method [22], which is impulse invariant. Thus, the digital filters recommended by the ISO 18431-4 Standard to replace Eq. (2) adopt a second-order Infinite Impulse Response (IIR) filter, expressed by the following general Z-transform expression:

$$H(z) = \frac{\beta_0 + \beta_1 \cdot z^{-1} + \beta_2 \cdot z^{-2}}{1 + \alpha_1 \cdot z^{-1} + \alpha_2 \cdot z^{-2}} \tag{3}$$

where the filter coefficients for absolute acceleration response are defined as:

$$\beta_0 = 1 - e^{-\frac{\omega_n T}{2Q}} \cdot \frac{\sin\left(\omega_n \Delta t \sqrt{1 - \frac{1}{4Q^2}}\right)}{\omega_n \Delta t \sqrt{1 - \frac{1}{4Q^2}}} \tag{4}$$

$$\beta_1 = 2e^{-\frac{\omega_n \Delta t}{2Q}} \cdot \left[\frac{\sin\left(\omega_n \Delta t \sqrt{1 - \frac{1}{4Q^2}}\right)}{\omega_n \Delta t \sqrt{1 - \frac{1}{4Q^2}}} - \cos\left(\omega_n \Delta t \sqrt{1 - \frac{1}{4Q^2}}\right) \right] \tag{5}$$

$$\beta_2 = e^{-2\frac{\omega_n \Delta t}{2Q}} - e^{-\frac{\omega_n \Delta t}{2Q}} \cdot \frac{\sin\left(\omega_n \Delta t \sqrt{1 - \frac{1}{4Q^2}}\right)}{\omega_n \Delta t \sqrt{1 - \frac{1}{4Q^2}}} \tag{6}$$

$$\alpha_1 = -2e^{-\frac{\omega_n \Delta t}{2Q}} \cdot \cos\left(\omega_n \Delta t \sqrt{1 - \frac{1}{4Q^2}}\right) \tag{7}$$

$$\alpha_2 = e^{-2\frac{\omega_n \Delta t}{2Q}} \tag{8}$$

where $\omega_n = \sqrt{\frac{k}{m}}$ is the undamped natural frequency of a single SDOF system, $\omega_d = \omega_n \sqrt{1 - \zeta^2}$ is the damped natural frequency where ζ is the assigned damping coefficient, $\Delta t = \frac{1}{f_s}$ is the sampling time interval, and $Q = \frac{1}{2\zeta}$ is the damping ratio.

Chapter 3

Literature Analysis: The State of the Art

In the aerospace field, pyrotechnic devices are classified as high-energy materials to generate a pyroshock, a transient oscillatory response of the structure with distinct characteristics compared to other mechanical shocks. In-depth studies, employing simulation techniques and tests, are essential for understanding and managing pyroshock in aerospace missions.

Pyroshock simulations are conducted to ensure that materials and electronic/optical components can withstand the shock effects resulting from the detonation of pyrotechnic devices. These simulations can be primarily categorized into experimental and numerical approaches. The chosen approach depends on the type of established pyroshock, equipment requirements, distance from the source, and structural configuration. For this reason, the literature review in this chapter is systematically conducted and subsequently classified based on the experimental-numerical division. The combination of experimental and numerical techniques could be beneficial for a comprehensive understanding of pyroshock behavior on real components. Furthermore, considering the importance of impact physics in the context of pyroshock simulation, additional insights into contact mechanics are presented.

3.1 Systematic Literature Review

Although a few older studies on pyroshock date back several decades, the development of this topic is relatively recent, and scholars' attention to this issue has significantly increased over the last few years. In the literature, an already available narrative review conducted by Lee et al. [1] in 2012 focuses on the measurement and simulation of pyroshock. Since research on pyroshock has made substantial progress in the last decade, this section proposes a systematic analysis of the literature, which has not been presented before.

The primary objective of this systematic literature review is to identify the majority of studies conducted on the experimental and numerical simulation of pyroshock for aerospace applications. The analysis of the filtered articles allows the identification of the major existing gaps, providing motivation for the objectives of this thesis and highlighting its importance and novelty. The key elements for sieving the articles can be summarized in the following list:

- Subject related to pyroshock tests, also known as pyrotechnic shock tests;
- Application in the aerospace field for equipment qualification;
- Focus on techniques, methods, and simulation models, both experimental and numerical.

Moreover, the following further filters have been included:

- Year of publication between 1990 and 2024;
- Engineering as subject area;
- Only documents written in English.

For these reasons, an advanced search was performed on the Scopus database using the following search string:

((TITLE-ABS-KEY ("pyroshock test*" OR "shock test*" OR "shock response*" OR "shock environment*" OR "pyrotechnic") AND TITLE-ABS-KEY ("space" OR "aerospace" OR "equipment" OR "qualification") AND TITLE-ABS-KEY ("experiment*" OR "test*" OR "numerical" OR "model*" OR "technique*" OR "method*") AND TITLE-ABS-KEY ("simulat*")) OR (TITLE-ABS-KEY ("pyroshock" OR "pyrotechnic shock"))) AND PUBYEAR > 1989 AND PUBYEAR < 2025 AND (LIMIT-TO (SUBJAREA , "ENGI")) AND (LIMIT-TO (LANGUAGE , "English"))

Despite efforts to filter the studies as accurately as possible, the search conducted on 28/12/2023 produced 467 results, but the search string was not made more stringent not to exclude pertinent articles related to pyroshock simulation. Therefore, the initial 467 articles were manually selected by applying exclusion criteria. Specifically, studies were excluded if they were considered: (1) irrelevant in terms of the topic area, scope, application field, etc., (2) not significant, (3) reviews as document typology, or (4) co-authored by the undersigned [23–27]. This phase of manual filtering resulted in the selection of 28 articles, summarized in Table 1. For each article, the main contribution was reported in terms of experimental or numerical methods. Additionally, if available, characteristic information about the studies was provided. Specifically, numerical methods were classified based on the domain (methods developed in the time or frequency domain) and the numerical technique adopted (primarily categorized as FEM, SEA, and hybrid methods). Articles addressing experimental techniques or utilizing experimental data to validate proposed numerical models were classified based on the type of adopted resonant fixture (e.g., resonant plate, beam, or bar) and the excitation source (pendulum/hammer, air gun, explosive charges, laser, etc.). A preliminary analysis reveals that more than 2/3 of the articles were published in the last 10 years, indicating a growing interest in the subject.

Table 1. Results of the literature review after manual selection on the simulation of pyroshock tests for aerospace equipment qualification.

Authors	Year	Aim	Physical Domain	Num. Method	Resonant Fixture	Excitation Method
Abbas et al. [28]	2016	Exp.	-	-	Plate	Mechanical Gun
Choi [29]	2013	Exp.	-	-	Plate	Laser
Dilhan et al. [30]	2005	Exp.	-	-	Plate	Explosive charges
Garcia-Perez et al. [31]	2020	Num.	Time	FEM	Plate	Pendulum
Gherlone et al. [32]	2004	Num.	Frequency	Hybrid	-	-
Houshmand et al. [33]	2015	Exp.	-	-	Plate	Electro-magnetic
Hwang et al. [34]	2016	Hybrid	Time	Hybrid	Plate	-

Iadevaia et al. [35]	2002	Num.	Time	SEA	Plate	Electro-dynamic
Iwasa et al. [36]	2008	Num.	Frequency	Hybrid	Plate	Hammer
Jeong et al. [37]	2017	Exp.	-	-	Bar + Plate	Pneumatic Gun
Kim et al. [38]	2022	Exp.	-	-	Plate	Pneumatic Gun
Kiryenko et al. [39]	2005	Num. + Exp.	Time	FEM	Plate	Pendulum
Lacher et al. [40]	2012	Semi-analytical	Time	-	Plate	Pendulum
Lee et al. [41]	2015	Exp.	-	-	Plate	Explosive charges + Laser
Li et al. [42]	2016	Num.	Time	FEM	Beam	-
Lu et al. [43]	2022	Exp.	-	-	-	Explosive charges + Piston
Mittal et al. [44]	2018	Num. + Exp.	Time	FEM	Plate	Pendulum
Monti et al. [45]	2017	Num.	Time	Hybrid	-	-
Morais et al. [46]	2016	Num. + Exp.	Time	FEM	Plate	Pendulum
Remedia et al. [47]	2017	Num.	Time	FEM	-	Shaker
Sadkin [48]	2004	Exp.	-	-	-	Shaker
Seefeldt et al. [49]	2018	Exp.	-	-	Plate	Nail gun
Sutra et al. [50]	2005	Num. + Exp.	Time	FEM	Beam	Pendulum
Wang et al. [51]	2021	Num.	Hybrid	Hybrid	Plate	Pneumatic Gun
Wang et al. [52]	2022	Num. + Exp.	Frequency	SEA	Plate	Pneumatic Gun
Wattiaux et al. [53]	2008	Num.	Frequency	FEM	Plate	Pneumatic Actuator +

						Explosive charges
Yalcinkaya et al. [54]	2022	Num. + Exp.	Time	FEM	Plate	Pneumatic Gun
Zhao et al. [55]	2019	Exp.	-	-	Plate	Explosive charges

Since some studies were excluded from this search as they were not indexed (e.g., theses or company reports) or did not entirely meet search filters, 14 works considered relevant and interesting for the subject under investigation are additionally reported in Table 2.

Table 2. Additional relevant contributions.

Authors	**Year**	**Aim**	**Physical Domain**	**Num. Method**	**Resonant Fixture**	**Excitation Method**
Davie et al. [2]	1992	Exp.	-	-	Beam	Mechanical Sled
Davie et al. [3]	1997	Exp.	-	-	Bar	Mechanical Sled
Spletzer et al. [56]	2017	Exp.	-	-	Plate	Gas Gun
McGlaun et al. [57]	1990	Num.	Time	Hybrid	Block	Mechanical (Projectile)
Jonsson [58]	2012	Exp.	-	-	Plate	Pendulum
Cheng [59]	2021	Num.	Time	FEM	Beam + Plate	-
Kucukbayram [60]	2021	Num. + Exp.	Time	FEM	Plate	Hammer
Siam [61]	2010	Num. + Exp.	Time	FEM	Plate	Pendulum + Falling mass
Gomez [62]	2005	Num.	Hybrid	Hybrid	Plate	-
Dalton et al. [63]	1995	Num.	Frequency	SEA	-	-
Troclet et al. [64]	2009	Num.	Hybrid	Hybrid	Plate	-

Ullio et al. [65]	2001	Num.	Frequency	SEA	-	-
Lee et al. [66]	2010	Num.	Frequency	SEA	-	-
Liu et al. [67]	2019	Num. + Exp.	Time	Hybrid	-	Shaker

To summarize the whole article selection process, Figure 4 illustrates the flowchart leading to the final selection of the 28 articles identified in the database and the additional 14 works. The content analysis of these 42 contributions is developed in the following sections, with a focus on both experimental and numerical approaches.

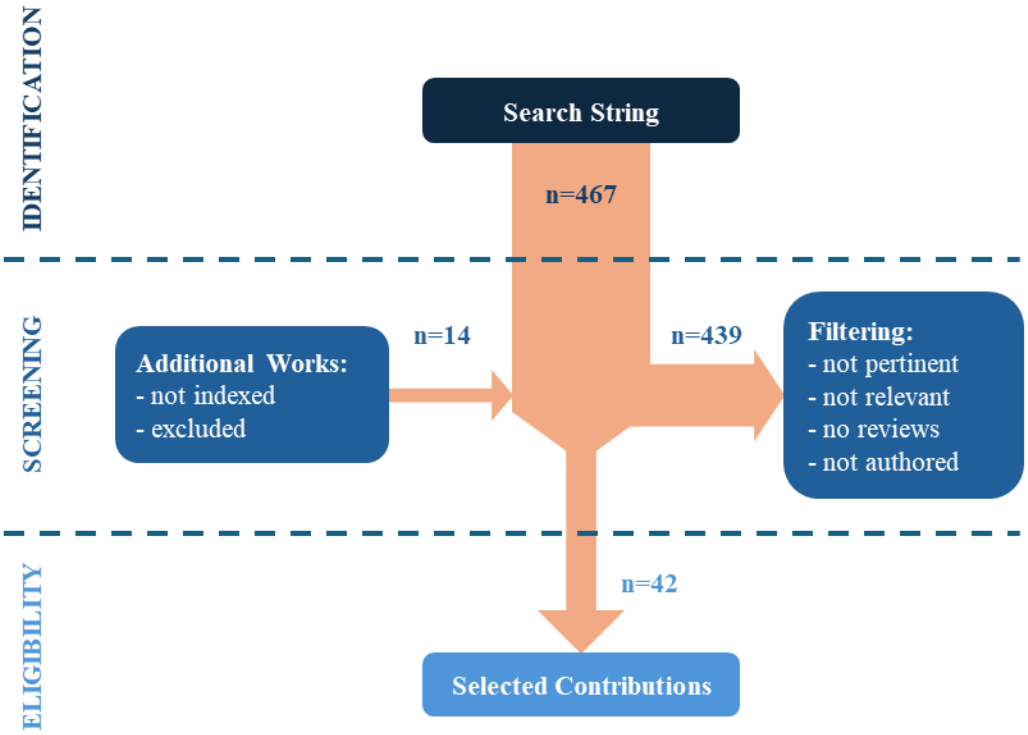

Figure 4. Flowchart describing the selection process for the systematic literature analysis.

3.2 Pyroshock Numerical Simulation Models

Numerical simulation employs mathematical methods to describe the behavior of real systems. This approach can be utilized both for comprehensive pyroshock test simulation and to predict the response of the experimental test setup. Since the current state-of-the-art inherent to the analytical characterization of collisions has not reached a sufficient level of detail to study the structural behavior resulting from impulsive loads, numerical models become essential. They permit to obtain responses to impact tests in the aerospace field to verify the resistance of the components. Various approaches exist in the literature, often complex and employing multiple techniques synergistically. In general, these approaches can be classified into several macro-categories, where Finite Element Method (FEM) and Statistical Energy Analysis (SEA) are prominent. These methods allow the analysis of wave propagation, thereby predicting and estimating the dynamic response of the mechanical system.

From the systematic analysis of the literature, it is evident that the majority of the selected works use a FE-based method for the numerical simulation of pyroshock tests. Specifically, 12 (46%) out of 26 works containing information on numerical methods propose an FE-based model. As depicted in Figure 5, the remaining works are distributed among SEA-based methods or hybrid models, incorporating multiple approaches simultaneously. Similarly, it can be observed that most of these methods operate in the time domain (16 out of 26). This correlation between the typology of methods and their domain can be explained by the fact that FEM typically employs transient analysis, a numerical simulation technique used to study the dynamic response of a structure subjected to time-varying excitations. The same is valid for SEA methods that typically operate in the frequency domain. Few selected studies exploit Transient Statistical Energy Analysis (TSEA), a technique that combines SEA with transient time-domain analysis, or FEM to directly derive the Frequency Response Function (FRF) of the dynamic system.

A brief overview of the methods selected in the literature follows, highlighting their strengths and limitations. Generally speaking, FEM, exploiting transient analyses and working in the time domain, requires long computational times and produces a large amount of data. On the other hand, SEA methods have lower accuracy at low frequencies and do not allow predictions of responses at specific frequencies and individual points, as they are statistical methods. Based on these considerations, this thesis aims to propose numerical methods for simulating pyroshock tests that

provide accurate results without excessively increasing the computational burden. For this reason, the proposed methods have a common approach based on the FRF computation of the resonant fixture (e.g., resonant plate, beam) through spatial discretization using MDOF or FE-based methods. Therefore, it can be stated that the proposed work would be positioned in the literature among FE-based methods (used in most cases for their advantages) and approaches working in the frequency domain (novelty contribution, as almost all the FEM-based works use the transient temporal analysis). As described later in the thesis, this combination allows for obtaining precise SRS predictions typical of FEM, significantly reducing computational times through the development of methods in the frequency domain.

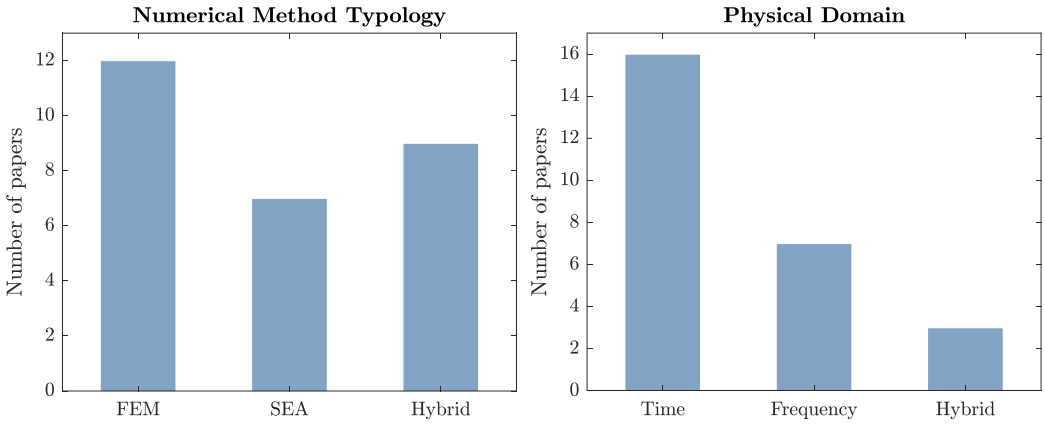

Figure 5. On the left, histogram of the method typologies of the selected papers describing numerical methods for pyroshock simulation. On the right, histogram of their domain.

3.2.1 Statistical Energy Analysis

The proposed general approach, known as Statistical Energy Analysis (SEA), is a methodology developed to address high-frequency vibroacoustic problems. Since pyroshocks are characterized by high-frequency content, this approach has been successfully extended to predict pyroshock responses using steady-state power balance equations. In the context of SEA, the entire analyzed system is divided into a series of coupled subsystems, each representing a group of modes with similar characteristics.

This technique heavily relies on accurate estimation of input power, modal densities, damping loss factors, and coupling loss factors. The magnitude of the obtained average FRF using the SEA can be employed with Virtual Mode Synthesis

and Simulation (VMSS) to predict transient responses. Many works, both old and recent, utilize the combination of these techniques, as in [52,63,66]. In the case of transient and shock loading, reference is made to Transient Statistical Energy Analysis (TSEA) [68,69]. Iadevaia et al. [35] proposed a TSEA procedure, applying SEA to study transient phenomena like the response of plate-like structures excited by shocks. SEA has attracted considerable attention in researching high-frequency structural response prediction. Compared to FEM, SEA is considered more suitable for high-frequency dynamic problems, as it is simpler to apply and often produces more accurate predictions at lower computational costs. Ullio et al. in [65] suggest using SEA in favor of or in combination with FEM. However, it is important to note that SEA is limited to high frequencies and provides averages over spatial positions and frequency bands, not allowing predictions of responses at specific points and frequencies. The formulation of the basic SEA equation incorporates concepts from statistical mechanics, acoustics, wave propagation, and modal analysis, making the choice of subsystems and parameter evaluation complex and challenging.

3.2.2 Finite Element Method

The Finite Element Method (FEM) is a fundamental approach employed to model, simulate, and predict shock response, both in the time and frequency domains. It is a deterministic method that requires accurate knowledge of all structure parameters. The procedure involves discretizing complex structures into sub-elements, then solving a series of differential equations describing their behavior. FEM proves particularly effective in the precise simulation of a structure's response to static and dynamic loads at mid and low frequencies. In the context of pyroshocks, FEM allows the application of well-characterized shock and vibration excitations to predict structural responses. Indeed, FEM enables accurate calculation of structural and acoustic modes over a wide frequency range for complex dynamic systems.

For these reasons, several studies exploit Finite Element Analysis (FEA), which is one of the most used methods nowadays in the industrial field for static and dynamic structural analyses. Yalçinkaya et al. [54] demonstrate the potential of an explicit finite element solver for predicting experimental SRS curves. Remedia et al. [47] propose virtual testing modeled through FE. Perez et al. [31] introduce FEM transient analysis to verify the structural design of a Supra Thermal Electrons and Protons (STEP) unit. The same authors in [70] provide an overview of the numerical analyses that can be used for shock test qualification by exploiting the FEM. In particular, they demonstrate that FEM can be adequate for analyzing small

structures subject to shock loads, as the need for a sufficiently fine mesh is not a critical issue, and simultaneously, it is possible to obtain appropriate accuracy for the simulations. In this study, an overview of analysis options using FEM to simulate shock loads is provided. The methodologies include:

- *Transient analysis* is the most general and calculates the behavior of a structure subjected to time-varying loads. It offers the advantage of obtaining temporal functions for various outputs but requires high computation times and produces a large amount of data.
- *Response spectrum analysis* estimates peak responses using modal analysis of the structure and applying the SRS to the base, but it has limited precision.
- *Sine transmissibility method* calculates SRS curves of the response acceleration by multiplying the input SRS by the shock transmissibility. However, it cannot determine peak values or time domain functions.
- *Equivalent quasi-static load method* provides an approximation of the total interface force of the shock load.

However, the FEM has some limitations. For instance, when dealing with high modal densities, the method becomes remarkably computationally expensive, limiting mesh size and allowing accurate modeling only for relatively simple structural configurations. Despite these limitations, simulating shock on simplified models provides SRS predictions consistent with measured tests at low frequencies. Demonstrations that FEA methods for simulating pyroshock responses are valid for simplified systems such as beams and plates are respectively proposed in [59] and [46]. It is worth emphasizing that, despite the versatility of FEM, it may be less suitable for simulating pyroshock tests characterized by high nonlinearities and high frequencies.

3.2.3 Other Methods

Researchers have suggested the use of a hybrid model for simulation at mid frequencies, given that methods based on FEM and SEA exhibit limitations at high and low frequencies, respectively. The mid-frequency system could result in too intricate for FEM and not random enough for SEA. The hybrid model divides the system's response into subsystems managed by FEM or SEA based on modal density, allowing for a more effective approach at medium frequencies. Troclet et al. [64] propose such an approach, combining FEM and SEA to predict mid and high frequencies. Another example of the combination of these techniques is utilized by

Wang et al. [52]. However, a comparison of their method with the related experimental outcomes reveals a considerably high error in the calculated results. Indeed, integrating a deterministic method like FEM and a statistical one like SEA into a unified model is complex due to their inherent substantial differences.

Finally, some methods belong to the category of hydrocodes. Hydrocodes are computational methods based on differential equations for unstable dynamic motion. These methods address the simulation of pyroshock with coupled or decoupled approaches, conducting comprehensive or separate analyses for initiation-explosion and structural response. This temporal method allows the simulation of the dynamic response following typical pyroshock explosions. By coupling complex material models with structural fluid dynamics, this method proves to be effective in highly dynamic situations, especially with shock waves. Although they are efficient for simple structures, hydrocodes become costly and require extended computation times for complex structures, making them powerful but demanding on resources with limited predictive accuracy.

3.3 Pyroshock Experimental Techniques

The experimental simulation of pyroshock tests aims to reproduce the propagation of shock waves generated by the real system. Various typologies of experimental simulation can be grouped into three main categories: (1) exciters using explosive charges or pyrotechnics, (2) mechanical exciters, and (3) optical exciters. Mechanical exciters encompass a wide range of impact generators, ranging from pendulums and hammers to pneumatic guns and nail guns. The use of lasers to simulate shock wave propagation is a less established and less well-known methodology in the literature. Analyzing systematically selected studies from the literature reveals that the majority of test benches (66%) utilize a mechanical exciter, while few studies describe pyrotechnic or laser excitation systems. Figure 6 shows a considerable number of other types of excitations, primarily electrodynamic excitations by means of shakers.

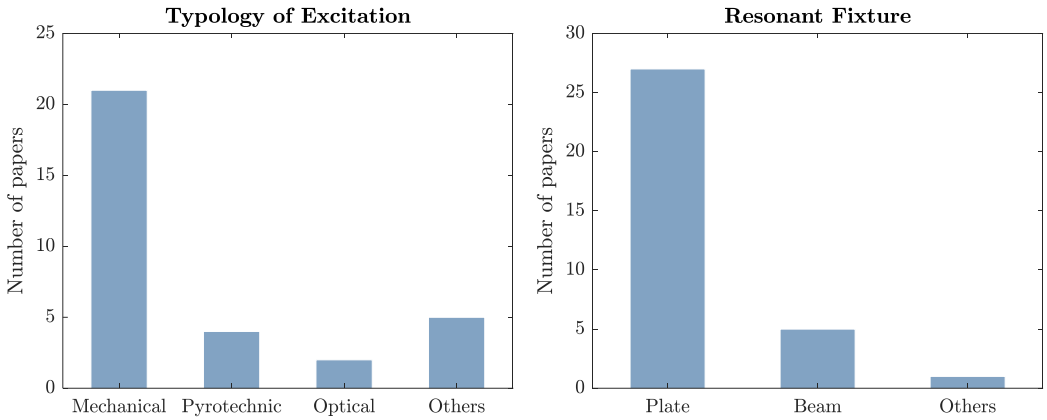

Figure 6. On the left, histogram of the excitation techniques of the selected papers describing experimental test benches for pyroshock simulation. On the right, histogram of the adopted resonators.

From the systematic analysis of the literature, it can also be understood that the resonant plate is the most widely used resonant fixture for simulating pyroshock tests. Indeed, after generating an impact using any technique, an interposing element is needed to allow proper calibration of the test bench and transmit the shock wave to the component under test. Resonant plates are the most well-known and commonly used technique in the field of pyroshock. However, it is worth noting that some studies (15%) use beams and bars as an alternative to the resonant plate.

Some experimental setups used in the literature are described and illustrated in the following. In the subsequent chapters of this thesis, a test bench designed to experimentally simulate pyroshock tests at the Politecnico di Torino is proposed. The choice of the experimental configuration was based on the use of an interchangeable resonant plate, as it proved to be the most performant and effective method given its widespread use in the literature. Two mechanical excitation techniques are also proposed: a pneumatic gun and a pendulum. These techniques have been selected as mechanical excitations since they are efficient, accurate, and repeatable. The design of two excitation systems is motivated by the need to generate different impulses. Indeed, with the same generated momentum, the air gun allows the launch of projectiles with lower masses at high speeds. On the contrary, the pendulum has the advantage of using impacting bodies with higher masses but with a limit on the maximum achievable speed.

3.3.1 Resonant Fixtures

Resonant fixtures are the most widely adopted technique for experimental simulation of pyroshock, as they enable the reduction of trial-and-error iterations in testing. These resonant fixtures are designed with a fixed knee frequency, determining the correspondence between their dominant resonant frequency and the SRS knee frequency. Adapters are required to connect the test object and allow acceleration measurements on all three axes. Resonant fixtures provide good tuning and repeatability of the SRS, although the test object influences the frequency content. Some typologies of resonant fixtures are shown in Figure 7 as an example.

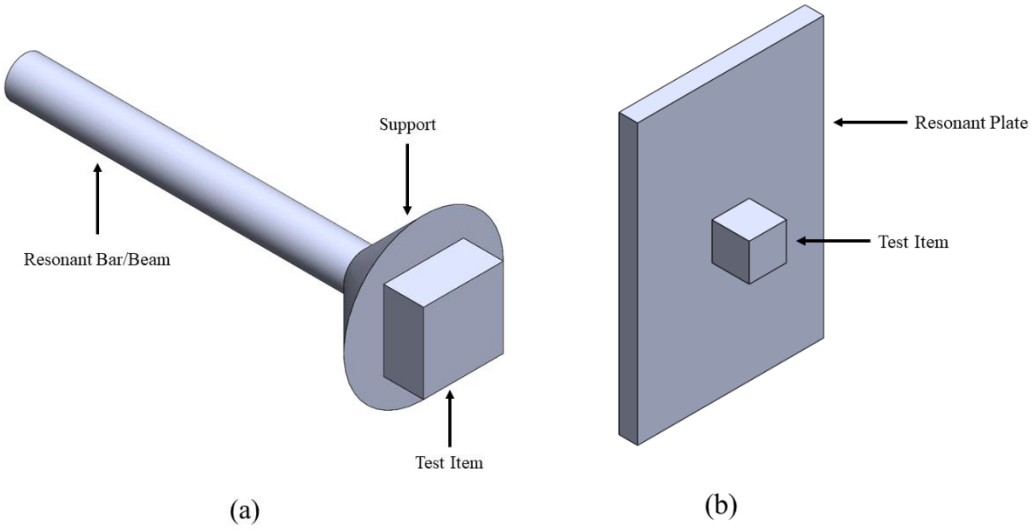

Figure 7. Different typologies of resonant fixtures: (a) resonant bar/beam, and (b) resonant plate.

The resonant plate is the most commonly used fixture to simulate pyroshock tests. The test object is mounted on the metallic resonant plate, which is in turn either suspended to simulate free-free boundary conditions or fixed to the support structure of the test bench. The mechanical impact, typically applied to an interposed anvil plate, induces vibrations in the plate. The dominant resonance frequency must be appropriately tuned to match the knee frequency of the test requirement. The plate configuration can be modified to change the resonance frequency and, consequently, tune the experimental setup according to variable requirements. The calibration adjustments primarily involve variations in the impact position, the use of interposed plates named anvil plates, damping insulators through polymeric layers, and changes in the arrangement of the test object.

Experimental configurations using bars or beams are alternatives to the resonant plate. The main difference between these two resonant objects lies in the wave propagation. Bars transmit longitudinal waves, while beams exploit flexural modes. In configurations with a resonant bar, the test object is fixed at one end, and the mechanical impact is applied at the opposite end, inducing resonance in the bar's longitudinal modes. These can be tuned by adding weights at specific positions along the bar. On the other hand, the resonant beam is fixed to a massive base to simulate a cantilever beam. The mechanical impact is applied in order to excite its flexural modes. Davie et al. have proposed two tunable configurations for pyroshock simulation in [2] and [3], using a beam and a bar as resonant fixtures, respectively.

3.3.2 Mechanical Excitation

There exist numerous typologies of simulations for mid- and far-field shocks using mechanical excitations. These range from dropping masses to pendulums or hammers, from actuators to projectiles launched by gas guns, nail guns, or sleds. Each of these methods has specific advantages, and the choice depends on the test requirements and specifications, and the characteristics of the specimen.

In test benches exploiting falling masses, the impact is generated by dropping a table onto the test object using an appropriate device and spring connections, as depicted in Figure 8. This typology of test bench is the least suitable for simulating pyroshock because such impacts generate a transient response that highly differs from the real behavior of explosive charges. Drop tables can lead to severe overtesting at low frequencies, causing structural failures that would not have been produced by real pyroshocks. The low performance of this test bench is further demonstrated by the fact that there are very few studies in the literature exploiting drop tables.

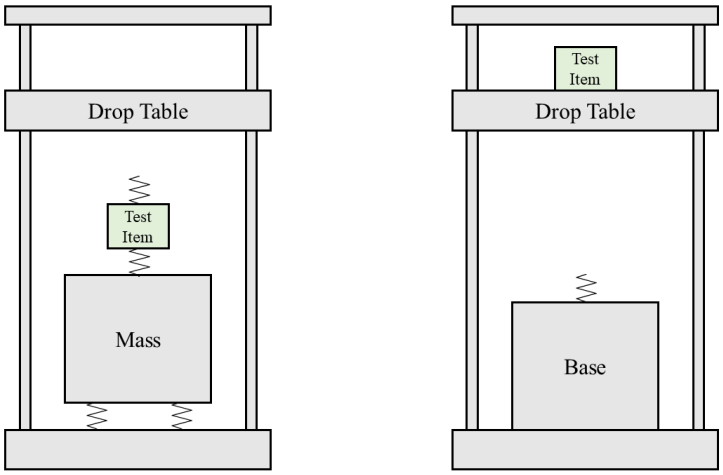

Figure 8. Examples of drop tables for pyroshock testing.

Test benches using pendulums or hammers to generate the shock are much more common. In general, a representative illustration can be referred to the structures shown in Figure 9. This technique consists of a pendulum with mass m dropped from a height h to hit the resonant fixture. The magnitude, duration, and frequency range of the shock depend on numerous factors, including the geometry and material of the impacting bodies, the mass and velocity of the pendulum/hammer, and the impact and test object positions. This method provides repeatable results and generates high momentum. However, the main limitation lies in the maximum speed achievable for the impact. Indeed, the maximum speed of the pendulum is reached at the lowest point of its trajectory and strictly depends on the initial height according to the formula $u_{MAX} = \sqrt{2gh}$. In the case of impact on a resonant plate, the pendulum can assume two main configurations based on the direction of the applied impact: Out-Of-Plane (OOP) and In-Plane (IP) configurations. In the OOP configuration, the impact is applied perpendicular to the resonant plate, primarily exciting its flexural modes. On the contrary, in the IP configuration, the impact is applied parallel to the plate plane. Morais et al. [46] propose an experimental setup that utilizes the response of a resonant plate excited by a pendulum in the IP configuration to simulate a shock environment. Similar proposals are made by Jonsson [58], Mittal et al. [44], and Kiryenko et al. [39], although they consider both IP and OOP configurations.

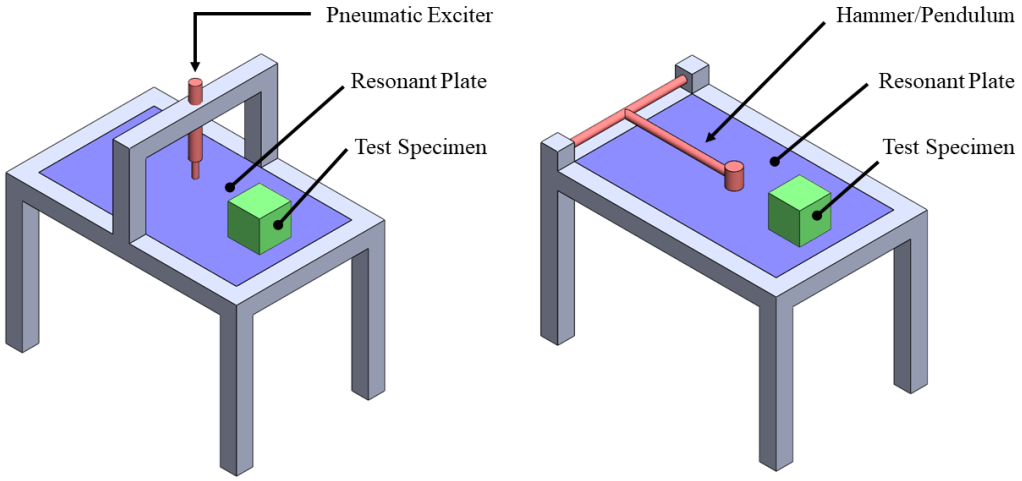

Figure 9. Examples of pyroshock simulator exploiting mechanical excitation techniques (pneumatic exciter and hammer or pendulum, respectively).

Very similar and equally widespread are projectile launchers, which typically utilize pneumatic systems to shoot a projectile against the resonant fixture. In some specific cases, the projectile is replaced by a piston or an actuator. Unlike pendula, pneumatic guns achieve impacts characterized by high velocities, but they limit the mass of the impacting bodies. The velocity and the mass of the colliding body enable the generation of different impacts and, consequently, tuning the test bench to varying frequency content requirements. Among the numerous studies in the literature proposing test benches for simulating pyroshock using pneumatic guns, notable ones include Yalçinkaya et al. [54], Wang et al. [52], and Jeong et al. [37]. More original is the work proposed by Kim et al. [38], suggesting a resonant device interposed between the plate and the air gun.

3.3.3 Pyrotechnic Excitation

Excitation with explosive charges is used to test structural integrity and design functions by generating high accelerations and frequencies. Pyroshock is produced by charges on the resonant plate. The configuration requires numerous trial-and-error attempts, making the method expensive and time-consuming. During the calibration phase, a dummy object is adopted. In addition to the drawbacks in terms of time and cost, this methodology presents other critical issues, such as the risk associated with handling and detonating explosive charges, as well as potential damage to the structure during each test. For these reasons, a qualified structure and related safety procedures are necessary to handle explosives. Moreover, the use of real

explosives can cause significant variations in impacts, reducing the repeatability of shock spectra guaranteed by mechanical exciters. As an example, some test benches to simulate the effects of pyroshock using explosive charges are shown in Figure 10.

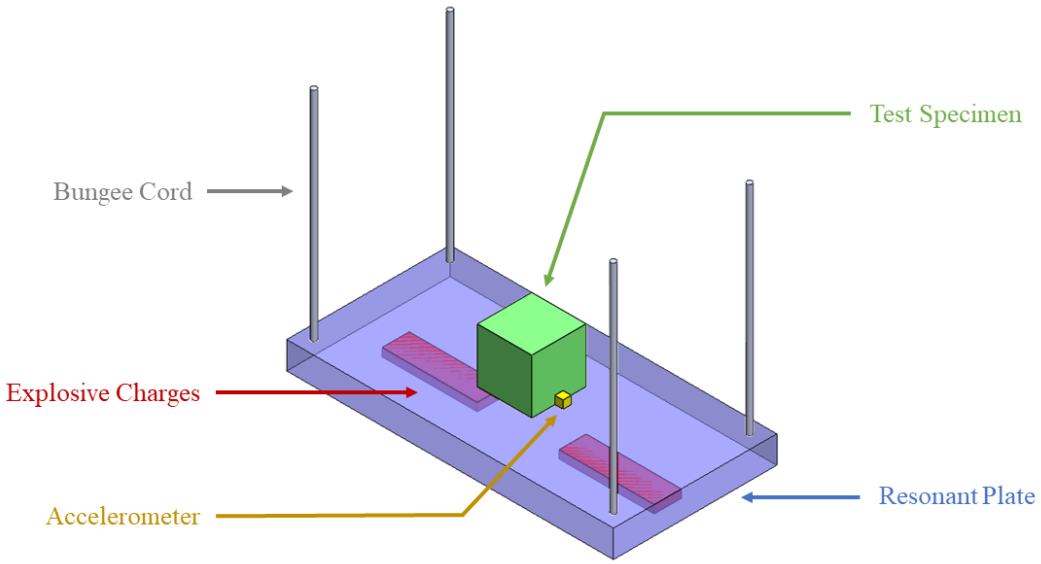

Figure 10. Example of a pyroshock simulator through explosive charges.

Dilhan et al. [30] proposed a characterization of eleven different typologies of pyrotechnic devices with various operating principles, materials, and amounts of explosive charge. Zhao et al. [55] suggest a test bench that generates excitation through an explosive charge appropriately positioned in a protective cover with a suitable exhaust hole to facilitate gas release.

3.3.4 Other Techniques

In addition to the well-known mechanical and explosive excitations, optical and electrodynamic techniques are also adopted in some cases, such as laser and shaker excitations.

Laser excitation utilizes an optical pulse to generate transient localized heating in the proximity of the material surface, producing thermoelastic stresses and deformations that act as a wave source. The main limitation consists in its inability to achieve high-magnitude excitations. An experimental simulation of pyroshock with laser excitation is proposed by Choi in [29]. In this work, a Q-switched Nd:YAG

diode-pumped solid-state laser was adopted. An alternative setup using laser-induced shock is described by Lee et al. [41].

Transient responses to pyroshock can also be simulated using an electrodynamic shaker. The limitations of this technique primarily involve frequency ranges and maximum accelerations. Despite the typical precision of shakers, this method can be considered suitable only for simulating low-energy pyroshock. Liu et al. [67] verified the effectiveness of their proposed method by experimentally simulating pyroshock tests using shakers. Remedia et al. [47] utilize the Hydra shaker capable of generating excitations along all six degrees of freedom. Finally, Houshmand et al. [33] propose an alternative experimental setup to overcome the limitations of shakers in terms of bandwidth. To propagate the wave on the plate, they use an electronic pulse generator and a coil, which produces a magnetic field and induces currents on the plate.

3.4 Contact Mechanics Insights

The field of contact mechanics is so vast and abundant that a thesis would still be insufficient for an exhaustive exploration. This Section does not aim to systematically study the state of the art on this subject, as done for pyroshock simulation methods. Instead, it briefly examines some key concepts that will be useful in the following chapters. Specifically, attention is focused on certain contact dynamics methods, starting from those describing perfectly elastic contacts (thus based on Hertzian contact theory) to some non-Hertzian viscoelastic and elastoplastic models. Finally, the coefficient of restitution, often used in contact mechanics to describe the energy dissipated during an impact, is explored.

In general, many approaches can be considered to describe contact mechanics. The first main group includes elastoplastic static contact models, which divide the contact process into three phases: elastic, elastoplastic, and fully plastic. The elastic phase is usually studied using Hertzian contact theory. Once the contact deformation exceeds the critical elastic deformation, the contact is no longer perfectly elastic, and the behavior is no longer governed by Hertz's theory. The beginning of plastic deformation can be analytically defined through a specific yielding criterion. Consequently, the fully plastic phase can be governed, for instance, by von Mises yielding theory.

A second major group of approaches to contact mechanics consists of continuous contact models. These consider energy dissipation through hysteresis cycles,

based on the concept that interaction forces act continuously during impact. Again, the starting theory is Hertz's one, which describes contact between two perfectly elastic bodies. However, it does not include any energy dissipation. Over the years, several approaches have been proposed to overcome this limitation. Among the most well-known are the Kelvin-Voigt and Hunt-Crossley models. The Kelvin-Voigt model adopts a linear spring-damper system that takes into account energy dissipation during contact, thanks to the damping term. Hunt and Crossley implemented the Kelvin-Voigt model by introducing a damping coefficient as a function of contact deformation.

Finally, some approaches assume a very rapid interaction between bodies and neglect variations in their configuration during impact. These approaches divide contact dynamics into two main phases: before and after impact. In this case, energy dissipation is modeled using coefficients, such as the coefficient of restitution.

3.4.1 Hertzian Contact Theory

The Hertzian contact theory represents a fundamental contribution to understand elastic deformation and contact mechanics between solid bodies. The theory deals with interactions that occur when two elastic spheres come into contact under quasi-static normal force. Hertz's model provides valuable insights into the distribution of stresses and deformations at the contact interface, offering a mathematical framework to analyze and predict the behavior of materials under compression. In particular, Hertz's theory focuses on determining the size and shape of the contact area, as well as the distribution of pressures and deformations within that area. The theory assumes that the involved materials are linearly elastic, isotropic, and homogeneous and that the deformation is small enough to maintain elastic behavior.

The most renowned treatises presenting the mathematics of elasticity theory are those by Love [71] and Landau-Lifshitz [72]. A qualitative approach has been proposed by Leroy [73]. The Hertzian theory describing elastic contact between two spheres can be generalized and applied to the case of contact between a sphere and a flat surface, according to Gugan [74]. In particular, this study demonstrates how the Hertzian theory accurately describes even the case of inelastic contacts where 40% of kinetic energy is lost during the collision. The author explains this result by noting that the estimates of the contact area and time primarily depend on the compression phase, where there is not a high loss of energy, suitably described by elastic theory.

3.4.2 Viscoelastic and Elastoplastic Models

Viscoelastic and elastoplastic theories describe contact mechanics by attempting to overcome the limitations of the Hertzian contact theory, including energy dissipation and material plasticity. While the Hertzian theory assumes purely elastic behavior, elastoplastic contact theories deal with situations in which materials withstand both elastic and plastic deformations during contact. In elastoplastic contact, solid bodies undergo irreversible deformations, allowing for a more realistic representation of the mechanical behavior of materials in contact. This is particularly relevant in situations where applied loads exceed the elastic limits of the involved materials. Figure 11 shows some contact mechanics models identified by the described force-indentation curve.

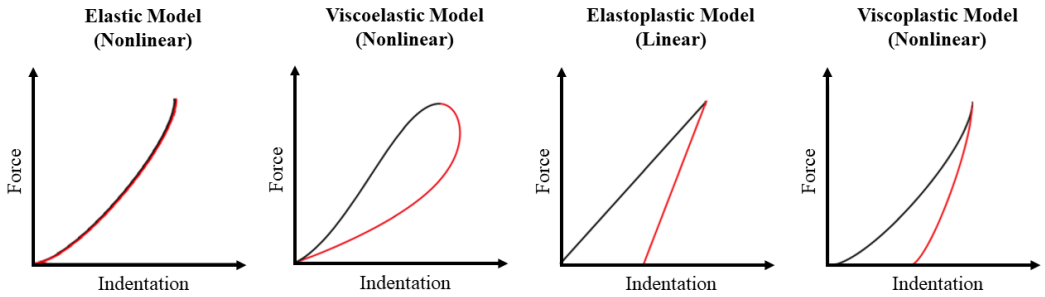

Figure 11. Example of contact mechanics models classified by the force-indentation curve. The hysteresis cycle is composed by the compression (black curve) and restitution (red curve) phases.

Numerous viscoelastic and elastoplastic models exist in the literature, and many scholars have provided overviews of the state of the art in impact physics. Ghaednia et al. [75] classify models for describing single asperity elastoplastic contacts based on the geometry of the impacting bodies. For example, in the case of contact between a sphere and a flat surface, they categorize models into three groups: those considering the flat surface as rigid and deformations concentrated on the sphere (flattening models), models conversely considering the sphere as stiff and the plate as deformable (indentation models), and finally, more comprehensive models that generalize the impact considering both deformable bodies. Then there are studies by Kerr [76] and Younesian et al. [77], which provide reviews on elastic and viscoelastic models of foundations. Foundation models are typically used to describe static contacts in structural mechanics. However, they could be adapted to impact

mechanics and it is also interesting to observe how approaches have evolved, gradually incorporating viscoelastic and nonlinear effects of materials.

The earliest foundation model is a simple linear elastic model introduced by Winkler [78]. In this approach, the foundation is assumed to consist of independent linear springs. Springs linearly relate pressure and deformation according to a material-specific elastic constant k. This model has been gradually developed, firstly by Filonenko-Borodich [79], who introduced an elastic membrane making the elastic elements interact, and later by Hetényi [80], who assumed that the beam or plate deforms only in bending. Finally, Pasternak [81] introduced shear interactions between the elastic elements. To overcome the limitation of elastic behavior, researchers have extended Winkler's foundation models by incorporating a viscoelastic element, as in the Kelvin-Voigt one [82]. The foundation is then modeled as a series of spring-damper systems in parallel. An alternative model is known as Maxwell model [82], in which dampers are assumed in series with the springs. The foundation models have been defined in many variations, depending on the number of springs and dampers considered, their arrangement in series or parallel, and the number of layers in the model. However, the Kelvin-Voigt model still has some drawbacks. In particular, the hysteresis cycle, reconstructed thanks to the viscoelastic factors, appears as a semi-ellipse with a discontinuity at the origin. This discontinuity loses physical meaning as it introduces a traction force on the impacting body in the separation phase. For this reason, Hunt and Crossley [83] proposed a viscoelastic contact model that describes a closed hysteresis cycle converging at the origin. This result was achieved by introducing a damping coefficient as a function of the contact deformation. The foundation models described so far have been illustrated in Figure 12.

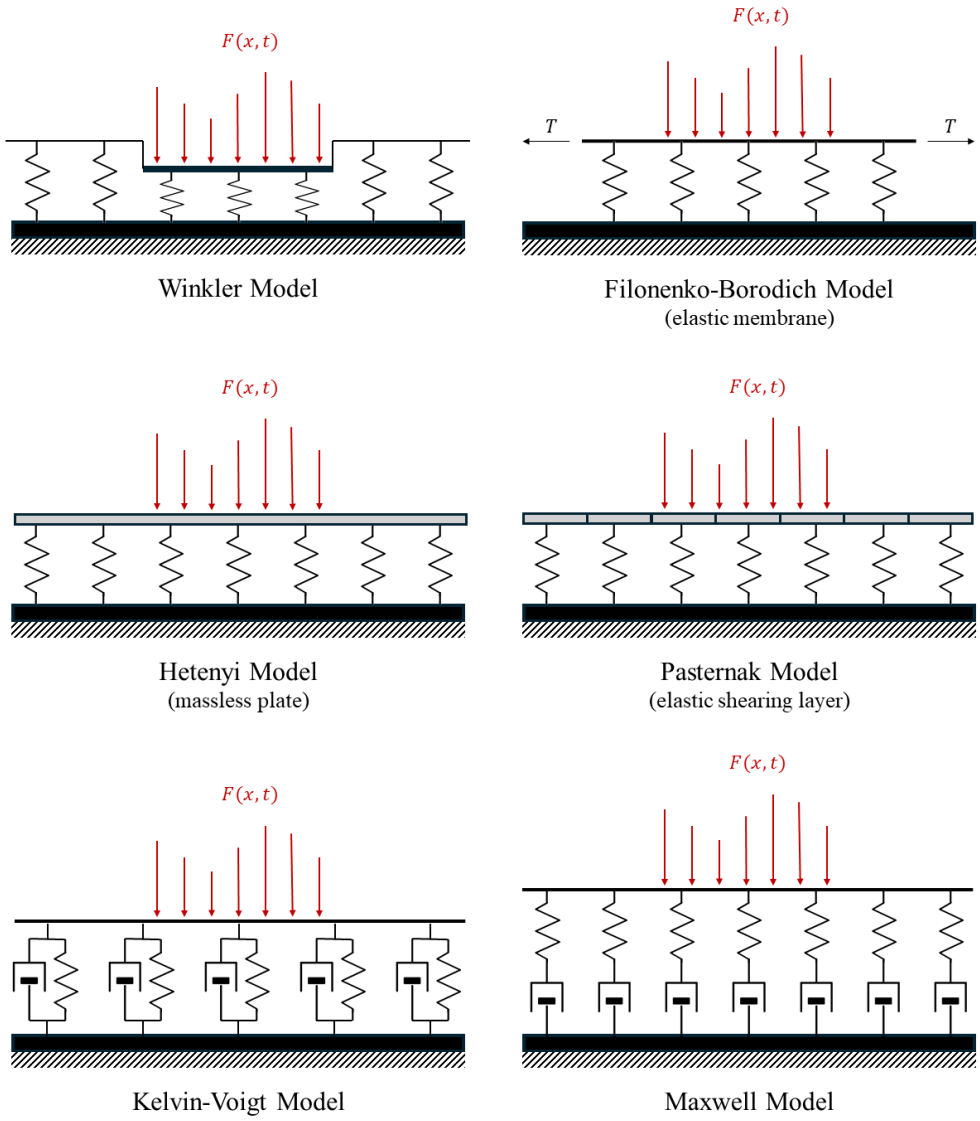

Figure 12. Main foundation models.

3.4.3 Coefficient of Restitution

Impact, defined as the collision between two bodies in a short time frame, is a highly complex physical phenomenon. Continuous impact models can be very intricate and depend on numerous parameters, as briefly summarized in the previous sections. To simplify impact modeling, studies have introduced the Coefficient Of Restitution (COR). The development of these models aims to derive the behavior of bodies in the post-impact phase based on the known behavior in the pre-impact phase. Given that the involved bodies experience a high level of force for a very

short duration, it is possible to divide the impact into two phases. The first phase, known as the *compression* phase, encompasses everything from the moment in which the bodies come into contact until their maximum compression. The second *restitution* phase takes place when the bodies begin to separate and ends when the bodies are completely detached.

In this context, the COR is a parameter aiming to determine the energy loss during impact. The COR value typically ranges between 0 and 1, where 0 represents a completely plastic collision as all energy is dissipated, while 1 means a perfectly elastic collision with energy conservation. The COR is influenced by various parameters such as the geometry of the bodies, the initial velocity, the material properties, and the contact duration. The initial kinetic energy is partially dissipated due to material damping, plastic deformations, wave propagation, and in the form of thermal and acoustic energy. The COR can exceed 1 only if, during the collision, there is an increase in energy due to factors such as a chemical reaction. However, it is worth noting that values greater than 1 are atypical and often indicate specific circumstances or singular conditions.

Newton was the first scientist to study the impact between two rigid bodies, defining the COR as a kinematic quantity that relates the perpendicular velocities before and after the impact at the contact point. According to this model, the COR (usually denoted by the letter e) is calculated using the following formula:

$$e = -\frac{u_f}{u_i} \tag{9}$$

where u_f and u_i are the relative post-impact and pre-impact velocities respectively. Subsequently, Poisson's model proposed a similar concept, defining the COR as a kinetic quantity that correlates the perpendicular impulses during the compression and restitution phases:

$$e = \frac{p_r}{p_c} \tag{10}$$

where p_r and p_c are the normal impulse for restitution and compression respectively. Nevertheless, Stronge [84] identified energetic discrepancies in specific cases analyzed by using Poisson model. To solve this issue, Stronge suggested

defining the COR as the square root of the ratio between the energy released during restitution and the energy absorbed by deformation during compression:

$$e = \sqrt{-\frac{W_r}{W_c}} \tag{11}$$

where W_r and W_c are the energy released during the restitution and compression phases, respectively.

In the literature, many studies propose the COR estimation, considering variations in impact configuration, such as changes in the geometries of impacting bodies, impact velocities, material properties, etc. Zener [85] and Weir-Tallon [86] studies are particularly relevant and well-known in this field.

Chapter 4

Frequency Domain Approach

As evidenced by the literature review, the resonant plate emerges as a widely adopted experimental setup in the context of pyroshock testing [87]. In these testing configurations, a specifically designed plate is employed to generate an established frequency response. A test component, typically connected using a fixture, is positioned on one side of the plate. The opposite side of the plate is impacted by a projectile, while a damping material may be strategically placed at the impact position to regulate impulse duration and magnitude. A uniaxial accelerometer is conventionally placed close to the object under test to measure acceleration along an axis aligned with the impact direction. Subsequently, the SRS is computed from the recorded time signal, assumed to accurately represent the experienced shock.

The SRS serves as a metric to quantify the severity of the transmitted shock and is derived by employing a peak-and-hold type measurement, simulating the response of an equivalent and calibrated SDOF system to the same shock. The primary objective of the modeling effort is to identify the maximum absolute acceleration of the equivalent SDOF system in response to the impulsive force generated by the bullet impacting the designated pad.

This chapter introduces innovative methods for calculating the acceleration of the pyroshock testing system in SRS terms, exclusively in the frequency domain. Starting from the description of a semi-analytical approach laying the foundations for subsequent numerical models, the analysis focuses on the convolutional method and presents an alternative approach to computing the SRS.

4.1 A Semi-Analytical Approach

The proposed semi-analytical model relies upon the mechanical system depicted in Figure 13, generically illustrating a simplified pyroshock testing and especially elucidating the development of the SRS calculation. It serves as a qualitative graphical representation of the SRS generation process. The transient acceleration responses of individual SDOF oscillators are presented, and their respective maximum values are graphically illustrated based on their natural frequencies, collectively establishing the SRS. This description is an initial, simplified model of the bullet-plate-SRS mass system, where m_s is the impacting mass, m represents the whole plate, and all the different m_{SRS} stand for the SDOF systems tuned at the c-th frequency Ω_c. The impact resulting from the collision of the two bodies induces vibrations that propagate initially through the plate and subsequently through the hypothetical SDOF systems independently. This semi-analytical model aims to describe the transmission of vibrations by exploiting the behavior of the mechanical subsystems.

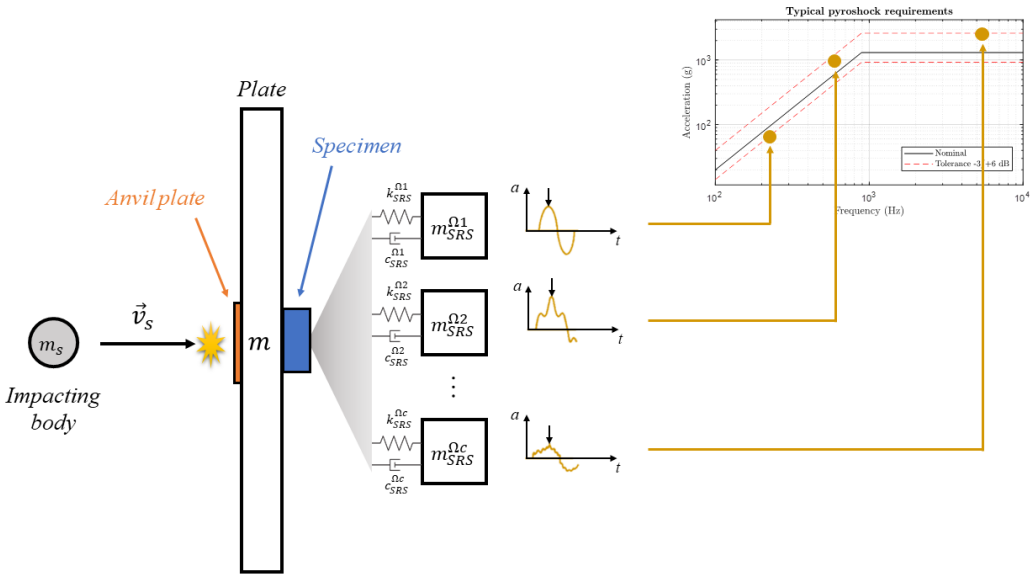

Figure 13. Simplified modelling of a generic pyroshock testing and development of the shock response spectrum.

Considering the frequency response of a unitary impulse, interpreted as a pulse with unitary momentum or equivalently unitary area under the curve, the SRS of the resonant plate system, under specific conditions, can be determined by exploiting the transmissibility T of a mass-spring-damper system. The latter system is

characterized by a damping ratio $\zeta_{SRS} = 0.05$ and a natural frequency Ω_c. To study the entire frequency band, the different SDOF systems must be tuned to achieve a frequency resolution of 1/24 octave for the same definition of SRS. The entire analysis is conducted exclusively in the frequency domain.

This approach offers several advantages during the modeling phase, enhancing algorithmic efficiency and result accuracy. Notably, it minimizes the use of computations as direct and inverse Fourier Transforms (FT), resorting to their use only when strictly necessary. For example, the Inverse Fast Fourier Transform (IFFT) is employed exclusively in calculating the SRS, given the need due to the same definition of SRS, i.e. maximum absolute value of the signal in the time domain. The mathematical steps governing the computation of SRS acceleration, incorporating known parameters and addressing both the direct and inverse problems, are briefly summarized in the following equation, where the SRS acceleration $\ddot{X}_{SRS}(\omega)$ has been decomposed into the following product:

$$\ddot{X}_{SRS}(\omega) = F(\omega) \cdot \frac{X(\omega)}{F(\omega)} \cdot \frac{X_{SRS}(\omega)}{X(\omega)} \cdot \frac{\ddot{X}_{SRS}(\omega)}{X_{SRS}(\omega)} \tag{12}$$

where $F(\omega)$ is the spectrum of the applied pulse, $X(\omega)$ is the displacement of the plate, $X_{SRS}(\omega)$ is the displacement of the SRS mass, $\ddot{X}_{SRS}(\omega)$ its acceleration, and ω is the frequency. It can be observed that the ratios composing the product represent well-known physical quantities, such as specific frequency response functions. Indeed, $\frac{X(\omega)}{F(\omega)}$ is precisely the definition of receptance. Several works in the literature present analytical solutions for the frequency response of generic rectangular plates [88]. However, solutions for plates with free-free boundary conditions are not known or easily obtainable. Therefore, this frequency response function will be solved in the subsequent sections of the thesis using numerical methods, making the present method semi-analytical. Similarly, the ratio $\frac{X_{SRS}(\omega)}{X(\omega)}$ is known and coincides with the transmissibility of a mechanical system. Indeed, the numerator and denominator of this ratio represent, respectively, the excitation and response of the hypothetical SDOF system for SRS calculation. Finally, the ratio of acceleration to displacement of an SDOF system $\frac{\ddot{X}_{SRS}(\omega)}{X_{SRS}(\omega)}$ is, by definition, equal to $-\omega^2$. Considering that the spectrum of the applied pulse $F(\omega)$ can be decomposed to explicitly express the momentum corresponding to the body generating the force, Eq. (12) can be reformulated as:

$$\ddot{X}_{SRS}(\omega) = \underbrace{\Delta p_s \cdot F^*(\omega)}_{Pulse\ definition} \cdot \underbrace{\alpha(\omega)}_{Plate\ dynamics} \cdot \underbrace{-\omega^2 \cdot T(\omega)}_{SRS\ computation} \tag{13}$$

where $F^*(\omega)$ is the spectrum of a pulse with unitary momentum (the force value mainly depends on the duration τ of the pulse), $\alpha(\omega)$ is the receptance obtained considering the specific location of the input force and the output measurement, Δp_s is the momentum demanded to reach the level of the SRS requirements, and $T(\omega)$ is the transmissibility of each SRS system. More detailed explanations of the origin of this formulation and the physics it describes will be provided in Subsection 4.2.1.

Eq. (13) may alternatively be represented by the block diagram shown in Figure 14. By defining a potential impact force profile $f^*(t)$ in the time domain, possessing unitary momentum, and considering a momentum Δp_s, the actual force applied in a generic node j can be derived. The spectrum of the real force is the input of an ordinary differential equation problem solved by the FEM. Subsequently, the receptance of the plate can be calculated, taking into account the application of the force in a generic node j and the response of the plate in another generic node k. Given the response of the plate $X_k(\omega)$, the computation of the SRS acceleration involves iterative applications of the steps within the SRS block for each hypothetical SDOF system, as defined by the SRS concept. These steps include evaluating transmissibility, i.e., the displacement $X_{SRS}^{\Omega_c}(\omega)$ of each SDOF system tuned at frequency Ω_c given the input $X_k(\omega)$, and computing the maximum absolute time value associated with the c-th SDOF system.

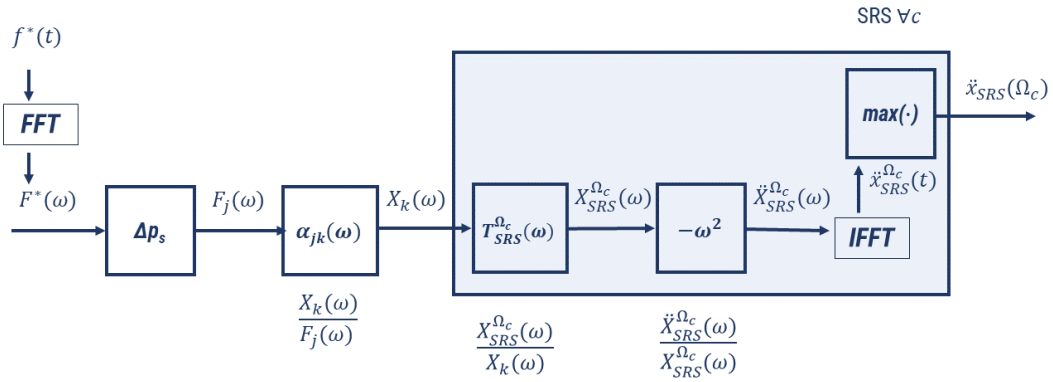

Figure 14. Block diagram describing the novel frequency domain approach laying the foundations of the proposed numerical simulation models.

4.2 Computation of the Shock Response Spectrum in the Frequency Domain

4.2.1 Convolutional Method

In this subsection, the model is investigated from a numerical point of view. The whole model is deconstructed into more manageable sub-models, each characterized by well-established equations. Specifically, the displacement of a point on a plate induced by an impulse can be delineated using convolutional equations analogous to those employed in seismic data analysis [89], assuming a given Impulse Response Function (IRF). Defining * as convolution, the displacement $x_k(t)$ can be expressed as:

$$x_k(t) = f_j(t) * h_{jk}(t) \tag{14}$$

where $f_j(t)$ is the force signal due to the impacting mass at point j, $x_k(t)$ is the displacement of the plate at point k and $h_{jk}(t)$ is the j to k IRF. In general, it is well known that IRF and FRF form a transform pair for the Fourier transform [90,91]. Hence, exploiting the convolution theorem of the FT, Eq. (14) can be easily transformed into Eq. (15), which holds in the frequency domain:

$$X_k(\omega) = F_j(\omega) \cdot \alpha_{jk}(\omega) \tag{15}$$

where $F_j(\omega)$ is the FT of the force signal at point j, $X_k(\omega)$ is the FT of the displacement at point k and $\alpha_{jk}(\omega)$ is the FRF, commonly named receptance.

The frequency domain provides the advantage of transforming the convolution operation, inherently complex in the time domain, into a significantly simpler product. This forms the essence of the frequency domain model proposed here, which proves to be more efficient and immediate compared to its time domain counterpart [92]. Moreover, any FRF expressed in terms of receptance within the context of linear MDOF systems follows a well-established formulation [90,93]:

$$\alpha_{jk}(\omega) = \frac{X_k(\omega)}{F_j(\omega)} = \sum_{r=1}^{2M} \frac{A_r}{i\omega - s_r} \tag{16}$$

where A_r are the modal constants and s_r are the complex poles. In this PhD thesis, many numerical methods for calculating the receptance of the plate will be introduced. The initial and simplest approach directly aligns with this formulation, as it employs a MDOF model in numerical computation for SRS prediction. Subsequently, the evolution of the model has led to the development of a more comprehensive method that computes the plate receptance by exploiting a FE solver.

Focusing back on the SRS computation, the acceleration of the equivalent, calibrated SDOF system, necessary for determining the SRS, can be acquired using a widely recognized FRF known as Transmissibility [94]. The relationship can be expressed as follows:

$$X_{SRS}^{\Omega_c}(\omega) = X_k(\omega) \cdot T_{SRS}^{\Omega_c}(\omega) \tag{17}$$

where $X_{SRS}^{\Omega_c}(\omega)$ is the displacement of the equivalent SDOF system mass, $X_k(\omega)$ is the previously obtained FT of the plate displacement at point k and $T_{SRS}^{\Omega_c}(\omega)$ is the transmissibility of a SDOF system with $\zeta_{SRS} = 0.05$ and a natural frequency Ω_c. This transmissibility is a fundamental FRF, whose expression can be found in the literature [94] or can be straightforwardly derived and validated to correspond to:

$$T_{SRS}^{\Omega_c}(\omega) = \frac{1 + 2r\zeta_{SRS}i}{1 - r^2 + 2r\zeta_{SRS}i} \tag{18}$$

where r is the dimensionless normalized frequency $\frac{\omega}{\Omega_c}$. Since the requirements are usually expressed as a maximax SRS acceleration at 5% of damping, the displacement $x_{SRS}^{\Omega_c}(t)$ in the time domain should be differentiated twice to obtain the corresponding acceleration $\ddot{x}_{SRS}^{\Omega_c}(t)$. Nevertheless, in the frequency domain the dual operation is a simple product by $-\omega^2$, which can be then added to the computation to derive the final equation:

$$\ddot{X}_{SRS}^{\Omega_c}(\omega) = -F_j(\omega) \cdot \alpha_{jk}(\omega) \cdot T_{SRS}^{\Omega_c}(\omega) \cdot \omega^2 \tag{19}$$

Then, given the spectrum of the input impact force $F_j(\omega)$, it is possible to directly find the corresponding $SRS(\Omega_c)$ as $\max\left(\text{abs}\left(\ddot{x}_{SRS}^{\Omega_c}(t)\right)\right)$, obtaining the time acceleration via IFT.

Such an input signal cannot be known a priori, necessitating some assumptions. According to the impulse-momentum theorem, a generic impact force $f_j(t)$ corresponds to a specific change in momentum Δp_s, represented by the area under its curve. Therefore, the impact force $f_j(t)$ can be considered as the product of the normalized force function $f^*(t)$, such that it corresponds to a unitary change in momentum, and its actual change in momentum Δp_s. In this study, the function of an elementary force $f^*(t)$ will be defined using parameters characterizing the impulse according to the principles of contact mechanics, such as the duration of contact and the coefficient of restitution. This aspect will be explored in greater detail in the subsequent sections of the thesis, as in Subsection 5.2.2. Now it can be generalized that the final frequency domain model can be written in the following form, where the decomposition of $F_j(\omega)$ leads to the following Eq. (20).

$$\ddot{X}_{SRS}^{\Omega_c}(\omega) = -\Delta p_s \cdot F_j^*(\omega) \cdot \alpha_{jk}(\omega) \cdot T_{SRS}^{\Omega_c}(\omega) \cdot \omega^2 \tag{20}$$

In numerical analysis, direct employment of the FT is unfeasible, necessitating its substitution by the Discrete Fourier Transform (DFT), the corresponding algorithm for discrete, finite signals. The DFT can be efficiently evaluated using the FFT algorithm. According to the convolution theorem, calculating convolution in the frequency domain involves straightforwardly multiplying the FT results of the input signals. As demonstrated in several studies [95,96], this procedure is particularly advantageous, especially for long signals, as it typically lowers computational burden and processing time.

4.2.2 Comparison of Time and Frequency Domain Models

The proposed semi-analytical model potentially allows for obtaining an analytical formulation of $\ddot{X}_{SRS}$. However, in practice, the analysis to derive $\ddot{X}_{SRS}$ will involve mathematical operations on digitized data. Predictive models estimate $\ddot{X}_{SRS}$ through numerical techniques, while from an experimental perspective, digital signals are acquired using computerized equipment for data processing. Regarding

regulatory standards, methods for digitally calculating the shock response spectrum are addressed in ISO 18431 [13].

Since shocks are typically defined as sudden and short-duration events, the standard provides an example of calculating the SRS on a signal identified as a reference. Indeed, SRS calculation methods can be applied to any signal. The reference signal consists of a semi-sinusoidal impulse with a duration of 11 ms and an amplitude of 10 g, as illustrated in Figure 15.

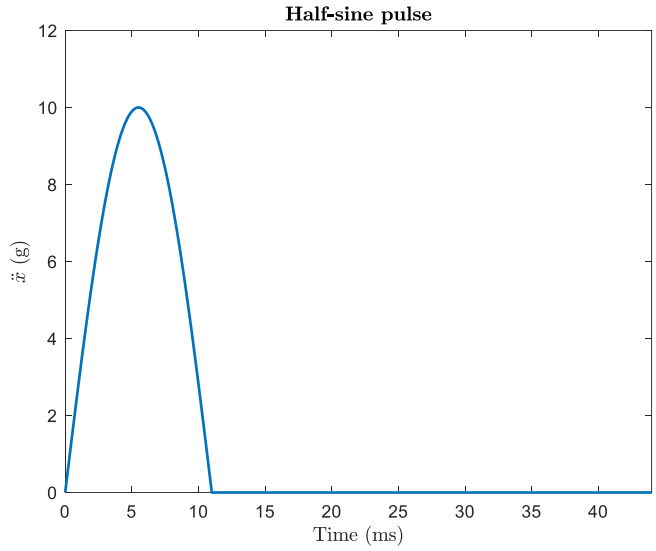

Figure 15. Semi-sinusoidal signal (with duration of 11 ms and magnitude of 10 g) considered as the input to compare the SRS computation methods.

The method for calculating the SRS proposed in this thesis, developed in the frequency domain, has been empirically validated by comparing the results obtained with those proposed by the standard, addressed in Subsection 2.2. In both cases, the acceleration signal to be analyzed is applied to the base of a set of SDOF systems characterized by their natural frequencies and Q values. For this comparison, the semi-sinusoidal signal is again considered as the input of the calculation method. According to the standard, all SDOF systems are assumed to have the same Q value of 10, corresponding to a damping coefficient of 5%.

The $\ddot{X}_{SRS}$ values obtained with the two methods are depicted in Figure 16. It can be observed that, by appropriately defining the sampling frequency f_s and the duration of the input signal T, the curve obtained with the proposed method perfectly reproduces the curve defined by ISO 18431. Calculating the Root Mean

Square Error (RMSE) between the two curves, an error on the order of 10^{-4} g is generated. Please remember that the ramp invariant algorithm adopted in the reference standard contains a bias error, dependent on the sampling frequency f_s. Therefore, the SRS calculation method utilized in this thesis can be considered verified and equivalent to the standard procedure.

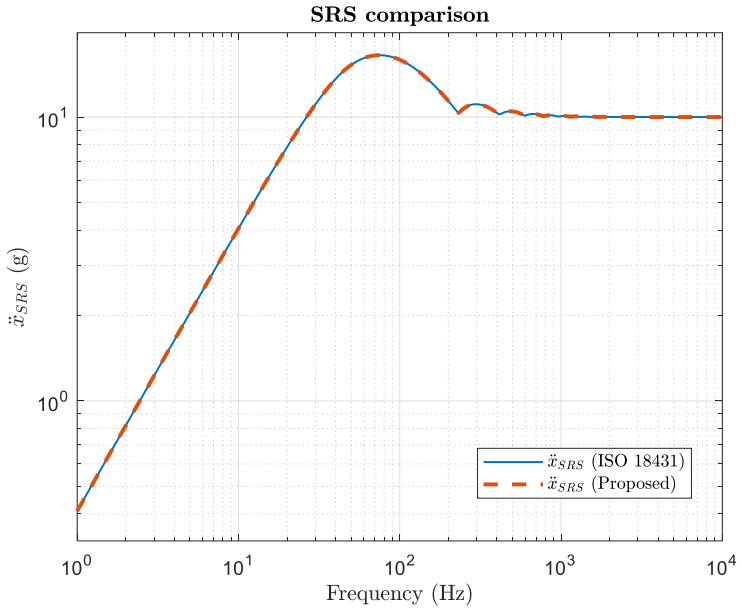

Figure 16. Comparison of the SRS calculation method proposed in this thesis (dashed red curve) with the one defined by the ISO 18431 standard (blue curve).

Chapter 5

Pyroshock Simulation Models

The proposed simulation models primarily consist of three phases: (1) a numerical analysis to derive the receptance of the plate, (2) the formulation of the impulse, and finally, (3) the computation of the SRS. The numerical analysis for obtaining the plate receptance was initially developed using a MDOF model. Subsequently, a novel implementation of an embedded Computer-Aided Design (CAD) modeler, integrated with a FE solver, was introduced to enhance both accuracy and flexibility. Both models facilitate the efficient fulfillment of varying SRS requirements, thereby reducing calibration times and yielding significant economic benefits. These models are exclusively formulated in the frequency domain, making them precise and computationally efficient. In this chapter, the models have been validated through reference to relevant literature. Moving forward in the thesis, analyses predominantly rely on the FE model, given its superior precision and integration of a greater number of parameters.

This chapter aims to introduce several methodologies for simulating an experimental configuration designed for pyroshock tests utilizing a resonant plate. The primary focus is on achieving accuracy, simplicity, and efficiency in developing each test. A detailed parametric model will serve as the reference model, playing a pivotal role in addressing the inverse problem discussed in Chapter 6. It is germane to highlight that the terms "direct" and "inverse" problem denote, respectively, the tuning of the experimental setup through the calculation of the required momentum p, and the optimal design of the test facility itself, exploiting geometry and material properties of the plate.

5.1 Multi-Degree of Freedom Model

The MDOF model was formulated to replicate the transverse dynamic characteristics of rectangular plates with varying geometries. As a two-dimensional (2D) model, it adapts to the base and height dimensions of the plate. On the contrary, the thickness exclusively influences the plate mass. Alongside these geometric parameters, the model facilitates the specification of the plate material composition (e.g., aluminum alloys, iron alloys), enabling the assignment of appropriate density values and assuming a frequency-independent constant damping coefficient ζ.

Given its nature, the model enables customization of the number of degrees of freedom by defining the number of nodes (ND_b and ND_h) along each side of the plate, as represented in Figure 17. Furthermore, the proposed model allows for the designation of the impulse generation and SRS measurement locations in terms of nodes. It also includes the test object, permitting the configuration of its dimensions, mass, and position.

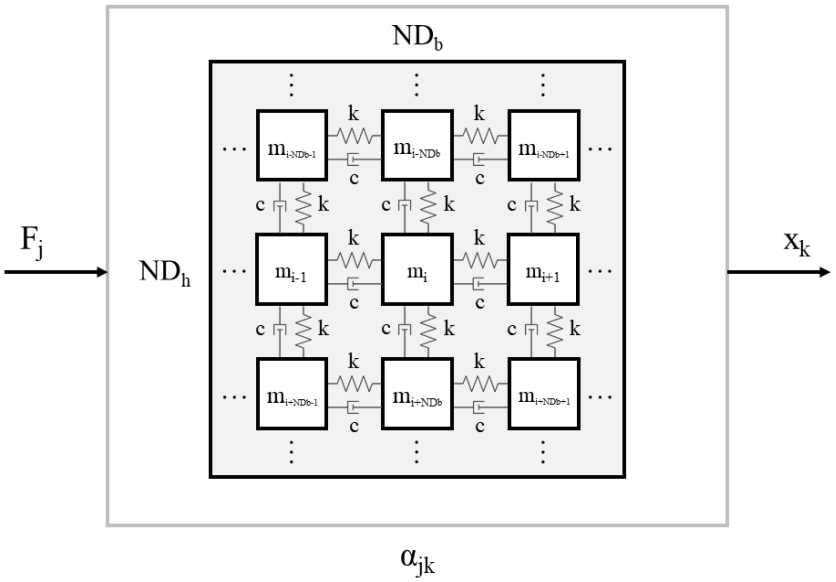

Figure 17. Scheme representing the MDOF model used to reproduce the plate behavior, considering a force F_j and the related displacement X_k in j-th and k-th node, respectively. The mass m_i represents the i-th sub-plate linked by a spring-damper system with the adjacent ones.

As explained in [97], the lumped parameter method utilizes flexibility influence coefficients. Hence, it exploits the mass concentration at discrete points, while stiffness is described using influence coefficients. This method applies to one-

dimensional and two-dimensional problems. However, it may not be feasible to derive flexibility influence coefficients for the latter, and consequently, for the specific case of the resonant plate. Given the inability to make assumptions or approximations regarding the stiffness k, a FEA has initially been conducted using dedicated software such as Autodesk Inventor or SolidWorks. This analysis aims to delineate the resonance frequencies of the pertinent modes of interest. Subsequently, the stiffness k of the MDOF model has been calibrated based on these frequencies.

The plate is partitioned into $ND_b \times ND_h$ sub-plates of uniform thickness, each contributing $\frac{1}{ND_b \times ND_h}$ to the total mass. By constructing a model wherein each sub-plate interacts with adjacent ones via a spring-damper system (characterized by stiffness k and damping c to impose a constant damping coefficient ζ), matrices representing stiffness K, damping C, and mass M are derived. The latter matrix considers both the total mass of the plate and that of the additional component under test, which has established specifications in terms of position, dimensions and mass.

Exploiting the aforementioned matrices, a modal analysis is conducted to calculate the receptance α_{jk} with the first n modes, where j and k respectively indicate the nodes where the impulse and the measurement are defined. To simulate the test configuration used by Sandia National Laboratories in [56], free boundary conditions on all four edges have been initially employed.

To validate this first proposed model, a simplified definition of the impulse described by a rectangular window may be adequate. Considering a collision accompanied by deformation and using the Hertzian contact theory, an estimation of the collision time τ can be derived as proposed in [73]:

$$\tau = 3.29 \cdot (1 - \nu^2)^{\frac{2}{5}} \left(\frac{m_s^2}{RE^2 u_s} \right)^{\frac{1}{5}} \tag{21}$$

where ν and E are respectively the Poisson's ratio and the Young's modulus of the material, m_s, R and u_s are respectively the mass, the radius and the velocity of the impacting object.

The validation of the proposed method is demonstrated through comparison with experimental results conducted by Sandia National Lab [56]. Table 3 provides

a summary of the plate characteristics and configuration parameters of the model (in the specific validation case $M = 51 \times 51 = 2601$ DOFs have been adopted).

Table 3. Characteristics of the resonant plate and associated parameters configurating the MDOF model.

Quantity	Value	Notes
Base	500 mm	divided in 51 nodes
Height	500 mm	divided in 51 nodes
Thickness	38.1 mm	
Material	aluminum	$\rho = 2700$ kg/m^3; $\zeta = 0.05$
Plate mass	25.72 kg	
Pulse position	central	
Measuring position	central	
Mass under test	0 kg	

Figure 18 demonstrates how the MDOF model, suitably calibrated to match the FEM plate, reproduces the experimental outcomes in a partial accurate manner. In fact, the slope of the simulated and experimental curves differs at low frequencies, while the prediction is accurate above 500 Hz. However, the quality of the obtained results allows to faithfully estimate the variation of momentum Δp_s, determined minimizing the Root Mean Square Error (RMSE) between the experimental and simulated curves. Furthermore, Figure 19 shows the obtained modal shapes of the first 13 modes of the resonant plate. Given the imposed free boundary conditions, the first mode concerns the plate rigid translation and, consequently, has not been reported as not relevant. It is evident that only certain modes give an effective contribution, considering the position of the test object and the impact.

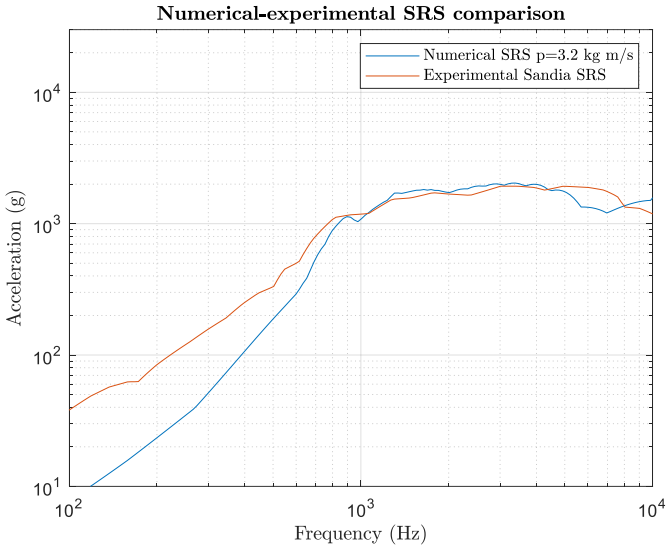

Figure 18. Comparison between the simulated plate SRS and the experimental results obtained with the Sandia reference plate.

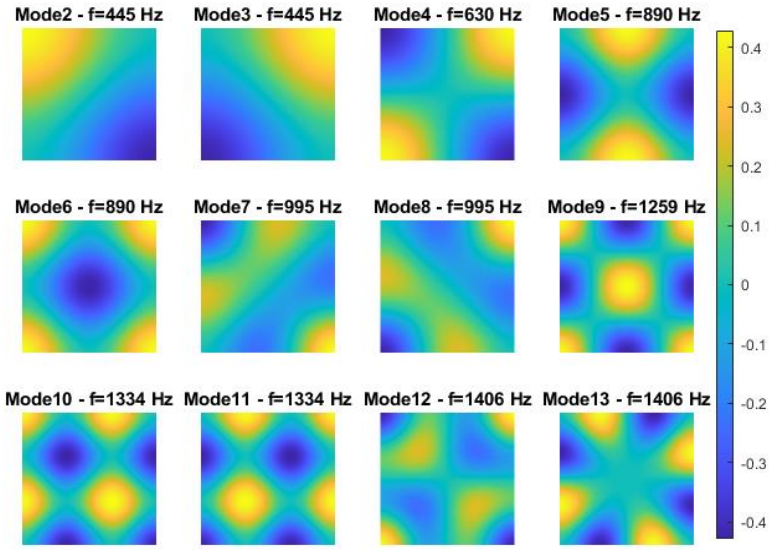

Figure 19. Modal shapes of the first 13 modes of the reference resonant plate.

Given that some parameters have been assumed due to lack of information, the proposed comparison allowed the verification of the tuning in terms of the determination of measurement and impact positions, the mass and velocity of the impacting body. In particular, assuming to apply the impulse through a projectile generating

a totally elastic impact, the mass and velocity of the impacting object to reach the SRS requirements are estimated equal to $m_s = 0.53$ kg and $u_s = 3$ m/s.

To enable a more comprehensive simulation of a pyroshock test, it is possible to implement the simulation of the system behavior during a component qualification test. By setting the mass and dimensions of the test object, its optimal position and the updated specifications for generating the impact can be determined. Figure 20 illustrates the discretization of the resonant plate, with nodes highlighted in blue indicating areas where the test object contributes as a massive element. Figure 21 presents the outcomes obtained by incorporating a 7.5 kg object (divided into a 13×13 node grid) positioned at the center of the plate.

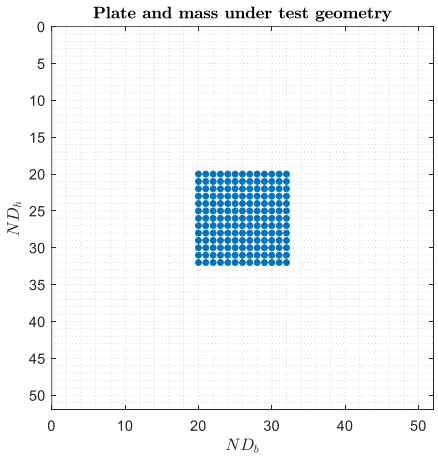

Figure 20. White represents the discretization of the resonant plate, blue indicates the position of the test object with discrete geometry.

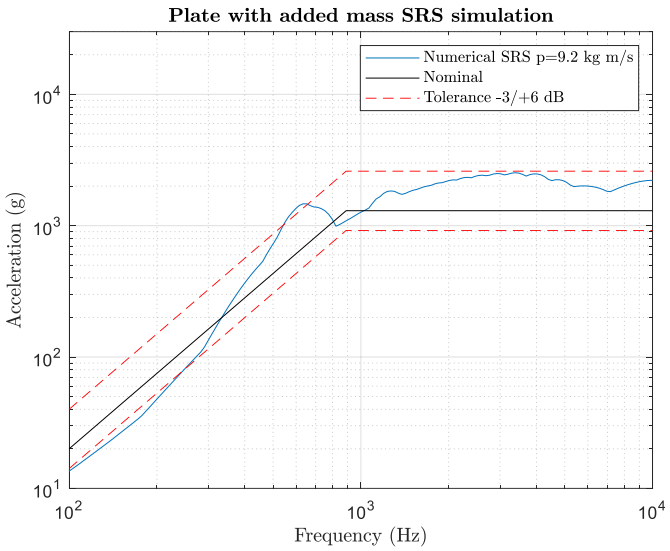

Figure 21. Numerically simulated SRS of the resonant plate with the additional mass of the test component.

To conclude, this first approach through the present parametric MDOF model allows to numerically simulate a pyroshock test with good approximation. This model facilitates the calibration process under varying experimental conditions and requirements, offering a first satisfactory SRS prediction. The SRS profile derived from simulation exhibits a trend similar to experimental observations, thereby validating the usefulness of the proposed model. Moreover, the computational burden of this model is moderate, resulting in expedited algorithm processing. This model anticipates the following enhancements to further improve the accuracy by considering a more comprehensive number of factors and exploiting a FE solver.

5.2 A Comprehensive Parametric Model

To address the limitations of the MDOF model and enhance simulation outcomes, a comprehensive parametric model was developed. While the MDOF model produced satisfactory results in terms of simulated SRS within a short processing time, it entails simplifications that may compromise result accuracy favoring computational efficiency. Therefore, exploiting a similar conceptual framework and operating entirely within the frequency domain, the improved comprehensive parametric model introduces an innovative integration of a CAD modeler into the MATLAB environment. This integration enables the derivation of the FRF of the plate via a FEM solver. This second proposed model facilitates the simulation of the dynamic behavior along all three plate dimensions, fulfilling variable and

potentially intricate geometries. Additionally, certain aspects previously subject to approximation, such as impulse definition and geometric complexity, are further analyzed. From now on the simulation results will refer to the following comprehensive parametric model, as it is considered as a reference given its superior performance.

To provide a general overview, the whole simulation model is composed of the three macro-phases depicted in Figure 22: (1) the FEM analysis, (2) the pulse definition, and (3) the SRS computation. Block diagrams in Figure 23 expand each macro-phase to entirely describe the simulation model, highlighting the numerous parameters involved in each subphase. These parameters are described in detail in Table 4. It is worth noting that the block diagram represents the same mathematical steps formulated in Eq. (13). For the sake of completeness, the optimization flows that are described in the continuation of this Ph.D. thesis have also been included in the chart.

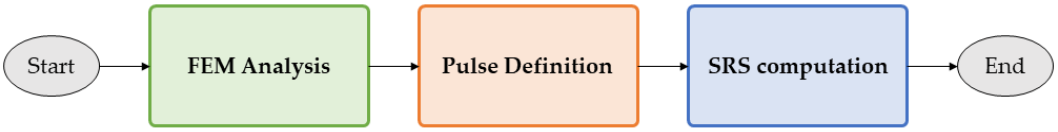

Figure 22. Block diagram summarizing the macro-phases constituting the structure of the numerical model.

5.2.1 Finite Element Method Analysis

The objective of the FE-based model is to compute the FRF of the resonant plate. The geometry of the resonant plate, along with the anvil plate and the specimen, can be parametrically defined by the CAD software, which is OpenSCAD [98]. This CAD tool facilitates the generation of complex geometries while preserving parametric flexibility, a crucial aspect particularly relevant to facing the inverse problem (i.e., plate design). The 3D problem is figured out by means of a frequency response analysis.

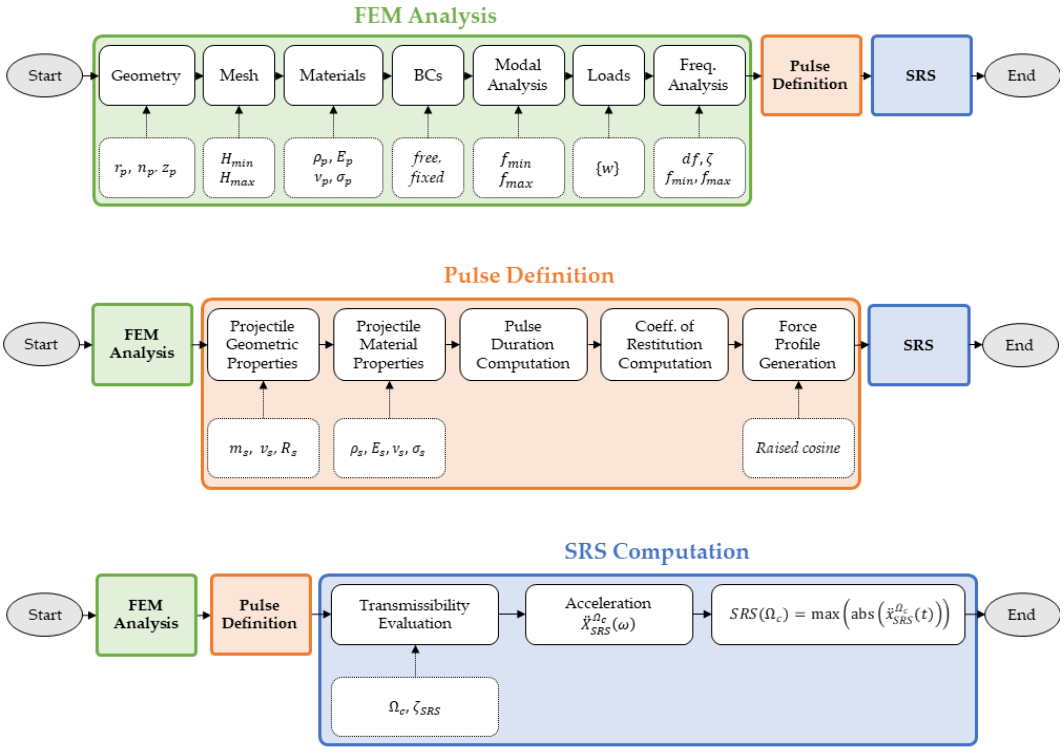

Figure 23. Block diagrams expanding the description of the model for the simulation of pyroshock tests. The parameters (which can be defined or unknown) involved in each macro-phase are highlighted.

The first step to obtain the FRF of the plate consists in setting the geometry. This aspect is highly flexible as it is possible to generate plates with simple (e.g., cuboid) and complex shapes (e.g., irregular shapes with geometric discontinuities, and holes). In general, according to the case under analysis, the parameters in question can describe the dimensions of a cuboid rather than the Cartesian coordinates of the vertices of an irregular solid. Furthermore, the flexibility of this generated CAD model allows including one or more components in the analysis. Hence, for example, only the resonant plate can be studied for a comparison with the experimental data or its correct tuning, otherwise the anvil plate and the specimen can also be included to predict the SRS obtainable under specific conditions. Please note that these last two elements can be placed in any position with respect to the main plate by varying the parameters $\{u_i\}$, $\{u_o\}$. The latter also determine the positions that define the impulse application and the output acceleration measurement.

Table 4. List and description of the parameters present in the proposed model.

Parameter	Description
$\boldsymbol{x, y, z}$	Components dimensions (in case they are assumed to be cuboids). Alternatively, to evaluate more complex geometries, these dimensions can be replaced with vectors of Cartesian coordinates representing the vertices of components.
$\{\boldsymbol{u_i}\}, \{\boldsymbol{u_o}\}$	Coordinate vector to establish the position of the elements (i.e., anvil plate and specimen) with respect to the plate and, consequently, the impact and the measurement positions.
$\boldsymbol{H_{min} - H_{MAX}}$	Minimum and maximum dimensions for the mesh generation.
$\boldsymbol{\rho}$	Density.
$\boldsymbol{E}$	Young's modulus.
$\boldsymbol{\nu}$	Poisson's ratio.
$\boldsymbol{G}$	Shear modulus.
$\boldsymbol{\sigma}$	Yield stress.
$\boldsymbol{BCs}$	Boundary conditions of the resonant plate (e.g., free-free, clamped-free, clamped-clamped, etc.).
$\{\boldsymbol{w}\}$	Vector establishing the direction of the applied impulse. The magnitude must necessarily be unitary.
$\boldsymbol{f_{min} - f_{MAX}}$	Minimum and maximum frequency to define the range of interest for the (modal and frequency) analyses.
$\boldsymbol{df}$	Frequency resolution.
$\boldsymbol{\zeta}$	Damping coefficient (depending on the materials properties).
$\boldsymbol{m}$	Mass.
$\boldsymbol{v}$	Velocity.
$\boldsymbol{p}$	Momentum.
$\boldsymbol{R}$	Radius of curvature.
$\boldsymbol{\tau}$	Pulse duration.
$\boldsymbol{e}$	Coefficient of restitution.
$\boldsymbol{sh}$	Shape of the impulse force profile (e.g., rectangular, half-sine, raised cosine = Hann, etc.).
$\boldsymbol{\Omega^c_{SRS}, \zeta^c_{SRS}}$	Natural frequencies and damping coefficients of the c-th SDOF systems defined by the SRS. Typically, Ω^c_{SRS} is tuned to obtain a minimum frequency resolution of 1/24 of octave and $\zeta^c_{SRS} = 0.05$.

After establishing the geometry of the system under analysis, it is necessary to generate a suitable mesh. The parameters H_{min} and H_{MAX} control the minimum and maximum size of the elements. Their choice is decisive for finding the best trade-off between the accuracy of results and calculation time. In this regard, ESA provides some rules to increase the FE model fidelity at high-frequency.

The minimum and maximum sizes of the mesh elements are recommended in [12] to limit the CPU time and avoid numerical errors. Specifically, the maximum mesh size depends on the minimum wavelength associated with the propagation of compression, shear, and flexural waves. It is suggested to employ at least 8 elements per wavelength to mitigate wave reflection or numerical filtering. Conversely, the minimum mesh size should not exceed 16 elements per wavelength, as doing so would escalate computation time without a corresponding improvement in results. Formulas for calculating the aforementioned wavelengths are delineated in Eq. (22)-(24).

$$\lambda_{compression} = \frac{\sqrt{E/\rho}}{f_{MAX}} \tag{22}$$

$$\lambda_{shear} = \frac{\sqrt{G/\rho}}{f_{MAX}} \tag{23}$$

$$\lambda_{flexural} = \left(\frac{2\pi}{f_{MAX}}\right)^{\frac{1}{2}} \left(\frac{Ez^2}{12\rho}\right)^{\frac{1}{4}} \tag{24}$$

Before proceeding with the analysis, materials need to be assigned to the various generated components. This entails associating mechanical properties corresponding to each material (e.g., iron alloys, aluminum alloys) with all individual components. The masses of these components will vary depending on the designated material and the dimensions specified in the geometry. Note that the optimization of this aspect, in the context of an inverse problem, results in the best choice among the different considered materials.

Boundary Conditions (BCs) can also be set in the present model. Experimental setups for pyroshock tests usually operate free-free conditions. However, it is also possible to constrain some portions, faces or edges of the plate thanks to the BCs parameter.

Before conducting the frequency analysis, it is necessary to define the load applied on the system under examination. Following the mathematical procedures outlined in Eq. (13), an ideal unitary pulse is employed in this stage. This facilitates the study of plate behavior ignoring the applied pulse, thereby allowing for the independent development of insights into pulse characterization at a later stage. Subsequently, the optimal momentum p can be derived to fulfill the requirements of each test. The only parameter that can be set in this phase is the vector $\{w\}$ which establishes the direction of the applied impulse. Typically, this vector is perpendicular to one face of the plate.

The analysis of the system described so far can be confined to a frequency range delimited by f_{min} and f_{MAX}. Determining these two parameters, along with H_{min} and H_{MAX}, is essential to achieve an optimal balance between accuracy and computational efficiency. Typically, the frequency range of $10^2 - 10^4\ Hz$ is employed, as the test requirements (as well as the guidelines initially introduced) are established in this frequency band. The results obtained from this modal analysis are also interesting for understanding the contribution of each mode as the input and output positions vary (respectively, the pulse application and the signal measurement).

To conclude this first macro-phase of the model, the FEM analysis ends with the solution for the frequency analysis of the plate. In addition to the already established frequency range $f_{min} - f_{MAX}$, it is possible to set the frequency resolution df and the damping coefficient function $\zeta(\omega)$. The latter depends on the previously defined materials and can usually be assumed constant in frequency. On the other hand, the df parameter also influences the accuracy of the results and the calculation times of the algorithm, necessitating careful calibration to achieve a balance between these aspects. The integration of all these steps and the combination of all these parameters facilitate the derivation of the receptance $\alpha(\omega)$ of the plate, crucial for the final SRS calculation.

5.2.2 Pulse Definition

The definition of the pulse represents a crucial aspect in obtaining the SRS acceleration. The spectrum $F(\Omega)$ of the pulse can significantly affect the plate response due to its inherent nature. Indeed, as an impulse is characterized by a very short duration, its spectrum is distinguished by being broad in frequency. However, when considering very wide frequency ranges, it generally behaves similarly to a low-pass filter, with the cutoff frequency predominantly determined by the duration of the impulse itself. Apart from influencing the SRS profile results, this phase is

instrumental in delineating parameters inherent to the impacting object (e.g., bullet, hammer, pendulum). These parameters enable the solution of the direct problem, entailing the simulation of the behavior of the experimental setup under specific conditions to obtain the momentum p_s necessary to satisfy the specific requirements.

The initial phase of the impulse definition involves the declaration of the characteristics (mass m_s, velocity u_s, and radius R_s) and the materials of the impacting body, thereby setting its mechanical properties. Since the solution of the direct problem entails identifying parameters to properly tune the test facility, the impact body characteristics might constitute the unknown quantities to determine. Typically, parameters such as mass, velocity, and projectile radius are adjusted iteratively to meet test requirements efficiently. However, since these values are essential for subsequent impulse definition, initial plausible estimates can be set. Through iterative refinement of the impulse generation process, the characteristics of the impacting body converge to numerical values consistent with the physics of the problem.

After setting the properties of the impacting body, it is possible to define the force-time pulse curve by establishing three main characteristics: the impact duration, the coefficient of restitution and the function describing the curve. For the estimation of the impact duration, reference is made initially to the Hertz contact theory, considering the collision accompanied by a deformation. Indeed, this theory establishes a relationship between the force applied at the contact area between two bodies and the displacements (specifically, compression on two surfaces), as well as the material properties of the bodies involved. Particularly, Hertz's theory enables the calculation of this relationship by treating bodies as spherical, homogeneous, and isotropic [71–73]. However, the scenario under consideration deals with a collision between the impacting body (which can be approximated as a sphere with radius R_s) and a plate (having a flat surface). For this reason, the collision time τ is obtained with Eq. (25) as in [74]:

$$\tau = 2.9432 \cdot \left[\frac{15 m_s \left(\frac{1-\nu_s^2}{E_s} + \frac{1-\nu_p^2}{E_p} \right)}{16\sqrt{R_s u_s}} \right]^{\frac{2}{5}} \tag{25}$$

It can be observed that the impact duration τ depends on various parameters related to the mechanical properties of the bodies (E and ν, both of the plate and projectile), to the physical and geometric properties of the sphere (R_s and m_s) and to the characteristics of the impact itself (u_s). In particular, the total duration of the contact τ assumes an elastic collision and, consequently, is twice the time necessary to reach the maximum compression. The dimensionless numerical value in Eq. (25) takes it into account and is obtained from the elliptic integral over the compression.

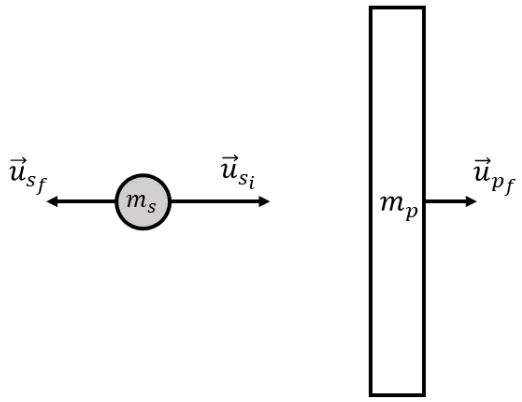

Figure 24. Diagram of the collision between the impacting body (represented as a spherical object) and the resonant plate, highlighting the related mass and speed properties before and after collision.

Hertz's contact theory, with its assumption of perfect elasticity of the involved bodies, limits the obtained results since a real impact - as inelastic - causes an energy loss. For this reason, the coefficient of restitution e is further introduced, defined as the ratio between the relative speeds after and before the collision (i.e., separation and approach). Considering that all the kinetic energy of the system is originally contained in the sphere since the plate is initially at rest, it is possible to apply the conservation of momentum to the system shown in Figure 24:

$$\Delta\vec{p}_p = \Delta\vec{p}_s = m_s\vec{u}_{s_f} - m_s\vec{u}_{s_i} \tag{26}$$

$$|\Delta\vec{p}_s| = m_s u_{s_f} + m_s u_{s_i} \approx m_s u_{s_i}(1+e) \tag{27}$$

where the second subscripts i and f respectively indicate the sphere speed before and after the impact. Thanks to the application of the coefficient of restitution

in Eq. (27), it is possible to consider part of the aspects shown in the energy balance in Figure 25. Indeed, it can be considered that, after the impact, the initial kinetic energy of the sphere K_s is distributed: partly reflected within the sphere as post-contact (restitution) kinetic energy K_{res}, partly transmitted to the plate in the form of kinetic energy due to its rigid translation K_p (applicable in free-free conditions) and vibrational energy $E_{p_{vibr}}$ (useful component for pyroshock tests) and, finally, partially dissipated due to some physical phenomena E_{diss} (including the inelastic collision itself). While these aspects are currently simplified and summarized in the coefficient of restitution, further investigation could provide deeper insights. For instance, the coefficient may vary with the impact position relative to the plate, although such influence is assumed to be minor and therefore negligible in the present context.

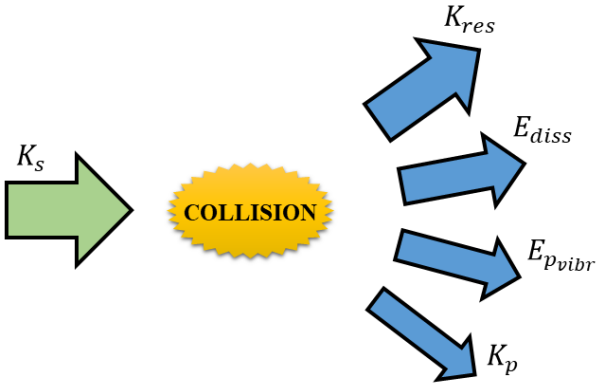

Figure 25. Energy balance diagram of impacts simulating pyroshocks. The provided kinetic energy K_s of the impacting body transforms into post-contact kinetic energy K_{res} of the same impacting body, dissipated energy E_{diss}, vibrational energy $E_{p_{vibr}}$, and kinetic energy K_p of the resonant plate.

From Eq. (27) it can be further deduced that the impact force profile can never be assumed to be symmetrical, precisely because of the coefficient e. Indeed, by considering the area under the force curve as a function of time during the sphere-plate contact, it is possible to deduce the depiction illustrated in Figure 26 and Eq. (28), where τ indicates the duration of the impulse.

$$\int_0^{\tau} \mathrm{F(t)dt} = m_s u_{s_i}(1+e) \tag{28}$$

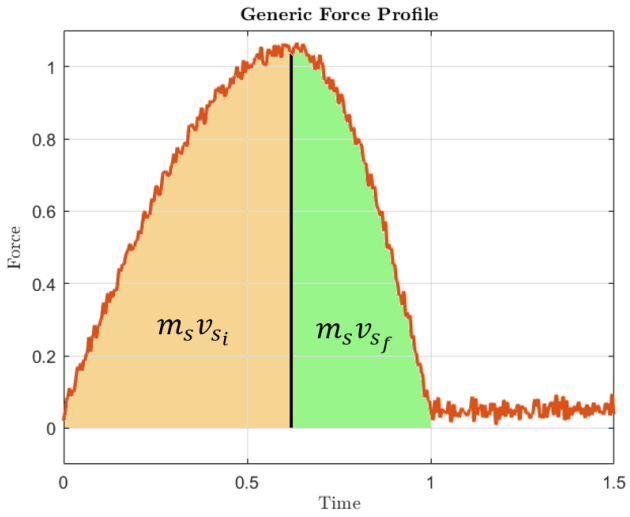

Figure 26. Representation of a generic impulsive force profile to highlight the effect of the coefficient of restitution e on the area under the curve. The force and time values have been normalized respectively with respect to the maximum value and the pulse duration τ.

The estimation of this crucial coefficient, which regulates the energy dissipation in the proposed model, is evaluated by referring to a couple of the best-known analytical formulations to consider the impact between a sphere and a plate. Among the many dissertations for estimating the COR, Zener's theory [85] is highlighted since it better assesses the e value when the plate has a thickness much smaller than the sphere diameter. On the contrary, Weir-Tallon's theory [86] gives better estimates if the plate has dimensions of the order of magnitude or greater than the diameter of the impacting object (as demonstrated experimentally in [99]). Since the plate does not have a totally negligible thickness in most cases, Eq. (29) reports Weir-Tallon's formula to estimate e:

$$e = \frac{3.1}{\rho_s^{1/8} \cdot \left(\frac{1-\nu_s^2}{E_s} + \frac{1-\nu_p^2}{E_p}\right)^{-\frac{1}{2}}} \cdot \left[\frac{\min\left(\sigma_s, \sigma_p\right)^5}{u_s^2}\right]^{\frac{1}{8}} \tag{29}$$

where $E_{s,p}$, $\nu_{s,p}$, and $\sigma_{s,p}$ are the mechanical properties of the materials constituting the bodies involved in the impact. Finally, the impulse is also defined by the

shape of the force profile through the sh parameter (which does not have a numerical value, but qualitatively defines the shape typology). This aspect had been initially simplified in the MDOF model by assuming the impulse with a rectangular force profile in the time domain. Given that some studies in the literature investigate the force profiles generated by impact tests [100–102], alternative profiles are proposed in this phase to ensure that the impulse reflects more faithfully the actual physical phenomenon. For this reason, functions such as the (half-)sine or the raised cosine (i.e., Hann window) can be used to define the impulse force profiles. It should be remembered that these curves have been deformed – according to the principle shown in Figure 26 – in order to obtain an asymmetrical shape (as a consequence of the coefficient of restitution) and their duration is determined by the τ parameter. Furthermore, these pulses are generated in the time domain and subsequently transformed into the frequency domain. Therefore, the previously defined parameters df and f_{MAX} also affect this pulse generation in the time domain, as they set the temporal discretization $dt = \frac{1}{2f_{MAX}}$ and the duration $T = \frac{1}{df}$. The df and f_{MAX} choice is relevant since it must also consider the possibility of defining the impulse force profile with good precision. In addition to these analytical functions, experimental signals acquired with impact tests could be used. For instance, a high-frequency shock load signal was recorded in [52] during pyroshock simulation tests. Figure 27 shows some qualitative shapes of impact force profiles, both in the time and frequency domain. It is worth noting how the pulse definition affect the final SRS since the related spectra of the pulses could significantly differ. These aspects might be further investigated to reproduce the load behavior during an impulse in a more precise manner and, therefore, to improve its characterization.

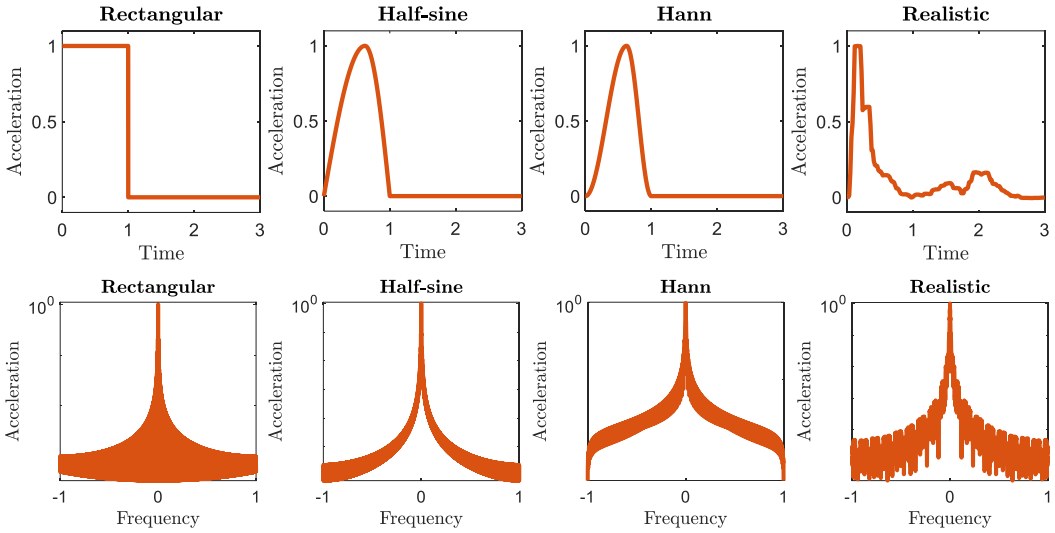

Figure 27. Qualitative representation of the force profiles adopted in the pulse definition phase. It is worth noting that the half-sine and Hann curves have been modified according to the effect of the coefficient of restitution e, which makes the profiles asymmetrical. The first row represents the time signals, normalized with respect to the maximum value and the effective pulse duration τ. The second row shows the related spectra, normalized with respect to the sampling frequency f_s.

5.2.3 SRS Computation and Score Functions

Once the plate FRF and the impulse spectrum have been computed, the derivation of the SRS acceleration becomes necessary to simulate the behavior of the experimental pyroshock test facility and compare it versus specific requirements, as depicted by the product in Eq. (13). It is important to recall that the SRS serves as a representation of how a theoretically infinite number of SDOF system with different natural frequencies responds to a shock input, which is an arbitrary transient acceleration. As already mentioned, if no SRS information is specified, reference is made to the maxi-max SRS. This represents the maximum absolute recorded response of a series of SDOF systems, having natural frequencies Ω_{SRS}^{c} tuned to achieve a minimum frequency resolution (set to 1/24 octave) and damping coefficient $\zeta_{SRS}^{c} = 0{,}05$. It is thus possible to obtain the desired SRS by exploiting the transmissibility T of a mass-spring-damper system with these characteristics. This calculation necessitates repetition for each SDOF system delineated by the SRS. To provide an alternative perspective, the different tuned SDOF systems filter the signal with respect to their transmissibility and provide information on the maximum acceleration that can be reached.

To compare the numerical results with the requirements of the pyroshock simulation tests and determine the necessary momentum p_s to minimize deviation from these requirements, a score function is introduced for this minimization task. Currently, there is no standardized recommendation or unified evaluation metric for such purposes, despite the prevalent use of score functions in the Machine Learning (ML) field. Commonly utilized evaluation criteria include the Mean Square Error (MSE) and its variant Root Mean Square Error (RMSE), the Mean Absolute Error (MAE) along with its variants such as Mean Absolute Percentage Error (MAPE) and Symmetric Mean Absolute Percentage Error (SMAPE), and the coefficient of determination R^2, which quantifies the ratio of the variance of the dependent to the independent variables [103]. Given that the RMSE is the most widely used criterion for evaluating the models, while MAE may offer greater statistical robustness in certain scenarios [104], these two metrics are primarily employed as score functions in this context. Nevertheless, there is nothing to prevent the use of other criteria, such as those aforementioned, based on their suitability for the specific application. The equations representing potential score functions are:

$$RMSE = \sqrt{\frac{1}{n}\sum_{\Omega_c=f_{min}}^{f_{MAX}} \left(\ddot{X}_{SRS}(\Omega_c) - \ddot{X}_r(\Omega_c)\right)^2} \tag{30}$$

$$MAE = \frac{1}{n}\sum_{\Omega_c=f_{min}}^{f_{MAX}} \left|\ddot{X}_{SRS}(\Omega_c) - \ddot{X}_r(\Omega_c)\right| \tag{31}$$

where $\ddot{X}_{SRS}(\Omega_c)$ is the calculated value of the acceleration expressed in g referred to the c-th SDOF system on n total (synchronized to the resonant frequency Ω_c) for the SRS calculation, $\ddot{X}_r(\Omega_c)$ is the test requirement (or the generic reference curve) in terms of SRS acceleration. Furthermore, it is specified that the related variants adapted in a logarithmic scale could also be used to balance the error over the whole considered spectrum, as in Eq. (32)-(33). These logarithmic variants are commonly known as Root Mean Squared Logarithmic Error (RMSLE) and Mean Absolute Logarithmic Error (MALE).

$$RMSLE = \sqrt{\frac{1}{n}\sum_{\Omega_c=f_{min}}^{f_{MAX}} \left(\ln\left|\ddot{X}_{SRS}(\Omega_c)\right| - \ln\left|\ddot{X}_r(\Omega_c)\right|\right)^2} \tag{32}$$

$$MALE = \frac{1}{n}\sum_{\Omega_c=f_{min}}^{f_{MAX}} \left|\ln\left|\ddot{X}_{SRS}(\Omega_c)\right| - \ln\left|\ddot{X}_r(\Omega_c)\right|\right| \tag{33}$$

Recalling Eq. (13), it is possible to obtain the momentum Δp_s – and consequently the pair of values m_s and u_s – necessary to minimize the generic score function (whose evaluation parameter is hereafter called $score = RMSE,\ MAE,\ RMSLE,\ MALE$ or any other possible variants).

5.3 Validation of the FE-based Model

This section presents the outcomes obtained through the complete simulation (direct problem), exploiting the FE model to compute the receptance (or equivalently, the inertance) of the resonant plate. Specifically, the simulation results are compared with the experimental findings documented in [58] for the purpose of model validation. This particular reference was selected due to its comprehensive detailing of the test bench setup, which proves indispensable for configuring the model parameters. Additionally, exhaustive datasets encompassing pyroshock qualification tests are currently limited in the literature. Jonsson's development of a test bench for pyroshock tests, as depicted in Figure 28, serves as a reference, considering the complete list of parameters documented during the tests. This level of detail assists in configuring the model as accurately as possible. However, given that not all necessary information is available, the remaining parameters are assumed based on the presumed execution of the tests. Consequently, any discrepancies between numerical and experimental results may be partly attributed to these approximations/assumptions. Model validation includes various experimental configurations to verify the accuracy of the results under differing operating parameters.

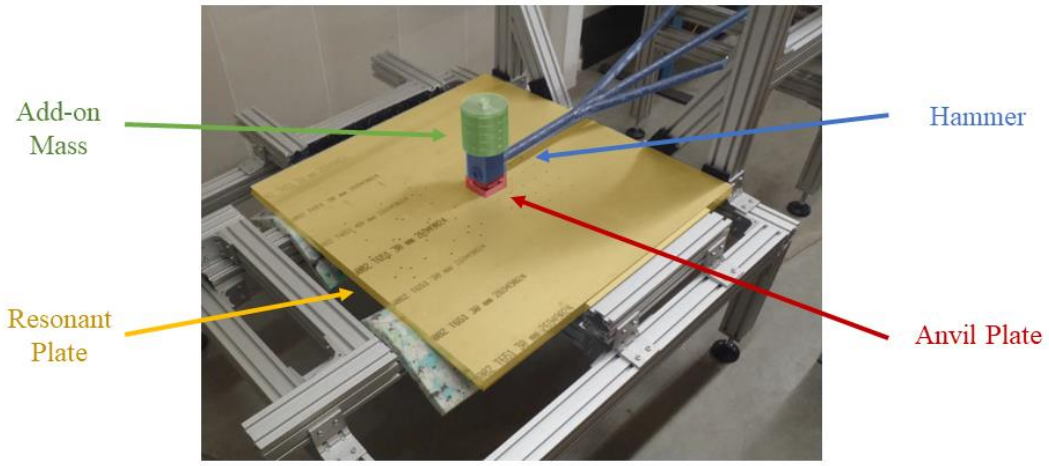

Figure 28. Test facility designed in [58] and used for validating the proposed numerical model, by comparing the experimental and predicted SRS curves.

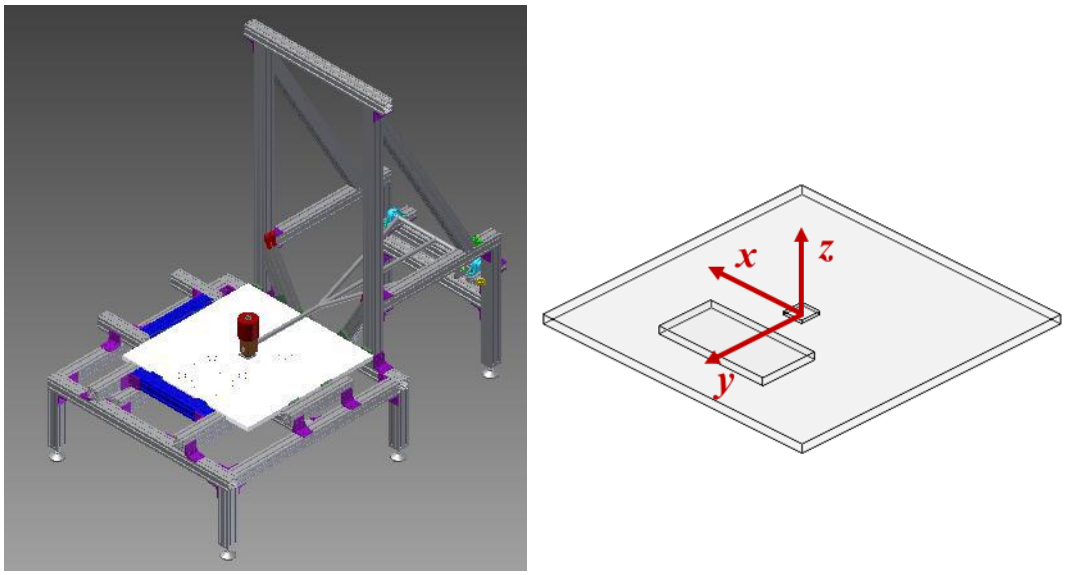

Figure 29. On the left, the CAD model of the reference test facility proposed in [58]. On the right, the integrated CAD model and its reference system generated by adopting the present methodology. Specifically, this configuration is specific to Test #2 in Table 5.

The model underwent validation through a comparison of the experimental and simulated SRS. To ensure the robustness and versatility of the model across varying operating parameters, two distinct configurations were chosen for validation. These configurations were selected to prove the efficacy of the model under different conditions and to provide a comprehensive validation process. The simulations were performed by considering a resonant plate with the characteristics summarized in Table 5, and the related results are shown respectively in Figure 30 and Figure 32.

In both cases, a mesh with quadratic tetrahedral elements was adopted, while the refinement of the mesh was determined using Eq. (22)-(24). In particular, the target minimum and maximum mesh edge lengths were set equal to $H_{min} = 18.6$ mm and $H_{MAX} = 37.3$ mm. Figure 29 represents the geometry defined in the present model with reference to Test #2 in Table 5. Furthermore, it has the purpose of showing the reference system adopted in the analyzed cases.

Table 5. Characteristics of the resonant plate used during the experimental reference tests. The superscript * indicates the parameters estimated on the basis of the data provided in [58].

Parameter	Test 1	Test 2
Plate dimensions	1 x 1 x 0.03 m^3	1 x 1 x 0.03 m^3
Plate material	Al6082	Al6082
Impact location	(-0.15 m; -0.15 m)*	(0 m; 0 m)
Measurement location	(-0.15 m; 0.15 m)*	(0 m; 0.325 m)*
Impact velocity	≈3.7 m/s*	≈1.7 m/s
Anvil plate material	Al7075	Al7075
Anvil plate dimensions	7 x 7 x 1 cm^3	7 x 7 x 1 cm^3
Boundary conditions	Free	Free
Hammerhead material	SS303	SS303
Hammerhead curvature	0.2 m*	0.2 m*
Hammer mass	3.5 kg*	3.5 kg*
Hammerhead add-on mass	0 kg	2 kg
Specimen size	No specimen	0.4 x 0.2 x 0.025 m*
Specimen mass	0 kg	6.3 kg
Force profile shape	Step	Hann

In the first configuration, no object under test was included to eliminate potential confounding factors. The results presented in Figure 30 indicate that the developed model faithfully reproduces the physical behavior of the test facility, as evidenced by the comparison with experimental data. Notably, there is a satisfactory agreement between the frequencies of SRS peaks, their amplitudes, and the overall curve trend. The major inaccuracies can be observed at low and high frequencies.

As mentioned above, these discrepancies may be partly due to the estimation and assumption of unknown parameters, despite efforts to derive them accurately from available data in [58]. Parameters such as impact and measurement locations, hammerhead curvature, and specimen size were derived from graphical representations, figures, and indirect measurements. For instance, the impact velocity was determined as a linear interpolation of the known velocities as a function of the charge angle of the pendulum. Similarly, the hammerhead mass was derived from an estimation of its geometric dimensions (approximately equal to $0.07 \times 0.07 \times 0.09$ m^3), considering a steel composition. The resulting inaccuracies may also be due to the choice of the impulse force profile, as well as the definition of the damping coefficient ζ. In fact, these aspects are very complex and could require further investigations to obtain even more accurate results. For instance, the fact that the first peak of the measured curve is less prominent than the simulated one can depend on the frequency-dependent damping of the system and on the boundary conditions.

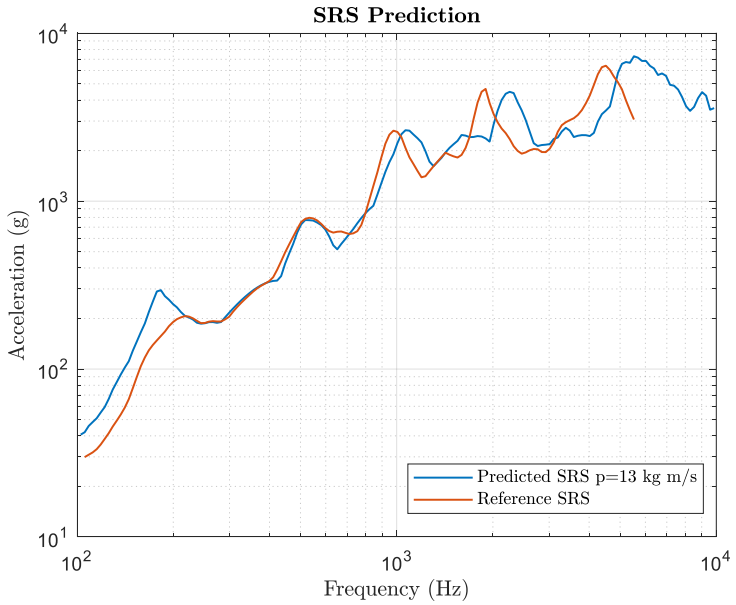

Figure 30. Comparison of the SRS simulated by the present model (in blue) with the experimental one (in red) obtained in [58]. The model parameters were set as reported in the Test #1 column of Table 5.

A transient analysis was conducted using the commercial software SolidWorks 2022 to compare its results with the proposed model. The same system configuration and parameters were employed to compute the system response in the time

domain. As depicted in Figure 31, the responses obtained from both models exhibit a high degree of coherence over time. Moreover, Figure 31 includes the frequency responses to facilitate a deeper understanding of the differences between the two results. While both models effectively describe the modes up to approximately 2 kHz with noteworthy precision, it is evident that only the proposed model provides accurate results over the entire frequency spectrum.

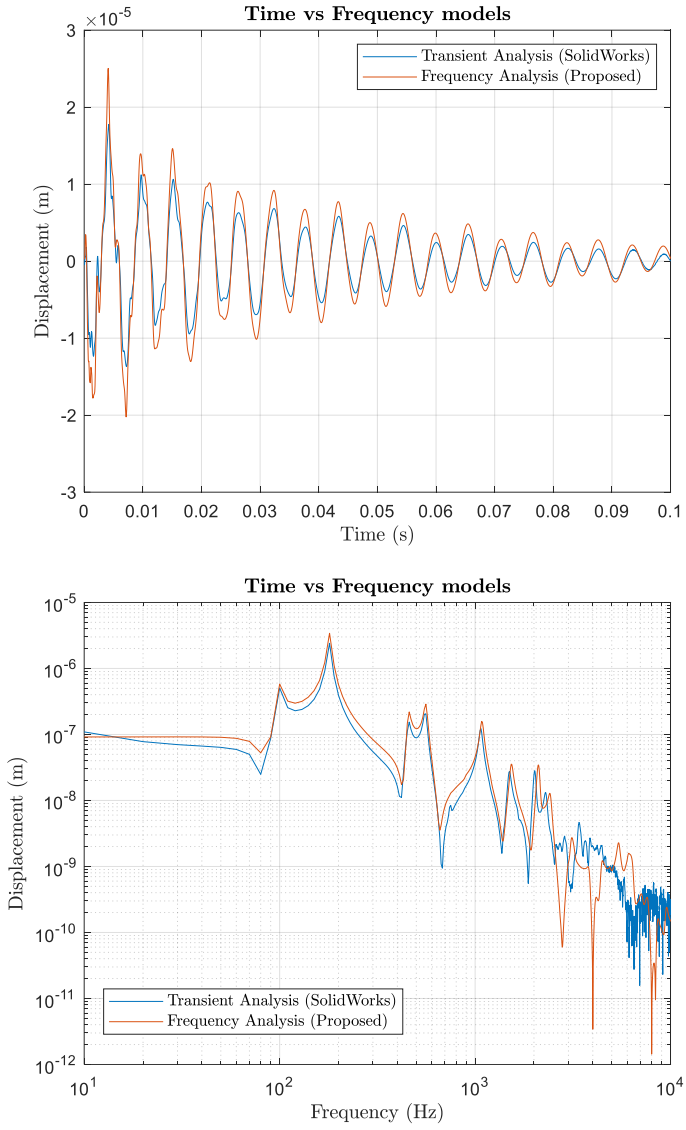

Figure 31. Comparison of the results obtained with the time model (Transient Analysis in SolidWorks 2022) and the proposed frequency model (which exploits the FEM solver integrated into MATLAB 2021b). Above, the comparison of the time signals; below, the related frequency responses.

Table 6. Running times necessary to solve the FEM analysis in the time (Transient Analysis in SolidWorks 2022) and frequency domain (MATLAB 2021b) and related performance improvement generated by the proposed method.

	SolidWorks 2022	**MATLAB 2021b**	$\Delta t_{\%}$
Running time	≈ 890 s	≈ 100 s	790%

Furthermore, the developed model offers a substantial reduction in computational time, leading to an overall decrease in simulation costs. This reduction in downtime is particularly advantageous for the tuning of the plate to execute shock qualification tests efficiently. Specifically, the transient analysis obtained using the FEM commercial software took nearly 9 times longer than the proposed frequency model, as illustrated in Table 6. Unlike the time model, which necessitates the analysis of the entire plate behavior at each time step, the frequency model enables the calculation of the response at a single point of interest. This results in a significant reduction in dimensionality and computational complexity.

The result of a second test is proposed in Figure 32 to validate the model under different operating parameters. This configuration includes differences in impact and measurement locations, impact velocity, hammerhead add-on mass, and the presence of a specimen. Additionally, a non-symmetric raised cosine force profile (a modified Hann window) is adopted to better approximate real-world scenarios. Despite these variations, the simulated curve closely follows the experimental one, demonstrating the accuracy of the model. Similar to Test #1, limitations depending on the assumptions are evident, particularly at low and high frequencies. Inaccuracies at low frequencies may be attributed to approximations in the damping coefficient and nonlinearities resulting from boundary conditions. Conversely, deviations at high frequencies may be due to the pulse duration estimation and the properties of the impacting bodies.

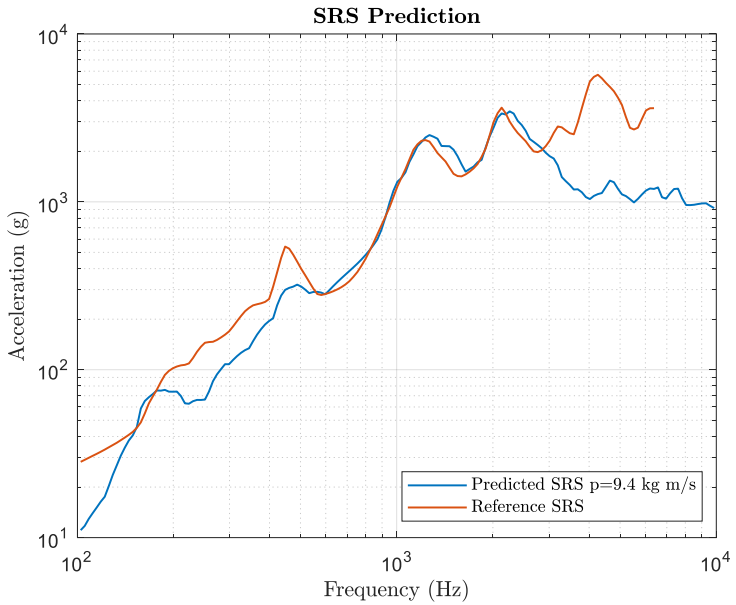

Figure 32. Comparison of the SRS simulated by the proposed model (in blue) with the experimental one (in red) obtained in [58]. The model parameters were set as reported in the Test #2 column of Table 5.

Furthermore, a comparison between the simulated pulse and a real force profile obtained from an impact characterization is presented. To analyze the influence of the force profile in greater detail, Figure 33 illustrates the results in terms of SRS obtained with four different impulses under Test #2 conditions. Specifically, Figure 33 shows the four different adopted functions: (1) the rectangular, (2) the half-sine, (3) Hann window and (4) a real pulse. All curves are normalized to have equal duration τ and unitary momentum to prevent confounding factors. The real profile was experimentally acquired using a test bench for impacts characterization, replicating the experimental conditions as accurately as possible. The impact was generated using the PCB 086C03 impact hammer (shown in Figure 34) equipped with a hammerhead with an established constant curvature, hitting a pendulum with a flat contact surface. The results indicate that the non-symmetric raised cosine (modified Hann window) is the force profile that best approximates the real case, with the SRS obtained from this function closely reproducing the reference curve. Additionally, Figure 33 demonstrates that the force profile effect predominantly influences the high frequencies, acting as a low-pass filter with variable cutoff frequency and slope (i.e., filter order).

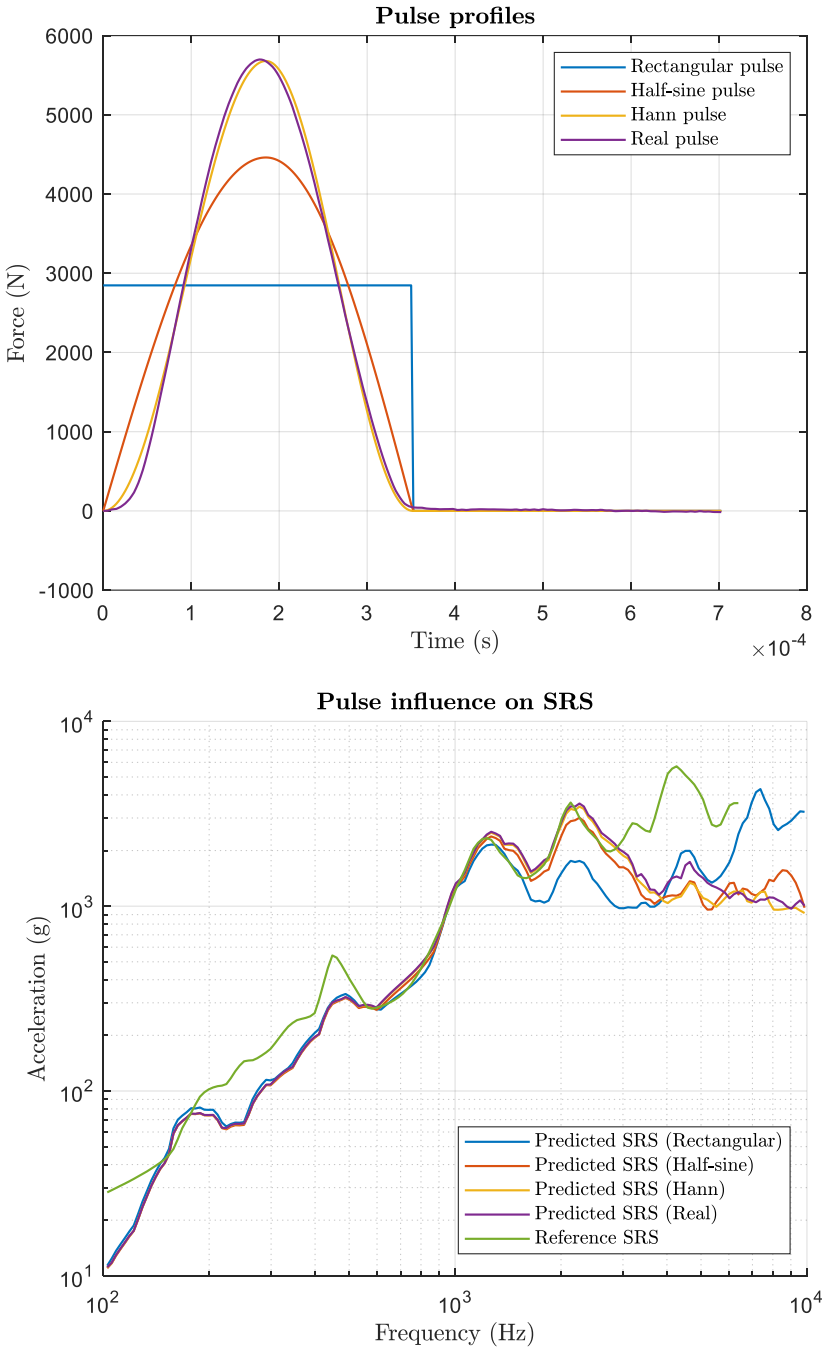

Figure 33. Above, force profiles in the proposed model. Below, comparison of the predicted SRS as the assumed pulse functions vary.

Figure 34. Impact hammer adopted to characterize the force profile.

To sum up, this chapter described numerical models developed for the simulation of pyroshock tests with resonant plates. The comprehensive parametric model introduced offers a novel approach to accurately simulate the SRS acceleration of the plate with minimal computational burden, achieved through a development in the frequency domain. Its short computation times and adaptability make it suitable for various applications, particularly in tuning test facilities to meet specific test requirements. This capability translates to significant reductions in downtime and costs associated with setting up experimental systems. Notably, these improvements address the iterative nature of many existing pyroshock simulation techniques, considerably simplifying the process. The comprehensive parametric model underwent validation across different experimental setups and was compared against time-frequency models, together with the pulse characterization. These detailed analyses have been employed to validate the proposed model and highlight its advantages, including its flexibility and computational efficiency.

Chapter 6

Inverse Problem: Design Optimization

After describing the numerical simulation models of pyroshock tests, this chapter proposes some methods for solving the inverse problems. It is worth noting that direct problem refers to the fine-tuning of the experimental setup thanks to the calculation of the required momentum p, while the inverse problem focuses on the optimal design of the test facility itself. The optimal design refines several parameters, such as the geometry and the material of the resonant plate. The reference model adopted for all the reported optimization techniques is the comprehensive parametric model described in Subsection 5.2. The three macro-categories, composing the present model and analyzed in Figure 23, are further expanded with an optimization algorithm to effectively solve the problem of designing a shock test facility, as shown in Figure 35. These results - which would not be achievable with the existing techniques - are thus obtained in a straightforward, novel, and innovative way. Initially, a generic optimization process using GA [105] is proposed. Subsequently, more specific investigations are described.

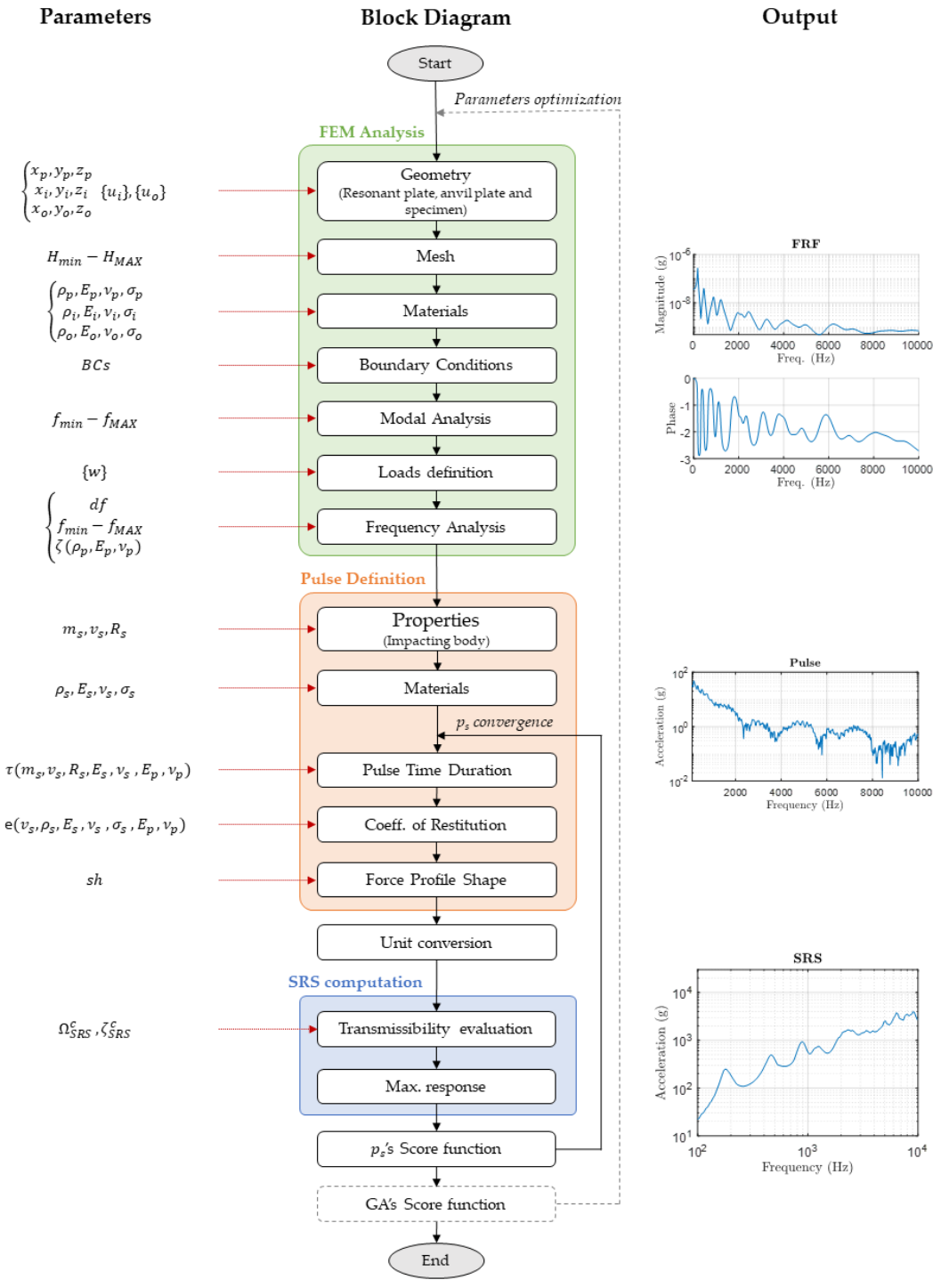

Figure 35. Block diagram describing the model for the simulation of pyroshock tests, implemented for the design of the experimental setup. The involved parameters and the graphs showing the results of each macro-phase are highlighted. The dotted lines represent the implementation characteristic of the design phase.

6.1 Genetic Algorithm Optimization

The proposed comprehensive parametric method simulates the SRS of the entire system starting from the definition of the experimental setup. The model can thus be used to simulate the plate behavior and, consequently, to tune the different parameters as the test requirements vary, constituting the direct problem. Moreover, the model can be further exploited to address the inverse problem, namely, the design of the experimental setup or its components given specific requirements and conditions. The distinction between these two problems basically lies in the typology of unknown parameters, such as the momentum p_s rather than geometric parameters of the plate x_p, y_p, z_p.

To achieve an optimized system design, the simulation model serves as the score function of a heuristic optimization framework such as GA. Hence, the score functions outlined in Eq. (30)-(33) could be the reference cost used by GA to derive the unknown parameters. Specifically, in this application, the score functions are customized to evaluate the error only when the SRS falls outside the tolerance region. Consequently, any value within this range is evaluated as zero error, while those exceeding these limits contribute to the error in proportion to their deviation from the tolerances. This modification of the score function is delineated in Eq. (34).

$$score_{GA} = \begin{cases} 0 & if \quad \ddot{X}_r(\Omega_c) - \ddot{X}_{tol}^- < \ddot{X}_{SRS}(\Omega_c) < \ddot{X}_r(\Omega_c) + \ddot{X}_{tol}^+ \\ score & if \quad \ddot{x}_{SRS}(\Omega_c) \leq \ddot{X}_r(\Omega_c) - \ddot{X}_{tol}^- \vee \ddot{X}_{SRS}(\Omega_c) \geq \ddot{X}_r(\Omega_c) + \ddot{X}_{tol}^+ \end{cases} \tag{34}$$

where $\ddot{X}_{tol}^-$ and $\ddot{X}_{tol}^+$ are respectively the values of the lower and upper tolerances, $score$ is a generic cost function, such as the cost functions described in Eq. (30)-(33), and $score_{GA}$ is the modified cost function for the application of the optimizer. Indeed, prioritizing the inclusion of the SRS within the tolerances during the design process is of prime importance, rather than solely focusing on minimizing the error according to the required curve.

This simulation algorithm facilitates the derivation of the design parameters of the test facility by employing a GA optimizer and specifying the required SRS profile along with related tolerances. Since SRS requirements are highly variable and depend on many factors, such as the launcher typology and the equipment location, a typical SRS profile is adopted as defined by the guidelines outlined in the NASA-STD-7003A standard [8]. However, the three-point SRS selected as reference,

along with its tolerance range, proves to be consistent with previous studies such as those conducted by Sandia National Laboratories [10]. Figure 36 illustrates a potential outcome achieved through this optimizer. All parameters except for the plate dimensions (e.g., the material of the resonant plate, mass and speed of the impacting object) are assumed to be average conditions for the pyroshock tests to be conducted with the plate under design. The GA optimizer iterates to minimize the score function, representing the deviation of the simulated SRS from the desired tolerances, within predefined maximum and minimum values for each parameter. Table 7 presents the optimal dimensions of the resonant plate obtained through GA optimization, resulting in an SRS response that satisfactorily meets test requirements and tolerances. The reported result was obtained by setting GA with a population size of 15 and the number of iterations equal to 10. The lower and upper bounds were set to optimize the resonant plate in a dimensions range. The minimum and maximum sizes were respectively established as equal to $0.2 \times 0.2 \times 0.02$ m^3 and $2 \times 2 \times 0.05$ m^3. Additionally, this model enables the determination of the required momentum, given the optimal test facility obtained under the specified design conditions.

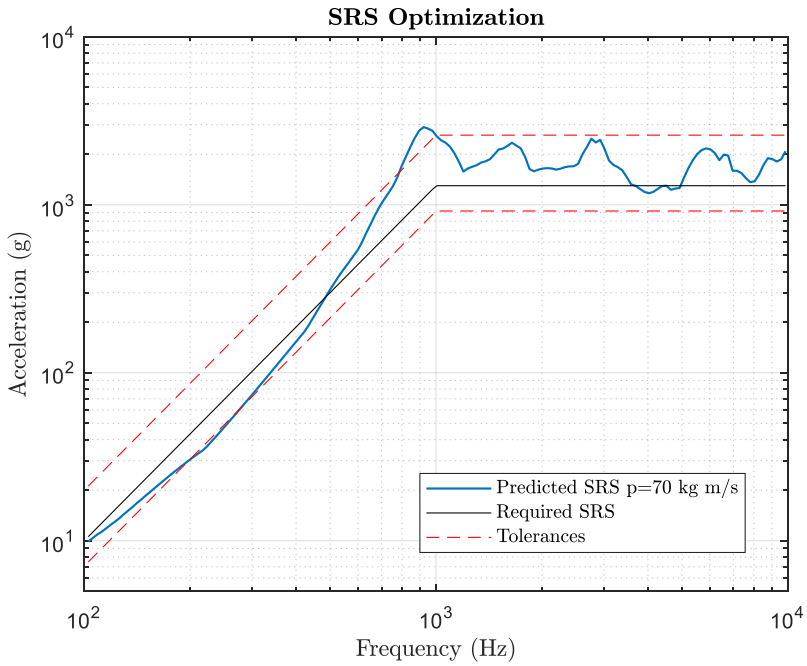

Figure 36. Comparison of the GA-optimized SRS (in blue) with the reference curves representing the typical requirements and related tolerances of pyroshock tests. The simulated behavior falls quite faithfully within the tolerances, minimizing the error and additionally allowing the estimation of the necessary momentum.

Table 7. Inverse problem results in terms of resonant plate dimensions optimized by means of GA.

Plate Dimension	Optimized Result
Length (x)	500 mm
Width (y)	400 mm
Thickness (z)	40 mm

The SRS obtained using the optimized plate indicates a slight overtesting, a condition judged more acceptable than undertesting in qualification tests. To draw further considerations on the optimized result, it is worth noting the complexity level to obtain a real experimental SRS within the required tolerances. Figure 37 shows an experimental SRS acquired in a real industrial context, with the amplitude normalized with respect to the required knee-frequency acceleration. This representation elucidates the disparities between the behavior of the real system and the specified requirements. Tuning the resonant plate often entails compromises about qualification test requirements, such as accepting overtesting or undertesting. This perspective highlights the important role of a simulation model in the calibration and realization of a test facility for pyroshock qualification tests.

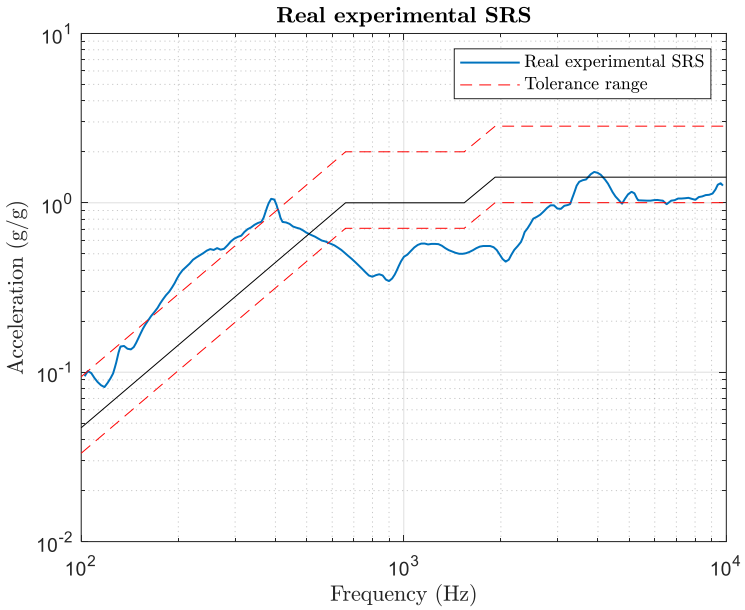

Figure 37. Experimental SRS used in a real industrial context, normalized with respect to the required knee-frequency acceleration.

6.2 Shape and Size Optimization

This section exploits the reference numerical model to simulate a pyroshock test and optimize the test facility configuration. A heuristic optimization algorithm is introduced to optimize the shape and size of a resonant plate to match the required SRS. The digital twin adopted in this process evaluates the efficiency of both regular polygonal and irregular quadrilateral shapes and sizes. The development of the proposed model in the frequency domain offers notable advantages, including the reduction of calculation times. Optimizing pyroshock test facilities is promising for enhancing both the accuracy of SRS outcomes and the efficiency, in terms of time and cost associated with test facility tuning.

6.2.1 Regular Polygonal Geometry Optimization

Initially, the emphasis is on geometric parameters, using a reverse engineering approach. Specifically, the investigation deeply analyzes the optimal shape of a resonant plate to satisfy standardized requirements: firstly regular and subsequently irregular, along with their respective dimensions, plates are tested. In the direct problem, these geometric parameters are typically fixed, given that the plate geometry usually remains constant, and the primary objective of the simulation is the determination of the necessary momentum to satisfy the shock test criteria.

Most test facilities for shock tests in the literature use a square or rectangular resonant plate. For instance, [58] and [38] use square aluminum alloy plates with dimensions of $1 \times 1 \times 0.03$ m^3 and $1 \times 1 \times 0.05$ m^3, respectively. Instead, [46] analyzes a rectangular plate with dimensions of $1.2 \times 0.5 \times 0.03$ m^3.

A genetic algorithm is used to search for the optimal plate. The integration of an embedded CAD modeler and a FE solver enables the accurate prediction of the dynamic behavior of a resonant plate with complex and variable shapes.

The model is configured with three key parameters defining the plate geometry: the circumscribed radius r_p for regular plate geometries, the number of sides n_p for polygonal configurations, and the plate thickness z_p. These parameters enable the exploration of the dynamic characteristics of plates with varying shapes and sizes. Moreover, the mass m_s and velocity u_s of the impacting object are also optimized, considering that the mass of the plate is proportional to its size. Consequently, larger plates necessitate higher momentum, and vice versa. This approach improves the optimization of the SRS profile, making it independent of other potential

confounding factors. To mitigate the risk of encountering local minima, typical of heuristic optimizers, all parameters are discretized within specific ranges.

The formulation of a score function is fundamental to deal with the minimization task effectively. While conventional metrics like RMSE and MAE are widely employed, a specific score function is conceived for the present application. Given that pyroshock requirements are typically provided with associated tolerances, the score function is designed to evaluate errors only when the SRS falls outside the tolerance regions. This adjustment has been integrated into the score function presented in Eq. (34). Nevertheless, modifications based on the particular application or further ameliorations of this metric are evaluable. Specifically, the score function should reflect the higher level of criticality for undertesting over overtesting conditions. Hence, the revised score function adopted from now on is defined as follows:

$$score_{GA} = \begin{cases} \dfrac{\log_{10}(\ddot{X}_{SRS}) - \log_{10}(\ddot{X}_r)}{\log_{10}(\ddot{X}_{tol}^{+}) - \log_{10}(\ddot{X}_r)} - 1 & if \quad \ddot{X}_{SRS} > \ddot{X}_{tol}^{+} \\ 0 & if \quad \ddot{X}_{tol}^{-} \le \ddot{X}_{SRS} \le \ddot{X}_{tol}^{+} \\ \dfrac{\log_{10}(\ddot{X}_{SRS}) - \log_{10}(\ddot{X}_r)}{\log_{10}(\ddot{X}_{tol}^{-}) - \log_{10}(\ddot{X}_r)} - 1 & if \quad \ddot{X}_{SRS} < \ddot{X}_{tol}^{-} \end{cases} \quad (35)$$

where $\ddot{X}_{SRS}(\Omega_c)$ is the calculated value of the acceleration synchronized to the resonant frequency Ω_c of the c-th SDOF system for the SRS calculation, $\ddot{X}_r(\Omega_c)$ is the test requirement (or the generic reference curve) in terms of SRS acceleration, $\ddot{X}_{tol}^{-}$ and $\ddot{X}_{tol}^{+}$ are respectively the values of the lower and upper tolerances. For the sake of clarity, Figure 38 shows the colormap representing the score applied to the SRS predictions, considering a standard requirement.

The minimization of the cost function in a discrete multidimensional space led to the outcomes in terms of regular shape and size optimization of the resonant plate. This multivariate space is generated by the five parameters, identified as crucial for the present investigation and summarized in Table 8. The upper and lower bounds were established based on typical applications, ensuring consistency between parameters. Similarly, discretization was determined considering the best trade-off between the total number of combinations and the computational burden. The number of sides n_p of the polygon has been set to consider all the regular shapes

from $n_p = 3$ (triangular case) up to $n_p = 8$ (octagonal case) and, in addition, $n_p = 100$ to simulate a circular plate.

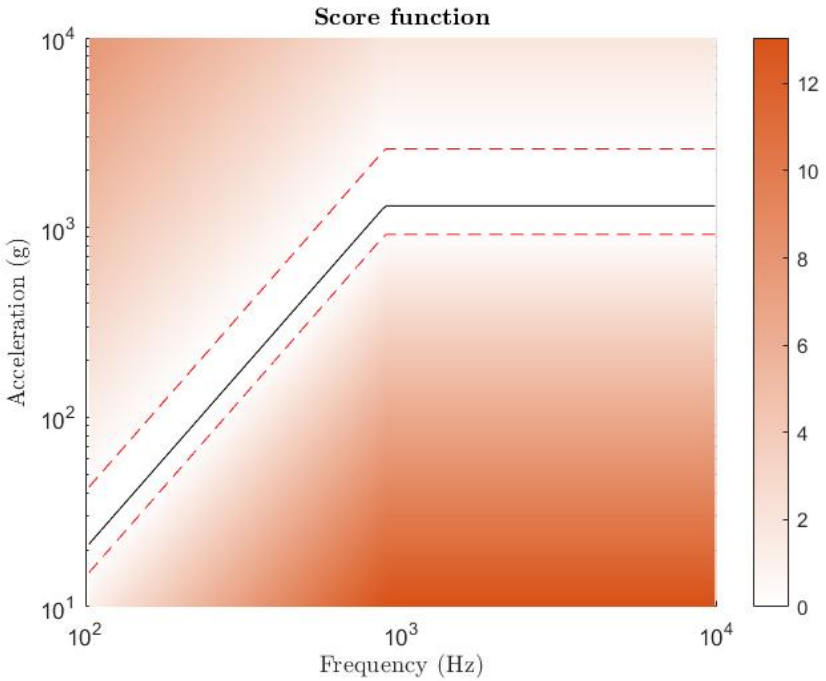

Figure 38: Colormap describing the adopted score function according to a generic requirement with related tolerances.

Table 8. Discretization of the parameters optimized by GA for the regular polygonal case.

Parameter	Lower Bound	Discretization	Upper Bound
r_p	0.45 m	0.05 m	0.60 m
z_p	0.02 m	0.01 m	0.05 m
n_p	3 sides	1 side	8 sides + circle
m_s	1 kg	1 kg	10 kg
u_s	1 m/s	1 m/s	10 m/s

With a total of 11200 possible combinations, a population size of 50 was chosen to initialize the genetic algorithm, considered the best trade-off between the density

of analyzed cases in the multidimensional space and calculation times. Additionally, to ensure algorithm convergence while minimizing runtime, the number of iterations was set to 10.

Considering the specific requirements used in this analysis, GA found the best configuration as a triangular plate ($n_p = 3$) inscribed in a circle with radius $r_p = 0.6$ m and thickness $z_p = 0.04$ m, hit by an impacting object with mass $m_s = 9$ kg and velocity $u_s = 1$ m/s. Table 9 reports both the assumed and the optimized parameters established to define the design decisions in the model. Figure 39 shows the optimized plate geometry with arrows indicating the input and output directions fixed in the model.

Table 9. Fixed and optimized (indicated by the superscript *) parameters adopted to numerically simulate the configuration with the optimized regular shape.

Parameter	Value
$\boldsymbol{r_p}$*	0.60 m
$\boldsymbol{z_p}$*	0.04 m
$\boldsymbol{n_p}$*	3 sides
$\boldsymbol{m_s}$*	9 kg
$\boldsymbol{u_s}$*	1 m/s
Plate material	Al6082
Impact location	Center of mass (0 m; 0 m)
Measurement location	Center of mass (0 m; 0 m)
Boundary conditions	Free
Impacting object material	SS303
Impacting object curvature	0.2 m
Force profile shape	von Hann window

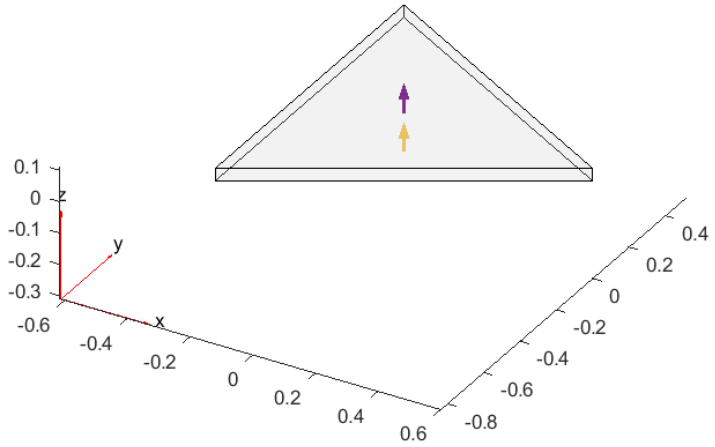

Figure 39. Optimized geometry of the regular polygon resonant plate.

Figure 40 shows the SRS prediction of the optimized resonant plate in the described operating conditions. The optimized design led to satisfactory results since the required tolerances are almost totally accomplished.

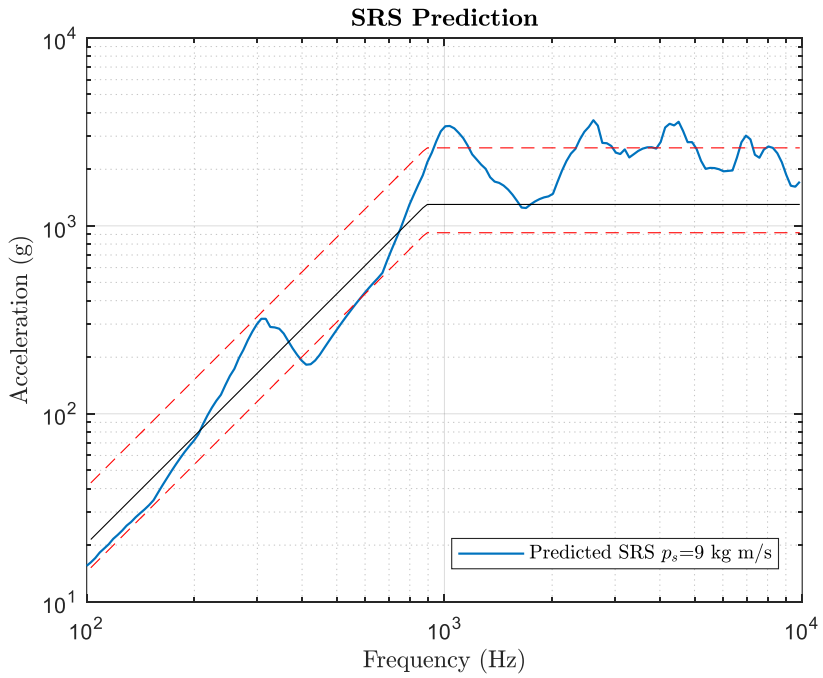

Figure 40. Simulated SRS inherent to the GA-optimized resonant plate with regular triangular shape.

6.2.2 Irregular Quadrilateral Geometry Optimization

The previous optimization focused on exploring various geometries with the constraint of regular polygonal shapes. To further expand the analysis and potentially identify shapes that better fulfill the requirements, a second method was developed. This method extends the investigation to include irregular shapes. Due to the vast number of possible irregular shapes, the analysis is restricted to irregular quadrilateral shapes. These geometries generate a notable range of configurations while also limiting the overall population and the parameters to be optimized.

The proposed simulation model offers flexibility in defining irregular quadrilateral plates by specifying the coordinates $(x_V; y_V)$ of their vertices $V = 1,2,3,4$, as shown in Figure 41. To prevent redundancies arising from geometric symmetries, one vertex (V_1) is fixed at the origin of the reference system. The remaining vertices are confined to predefined regions of space, which also determine the maximum and minimum dimensions of the plate ($1 \times 2 \times 0.05$ m^3 and $0.5 \times 1 \times 0.01$ m^3 respectively). Moreover, this definition of regions allows to consider irregular triangular shapes, corresponding to degenerate quadrilateral cases. Table 10 presents the parameters optimized by GA and their established discretization. In addition to the coordinates of the vertices, GA also optimizes the thickness z_p of the plate, the mass m_s, and the velocity u_s of the impacting object, driven by the same considerations as in the case of regular shapes.

Table 10. Discretization of the parameters optimized by GA for the irregular quadrilateral case.

Parameter	Lower Bound	Discretization	Upper Bound
x_2	0 m	0.1 m	0.5 m
y_2	1 m	0.1 m	2 m
x_3	0.5 m	0.1 m	1 m
y_3	1 m	0.1 m	2 m
x_4	0.5 m	0.1 m	1 m
y_4	0 m	0.1 m	1 m
z_p	0.01 m	0.01 m	0.05 m
m_s	1 kg	2 kg	9 kg
u_s	1 m/s	2 m/s	9 m/s

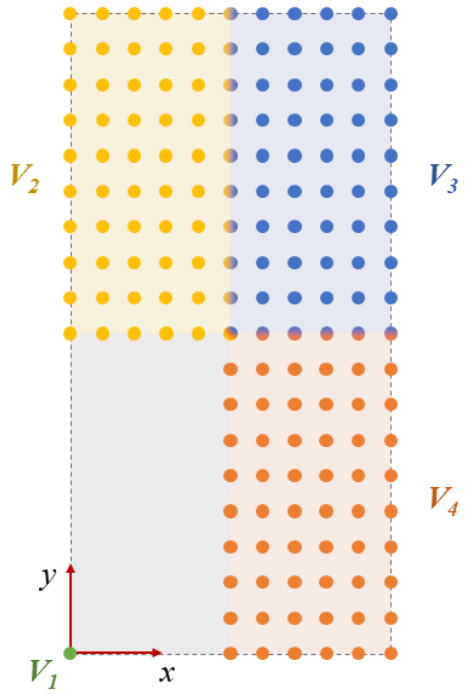

Figure 41: Discretization grid of the parameters for the optimization of the irregular geometry of the resonant plate.

The other parameters were set as in the previous optimization, including the plate material (in the specific case, an aluminum alloy), the impact and measurement points (both established in the center of gravity of the plate). Since the multivariate space generated by the parameters to be optimized contains a higher number of possible combinations, the GA optimizer settings were consequently modified by increasing the size of the population up to 200, while maintaining the number of iterations equal to 10. The score function that regulates the optimization is reported in Eq. (35) and shown in Figure 38.

The resulting geometry of the GA-optimized irregular quadrilateral plate is shown in Figure 42, while Table 11 lists both the optimized and assumed parameters adopted in the simulation. It can be observed that the resulting shape is rather complex and difficult to extract using other methodologies. It is worth noting that

the specific imposed conditions, such as the required SRS profile, may influence the result and lead to this precise geometry.

Table 11. Parameters adopted to simulate the configuration with the optimized irregular shape. Optimized parameters are indicated by the superscript *.

Parameter	Value
$\boldsymbol{V_1}$	(0 m; 0 m)
$\boldsymbol{V_2}$*	(0.3 m; 1.6 m)
$\boldsymbol{V_3}$*	(0.8 m; 1.5 m)
$\boldsymbol{V_4}$*	(0.8 m; 1 m)
$\boldsymbol{z_p}$*	0.03 m
$\boldsymbol{m_s}$*	9 kg
$\boldsymbol{u_s}$*	1 m/s
Plate material	Al6082
Impact location	Center of mass (0.475 m; 1.025 m)
Measurement location	Center of mass (0.475 m; 1.025 m)
Boundary conditions	Free
Impacting object material	SS303
Impacting object curvature	0.2 m
Force profile shape	von Hann window

Figure 43 shows the simulated SRS with the new optimized plate. It is worth noting that the curve falls perfectly within the tolerance ranges, flawlessly satisfying the imposed requirements. It cannot be excluded that other equivalent solutions exist within the population of considered plates (i.e., plates with irregular quadrilateral geometry and dimensions within the set range).

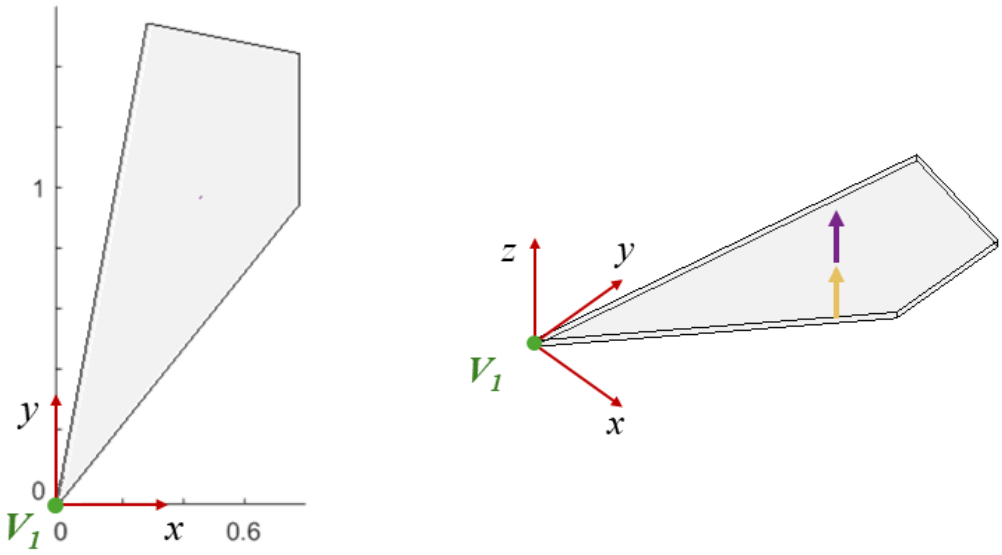

Figure 42. Resulting optimization of the irregular quadrilateral shaped and sized resonant plate.

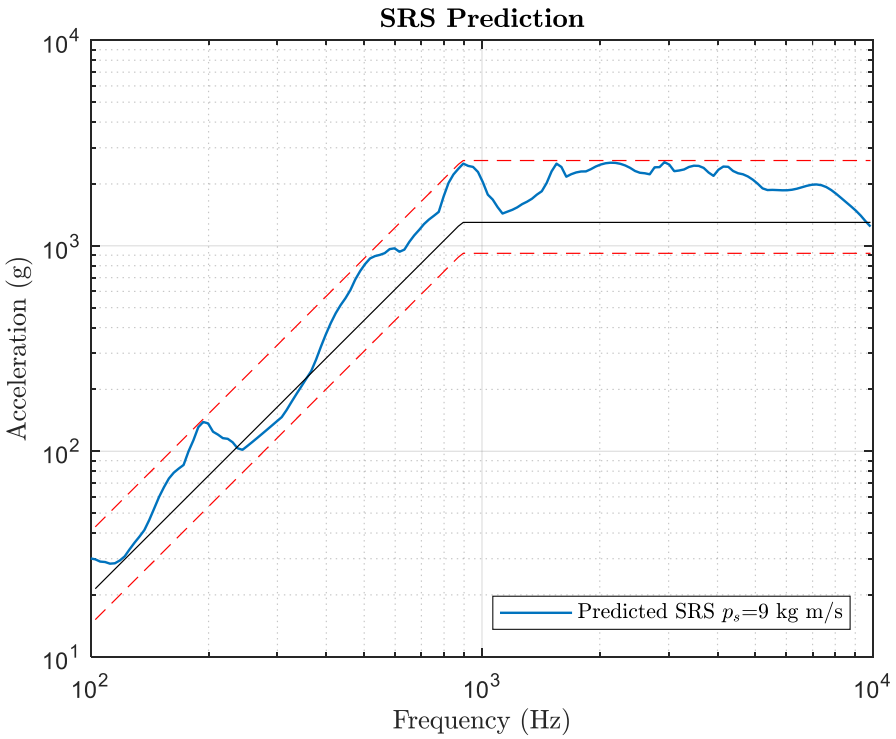

Figure 43. Simulated SRS inherent to the GA-optimized resonant plate with the trapezoidal scalene shape.

6.3 Optimization of the Energy Input and Output Parameters

This section focuses on investigating the effect of energy input and output parameters within a test facility, including factors like impact location, anvil material, and object mounting position. These parameters have significant influence, and their interactions are complex, making a comprehensive exploration necessary. Such an exploration can notably reduce calibration times and offer economic benefits by circumventing costly trial-and-error iterations. This optimization exploits the simulation methodology aiming at optimizing test configurations. An exemplary application is demonstrated based on the outcomes derived from the optimization of regular shape and size. Furthermore, given that the test object influences the dynamics of the entire system, the appropriate setting of these variables allows the correction and compensation of the effects of the specimen on the SRS.

While the previous geometry optimizations aimed to tune the resonant plate according to specific requirements, this optimization focuses on better matching the SRS requirement by adjusting the so-called energy input and output parameters. In this context, the energetic parameters are defined as: (1) the impact pad (or anvil) material, (2) the impact location, and (3) the testing object mounting location (i.e., the measurement location) in proximity to their design values. This optimization is applicable to any plate typology and geometry. The following results concern the optimized plate with regular geometry, since it is still possible to compensate for the residual error. It is worth noting that the geometrically optimized plates were automatically designed by GA without neither anvil nor testing object, whose influences were neglected. Furthermore, the excitation and the measurement point were considered coincident to the center of the plate. To simulate a real impulse, the impact force $f(t)$ is modelled by two half non-symmetrical windows (left and right) whose shape is defined as half a raised cosine (i.e., the von Hann window). The described optimization of the input and output parameters has been investigated to cope with the effects of variable operating conditions.

To investigate the effects of variable anvil material and input pulse location on the contact time computation, the numerical model was implemented including a fixed-size ($0.07 \times 0.07 \times 0.01$ m3) anvil with variable material. Furthermore, a NASA CubeSat 1U was chosen as the sample testing object, characterized by an equivalent density of ρ_{eq} and a characteristic dimension of 0.1 m [106]. The input pulse location and the mounting location coordinates of the space equipment were

varied over a discrete range around the plate center (±0.1 m), as shown in Figure 44. This approach simulated various scenarios for mounting the CubeSat and the anvil plate on the resonant plate. Hence, a total of 162 combinations consisting of 9 input positions, 9 output positions, and 2 anvil plate materials were analyzed. It is worth noting that some of these combinations may be redundant because of possible symmetries of the test facility. However, for the sake of proposing a generic method applicable across various scenarios, all potential configurations were thoroughly examined in this study.

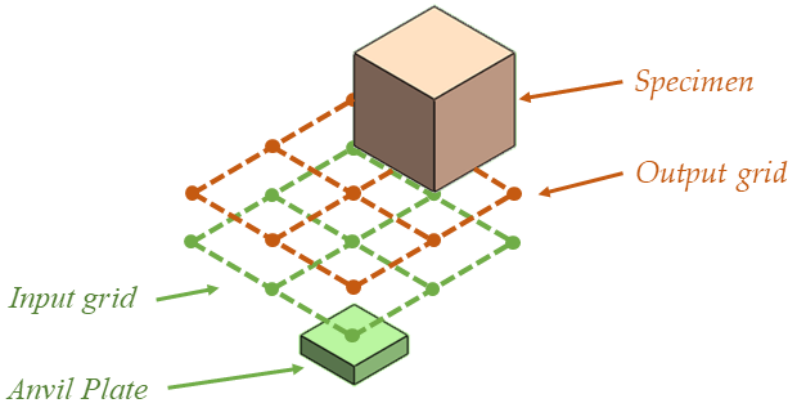

Figure 44: Scheme of the input/output grid including 9 different positions for the anvil plate (green) and the specimen (orange), respectively.

The starting point for energy input and output optimization is the optimized resonant plate depicted in Figure 39. This plate is an equilateral triangle with side dimensions of 1.04 m (inscribed in a circumference of 0.6 m) and a thickness of 0.04 m, composed of aluminum alloy. For clarity and completeness, Figure 45 illustrates the FE modal analysis of the bare triangular plate.

The SRS depicted in Figure 40 exhibits its first peak corresponding to the natural frequency of mode #1 and its second peak coincides with mode #7. This alignment is evident from Figure 45, where modes #1 and #7 manifest significant displacements at the center of gravity, which corresponds with the established excitation and measurement points from the regular shape optimization.

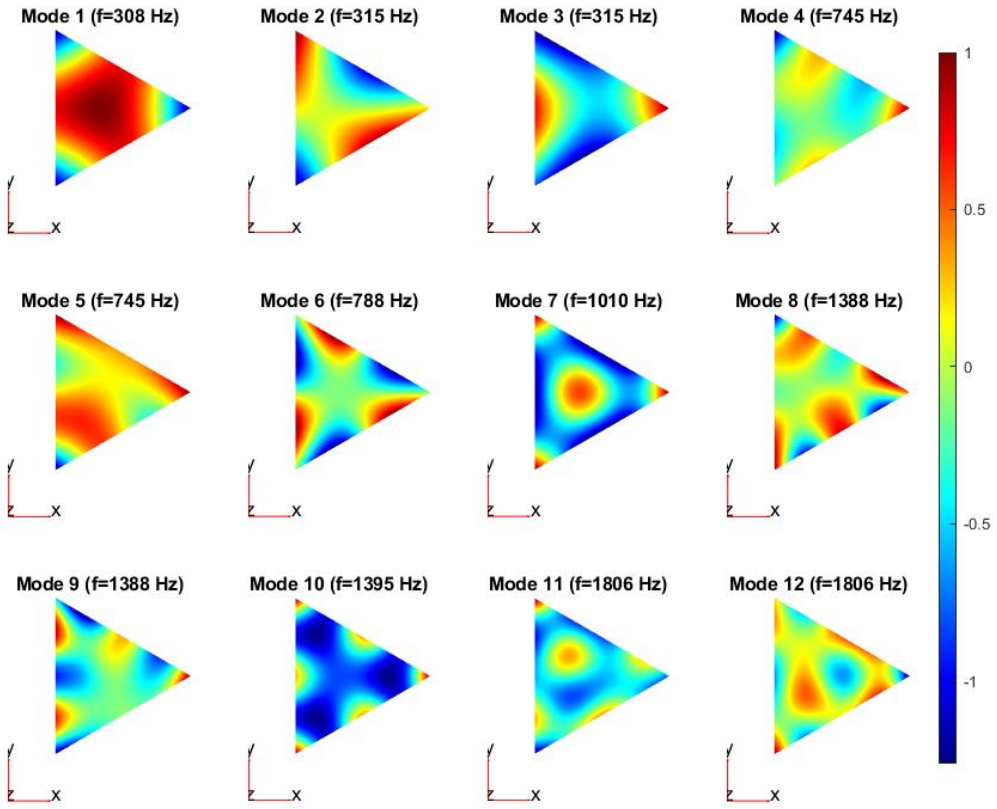

Figure 45: Modal analysis of the bare regular triangular plate.

To analyze the impact of input and output parameters, a brute force approach is employed, considering the full factorial combinations. Figure 46 illustrates the input/output grids applied to the regular triangular plate following the GA optimization. Consequently, numerical simulations of the SRS are conducted for each of the 162 combinations, evaluating the optimal tuning parameters under new operating conditions. This assessment exploits the score function defined in Eq. (35) and depicted in Figure 38, which considers tolerance regions and penalizes undertesting more severely than overtesting conditions. Table 12 provides a summary of the pertinent parameters and their corresponding values.

Table 12. Description of parameters defined in the model to optimize energy input and output.

Parameter Name	Parameter Value / Range	Parameter Description
$\{\boldsymbol{u_i}\}, \{\boldsymbol{u_0}\}$	Points 1-9 (Figure 44)	Impact and object location coordinates
$\boldsymbol{\rho_i}$	2700 or 7870 kg/m^3	Density of the anvil material
$\boldsymbol{E_i}$	69 or 205 GPa	Young's modulus of the anvil material
$\boldsymbol{\nu_i}$	0.33 or 0.29	Poisson's ratio of the anvil material
$\boldsymbol{\sigma_i}$	80 or 350 MPa	Yield stress of the anvil material
$\boldsymbol{\rho_0}$	2000 kg/m^3	Equivalent object density
$\boldsymbol{l_0}$	0.1 m	Object characteristic dimension (side of the cube)
$\boldsymbol{r_p}$	0.6 m	Radius of the circumscribed circle
$\boldsymbol{n_p}$	3	Number of sides of the polygon
$\boldsymbol{z_p}$	0.04 m	Thickness of the plate
$\boldsymbol{H_{min} - H_{max}}$	0.0186 - 0.0373 m	Mesh size - range
$\boldsymbol{\rho_p}$	2700 kg/m^3	Density of the plate material
$\boldsymbol{E_p}$	69 GPa	Young's modulus of the plate material
$\boldsymbol{\nu_p}$	0.33	Poisson's ratio of the plate material
$\boldsymbol{BCs}$	Free	Type of Boundary conditions
$\boldsymbol{f_{min} - f_{max}}$	100-10000 Hz	Range of frequency for the study
$\{\boldsymbol{w}\}$	[0,0,1] (orthogonal)	Input Force intensity and direction
$\boldsymbol{df}$	10 Hz	Frequency resolution for the Inertance
$\boldsymbol{\zeta_p}$	0.02	Modal damping factor of the plate
$\boldsymbol{m_s}$	9 kg	Bullet mass
$\boldsymbol{u_s}$	1 m/s	Bullet speed
$\boldsymbol{R_s}$	0.2 m	Bullet contact radius
$\boldsymbol{\rho_s}$	7870 kg/m^3	Density of the plate material
$\boldsymbol{E_s}$	205 GPa	Young's modulus of the bullet
$\boldsymbol{\nu_s}$	0.29	Poisson's ratio of the bullet
$\boldsymbol{sh}$	Raised-cosine (von Hann window)	Window shape

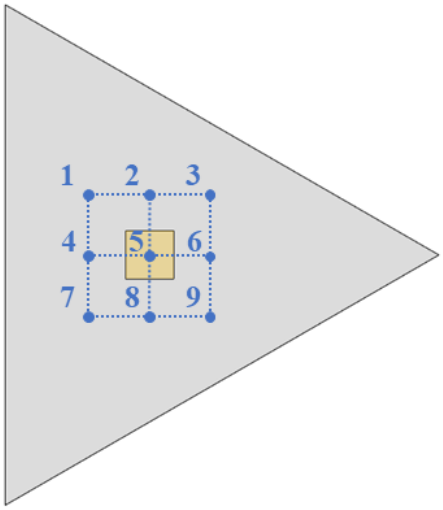

Figure 46: Scheme of the optimized resonant plate (grey), specimen (yellow), and the blue grid with the 9 different positions of input and output under analysis.

The scores corresponding to each of the 162 conditions are shown in Figure 47. It is worth noting that the steel anvil plate demonstrates superior performance compared to its aluminum counterpart. This discrepancy arises due to the restitution coefficient (e) and the pulse duration (τ), both dependent on the mechanical properties of the impacting bodies, thereby influencing contact mechanics. Setting #41, which denotes the operating conditions utilized for optimizing the bare plate design, remains optimal among the aluminum anvil plates. The equivalent scenario with the steel anvil plate corresponds to setting #122. Ultimately, the overall optimal case is denoted by #131, characterized by input coordinates at (0 m; 0 m) and the specimen positioned at point 6 (0.1 m; 0 m).

Figure 48 illustrates the comparison of the predicted SRS in the operating conditions #41, #122, and #131, which are considered the three most relevant cases. The best condition #131 leads to faithfully satisfy the requirements. Furthermore, the peak around 308 Hz (visible in Figure 45 and referred to the bare plate SRS simulation) is missing due to the implementation of the anvil plate and the testing object.

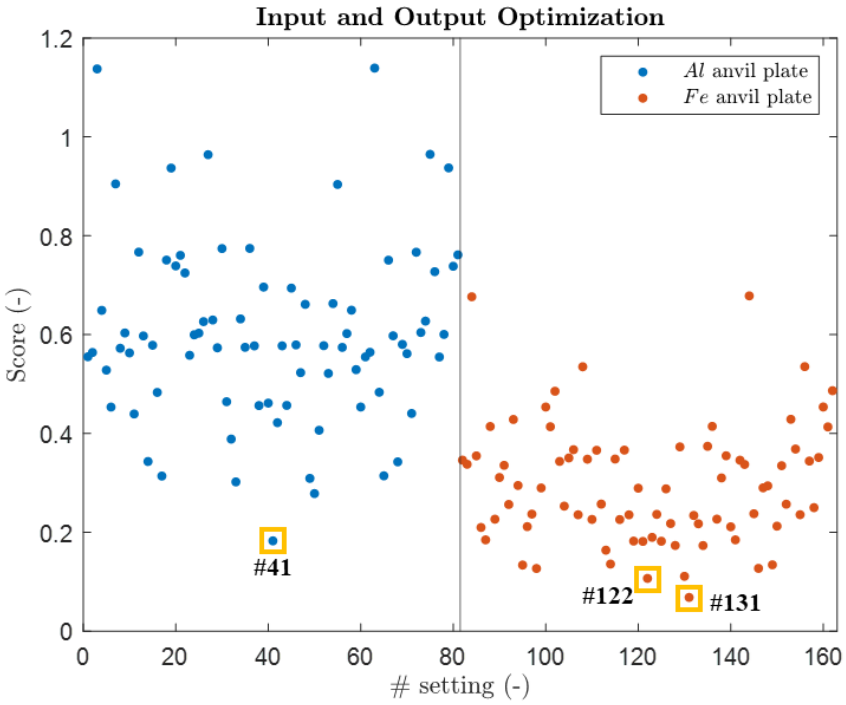

Figure 47: Scores computed for each of the 162 analyzed setting conditions.

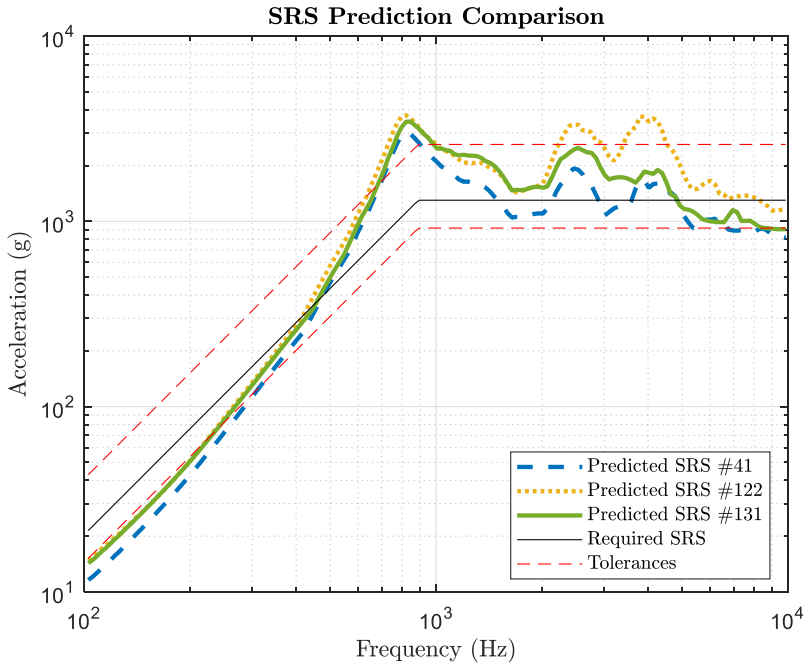

Figure 48: Comparison of the predicted SRS obtained with settings #41, #122, and #131, identified as the most relevant.

In conclusion, this chapter deepened various optimization strategies for improving the performances of a pyroshock test facility, dealing with both general, geometrical, and energetic considerations. The use of a robust numerical model equipped with an embedded CAD modeler and FE solver enabled comprehensive simulations of pyroshock tests. The model adaptability and precision facilitated a GA-based optimization of resonant plate shape and size to align with specified SRS requirements.

Initially, a wide-range optimization process was outlined, followed by a detailed exploration of specific optimization facets. One of these optimizations focused on regular geometries, obtaining solutions that effectively satisfy tolerance requirements. Another investigation concerned irregular quadrilateral shapes, resulting in a resonant plate design that further optimized SRS outcomes by fully respecting tolerance ranges. The final optimization strategy pertained to energy input and output parameters, diverging from previous reverse engineering approaches. This method focused attention on the dynamic nature of operating conditions, incorporating elements like the anvil plate and specimen. The results demonstrated the possibility of achieving configurations better aligned with requirements through energetic parameter optimization.

Given the intricate nature of pyroshock test facilities and the significant influence of their parameters on SRS, the findings exhibited improvements in SRS accuracy. Notably, these advancements could offer substantial improvements in terms of reduced calibration times during tuning processes and the avoidance of costly trial-and-error iterations.

Chapter 7

Datasets for Shock Testing

In addition to developing predictive models, understanding shock physics is crucial for advancing equipment qualification techniques in aerospace. Experimental datasets from pyroshock tests play an essential role for this purpose. Jonsson developed a shock test facility in [58] and presented some results in terms of SRS. However, these tests analyzed a limited set of parameters and configurations, restricting a comprehensive understanding of their interactions. Similarly, Castro presented impact test data on a resonant plate in [107], but the limited configurations and plate geometry did not fully align with typical pyroshock test setups, limiting their applicability.

Currently, the literature lacks exhaustive open-access datasets focused specifically on pyroshock qualification tests. To fill this gap, some experimental campaigns have been developed to better investigate and understand the physics of pyroshock tests.

This chapter aims to achieve several objectives. Firstly, it seeks to propose experimental datasets that can serve as valuable resources for studying pyroshock phenomena. Furthermore, these datasets will be utilized to investigate the influence of different parameters on SRS behavior. Finally, the data will be exploited to validate the comprehensive simulation model in different experimental configurations.

7.1 A Full Factorial Dataset

Shock test data involving a resonant plate were collected at the Marcus Wallenberg Laboratory for Sound and Vibration Research (MWL) of the KTH Royal Institute of Technology. This extensive dataset was systematically generated using Design Of Experiments (DOE) methodologies, enabling a comprehensive exploration of various parameters. It has been made openly accessible to the scientific community and can be accessed via the link https://zenodo.org/doi/10.5281/zenodo.10371545 [108]. This dataset serves as a valuable resource. In addition to providing a detailed description of the dataset and its experimental setup, the dataset allows the examination of parameter influences on SRS acceleration results. This analysis is crucial for accurately calibrating qualification tests. Furthermore, the proposed predictive model, exploiting a digital twin approach, is applied to the dataset and subjected to further validation.

Given that the dataset includes force profiles corresponding to each impulse, there is an opportunity for an in-depth exploration of shock physics. This involves comparing real force profiles with those simulated by the model to gain deeper insights into the dynamics of the system.

7.1.1 Experimental Setup

The test rig at the MWL Lab of the KTH Royal Institute of Technology in Stockholm used for the dataset acquisition consists mainly of a resonant plate made of aluminum alloy (Al6061). The mechanical properties of the latter aluminum alloy have been considered equal to $E_p = 69$ GPa, $\nu_p = 0.33$, $\rho_p = 2700$ kg/m^3. Figure 49 shows the bare resonant plate in a specific configuration with fixed boundary conditions. Indeed, the tests include different arrangements. The plate was both suspended (to simulate the free boundary conditions) and fixed to a mixed concrete and steel base by means of viscoelastic supports (to simulate fixed boundary conditions in three points avoiding the dynamic influence of the external elements).

The resonant plate has an irregular quadrilateral geometry and a constant thickness equal to 20 mm. The plate dimensions are shown in Figure 50. A Cartesian coordinate system (X-Y-Z) with the origin fixed in a corner of the plate and the XY plane lying on the surface of the plate has been used as a reference in the present section.

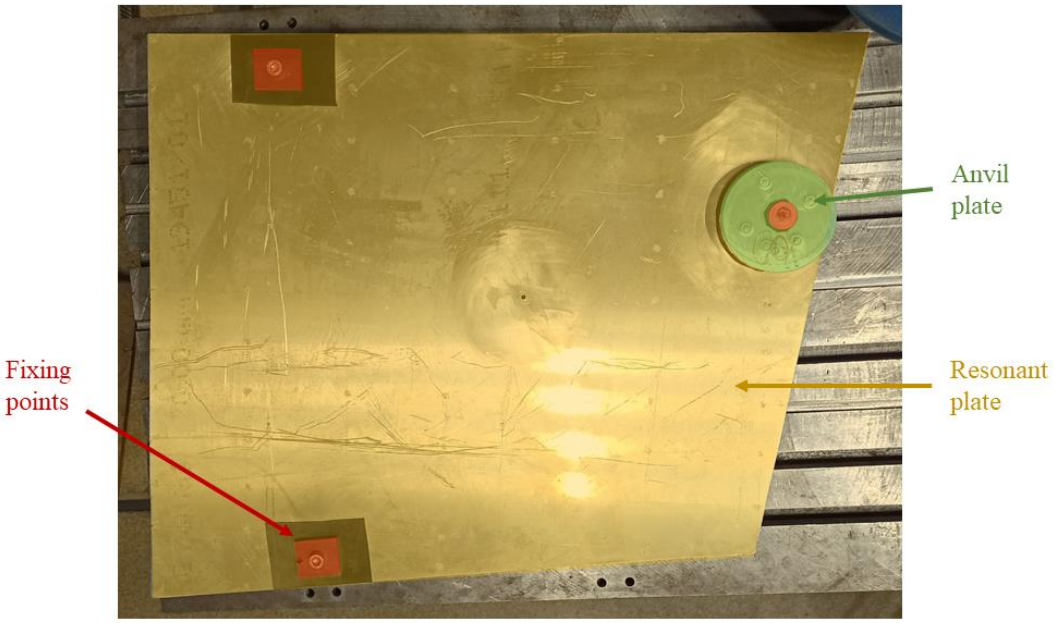

Figure 49. Bare resonant plate in a fixed configuration. In addition to the plate, the base, the anvil plate, and the three fixing points interposed by polymeric layers to avoid micro-impacts due to metal-metal contact are shown.

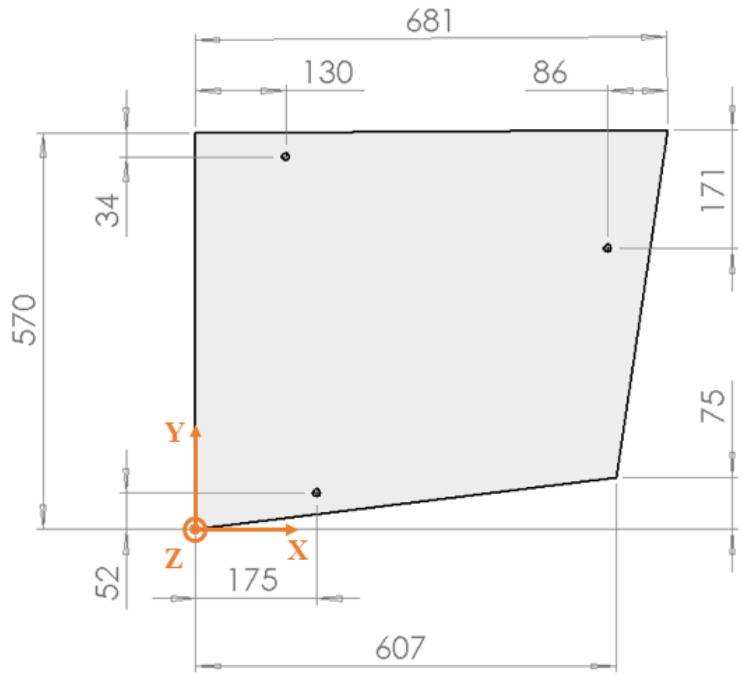

Figure 50. Geometry and dimensions (expressed in mm) of the plate. The resonant plate has a thickness equal to 20 mm.

In addition to the resonant plate, the test facility includes many other components and can be set in several configurations. The latter are described in detail in Subsection 7.1.3. In general, the resonant plate was excited with impacts by means of an impact hammer. Each test lasts 61 s and contains 10 impacts at approximately regular intervals. The first impact is applied after 1 s of recording, while the subsequent ones have a regular cadence about every 6 seconds. The free response of the plate has a duration of about 4-5 seconds as the oscillation of the plate was manually damped before each new impact to avoid overlapping effects of the responses.

7.1.2 Sensors and Acquisition

The primary objectives of the provided dataset are dual: to elucidate the response of the plate to impulsive excitations and to comprehend the underlying impact physics, particularly with regard to the applied force profiles. To achieve these goals, seven accelerometers were strategically positioned to capture the plate response at various locations. Additionally, an impact hammer, equipped with a load cell for recording applied force, was utilized. An additional accelerometer was incorporated on the hammer for indirect measurements, such as estimating impact velocity. All the accelerometers mounted on the plate (B&K 4394) are single axis Integrated Electronics Piezo-Electric (IEPE), with frequency range 1–25.000 Hz (amplitude ±10%, phase ±5°), nominal resonance frequency of 52 kHz, and nominal sensitivity of 10 mV/g. The impact hammer is the Dytran Dynapulse 5800B4 with sensitivity of 2.2 mV/N, and interchangeable impact tips. Finally, the accelerometer mounted on the impact hammer is a B&K 8309 charge accelerometer with a measuring range of up to 15000 g peak. The latter sensor was suitably calibrated, and its signal was converted using a B&K 2635 charge amplifier. The masses of the individual accelerometer and of the impact hammer were measured respectively equal to 4 grams and 186 grams. Figure 51 shows the impact hammer adopted with the related accelerometer.

The accelerometers were fixed on the resonant plate as depicted in Figure 52. Table 13 lists the coordinates of each measurement point and the technical information related to the acquisition channels. The specific sensitivities of the accelerometers have been set to record the time histories of the acceleration in g. The point named G has a threaded connection to the accelerometer, while all the others have been fixed using a cyanoacrylate glue. Point C coincides with the intersection of the diagonals of the trapezoidal plate.

Figure 51. Impact hammer with the mounted accelerometer (B&K 8309).

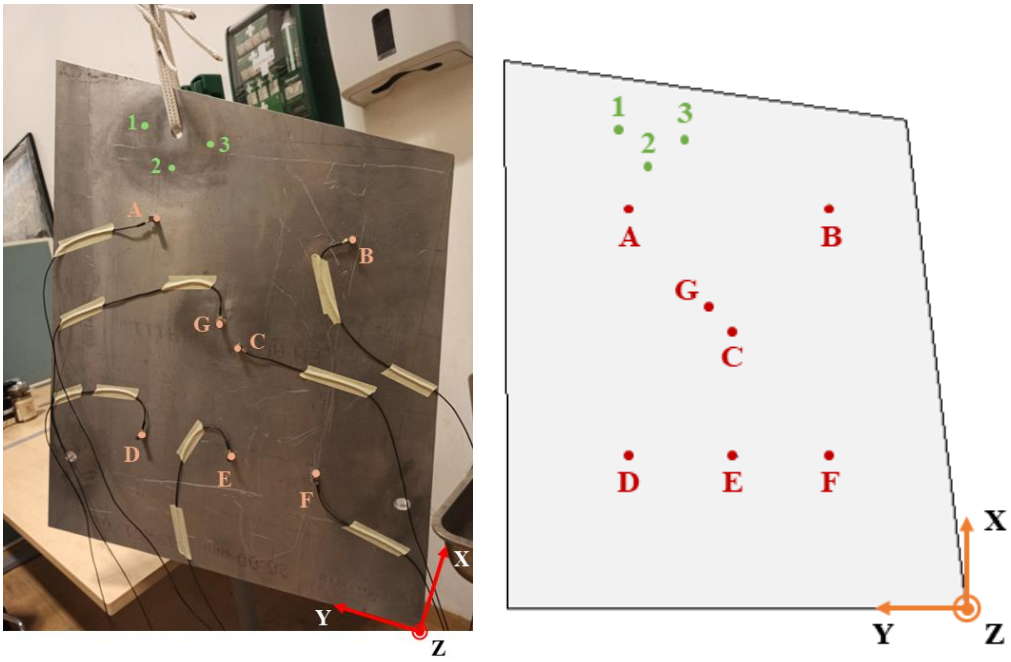

Figure 52. On the left, picture of the resonant plate with mounted accelerometers. On the right, scheme inherent to the positioning of the accelerometers (letters in red) and impact positions (numbers in green).

Table 13. Coordinates of the measuring points for each accelerometer and related technical data.

Position	X (mm)	Y (mm)	Model	S/N	Sensitivity
A	498	420	B&K 4394	30524	9.738 mV/g
B	502	169	B&K 4394	30519	9.999 mV/g
C	348	292	B&K 4394	30791	9.934 mV/g
D	190	420	B&K 4394	30522	9.835 mV/g
E	190	286	B&K 4394	30525	9.836 mV/g
F	190	169	B&K 4394	30521	9.816 mV/g
G	374	319	B&K 4394	30520	9.992 mV/g
Hammer (Acceleration)	-	-	B&K 8309	31217	0.04412 pC/g
Hammer (Force)	-	-	Dyn. 5800B4	4083	2.2 mV/N

The acquisition system is composed of a cDAQ-9178 chassis equipped with three 4-channels NI-9234 modules with sampling frequency $f_s = 51.2$ kHz/channel. The input signal on each channel is sampled by a 24-bit Delta-Sigma Analog to Digital Converter (ADC) and all the modules are synchronized by sharing a single master timebase source.

7.1.3 Parameters and Design of Experiments

The proposed dataset was meticulously curated to allow a comprehensive exploration of shock tests, aiming to identify key parameters influencing contact mechanics and subsequent test outcomes, particularly regarding SRS acceleration. To achieve this, the different configurations to be measured were defined by a DOE [109,110] based on a full factorials model as applied, for example, in [111]. Unlike the One-Factor-at-A-Time (OFAT) methods [112], the full factorials ones allow to find the best trade-off between the amount of tests and the analysis of the effects of the parameters, including also their interactions.

The number of necessary tests defined by the full factorials DOE is equal to the product of the levels considered for each factor. Therefore, the selection of the parameters and their levels was made to consider as many significant configurations as possible while maintaining an adequate total number of tests. Based on this, six

parameters were selected: (1) impact position, (2) hammer speed, (3) hammer head tip, (4) anvil plate material, (5) anvil insulator, and (6) plate boundary conditions. Two or three levels have been established for each parameter, as outlined in Table 14. Since the factors can be both quantitative and qualitative, the levels (low, high, and sometimes middle) have been assigned in a purely arbitrary way in the second case.

Finally, it is important to note that certain parameters are interdependent, necessitating consideration of their mutual constraints. For example, the application of a polymer anvil insulator presupposes the presence of an anvil plate. Consequently, the total number of acquisitions conducted amounts to $3^2 \cdot (2^4 + 2^2) = 180$ tests, where each test contains 10 impulses along with the corresponding plate responses.

Table 14. Test factors and related levels considered for the full factorial DOE.

Factor Name	Low-level	Mid-level	High-level
Impact position (input)	#1	#2	#3
Hammer speed	Low	-	High
Hammer head material (Curvature radius)	Aluminum (30 mm)	Delrin (30 mm)	Polyurethane (15 mm)
Anvil plate material	None	Aluminum	Steel
Anvil insulator	None	-	Polymeric
Plate boundary conditions	Free	-	Fixed

Table 15. Coordinates of the impact positions.

Impact position	X (mm)	Y (mm)
#1	595	434
#2	565	404
#3	595	374

The following list provides a more detailed description of the parameters and their levels:

- The **impact position** was strategically delineated in 3 distinct points within a delimited region of the plate. This selection was made to ensure consistency in impact application across conditions, including those involving an anvil plate. Figure 52 illustrates the designated points, while their corresponding coordinates are detailed in Table 15.
- The **hammer speed** (as well as a generic impacting body) was defined on two generic levels: high and low. The speed is determined empirically by the operator and can be computed in the post-processing phase thanks to the accelerometer mounted on the impact hammer itself.
- To analyze in depth the effects of material composition and curvature radius of the impacting body on the pulse force profile, three diverse **impact tips** were employed: aluminum, polyurethane, and Delrin (also referred to as Polyoxymethylene). These tips, depicted in Figure 53, were selected to offer insight into how variations in material and curvature radius influence the pulse force profile. The respective curvature radii were estimated at 30 mm for aluminum and Delrin tips, and 15 mm for the polyurethane tip.

Figure 53. From left to right: impact tips adopted during the tests; side views with a focus on the curvature radius of the impact tips in aluminum, Delrin, and Polyurethane.

- The investigation into the effect of the **anvil plate** on shock tests involved three distinct conditions: (1) the baseline scenario consisting of the bare resonant plate, without any anvil plate; (2) the inclusion of an aluminum anvil plate, characterized by a circular shape with a radius measuring 50 mm and a thickness of 18 mm; and (3) the integration of a steel anvil plate, which exhibits a square shape with each side measuring 100 mm and a thickness

of 10 mm. The visual representation of these anvil plates is illustrated in Figure 54.

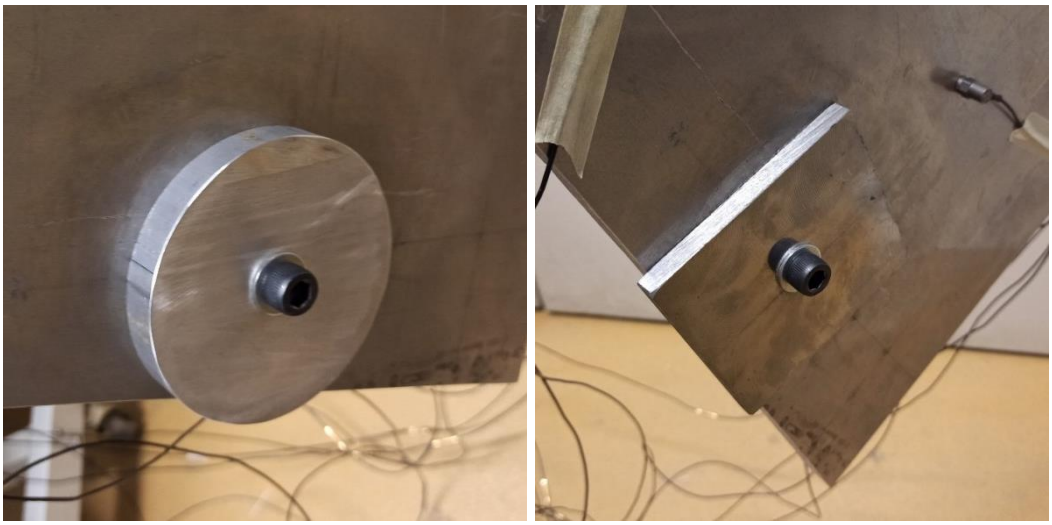

Figure 54. Anvil plate made of aluminum alloy (on the left) and steel (on the right).

- The investigation also dealt with the potential effect of damping materials or polymeric layers to mitigate metal-to-metal contacts and tune the SRS acceleration. This analysis includes scenarios both with and without the presence of an **anvil insulator**. It is worth noting that the introduction of an anvil insulator is dependent on the presence of an anvil plate. The anvil insulator, depicted in Figure 55, comprises a polymeric disk characterized by a radius measuring 50 mm and a thickness of 13 mm.

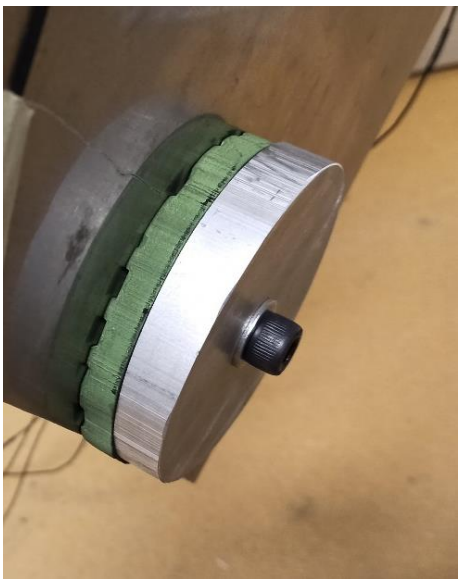

Figure 55. Anvil insulator consisting in a green polymeric disk placed between the resonant and the anvil plates (in this specific case, the aluminum anvil plate).

- Finally, the **boundary conditions** of the resonant plate have been named as free and fixed. The former BCs were simulated by hanging the plate through cables and springs in order to isolate the plate system and avoid any external interaction. The alternative condition consists of fixing the plate in 3 points on a mixed concrete and steel base. The fixing was achieved by means of threaded connections on 3 cylindrical supports made of viscoelastic composite material. These supports can be modeled as cylinders with a diameter of 50 mm and a height of 48 mm. These two configurations are shown in Figure 56.

Figure 56. Configurations with free (on the left) and fixed (on the right) boundary conditions.

The reader is referred to Appendix A for the complete test list with the related filenames and operating conditions.

7.2 Investigation on Parameters Effect

This section presents an initial analysis aimed at examining the influence of each parameter on the SRS acceleration. A similar investigation was conducted in [58], where variations in some SRS curves were depicted relative to specific parameters. However, the former study exhibits several limitations, including the absence of repeated tests to ensure statistical significance, the consideration of specific and limited configurations (resulting in the absence of a full factorials dataset), and an incomplete description of all experimental conditions necessary for a comprehensive numerical simulation of the outcomes. The present dataset addresses these limitations. Figure 57 illustrates the graphical outcomes, highlighting the behavior of the SRS curves as each parameter encounters variation.

The presented results were derived from processing the measured experimental data. Specifically, responses to the 10 impulses were extracted from each recording, uniquely identified through the force signal. Subsequently, the mean value of each

accelerometric signal over time was subtracted, and the SRS accelerations were computed using the standardized method proposed by Smallwood [13,21]. Consequently, 10 SRS curves were generated for each sensor, and their distributions were recreated by calculating the mean value $\bar{x}_{SRS}$ and standard deviation σ_{SRS}. The region of the graph bounded by $\pm\sigma_{SRS}$ thus signifies the range where the SRS curves exhibits the highest density. The more the region is restricted, the more the tests are repeatable and not influenced by external or random factors. Consequently, the evident differences between distributions reflect the actual influence of the observed parameter. The effect of each parameter is considered as the difference between the means of the results ($\bar{X}_{SRS}$ and σ_{SRS}) among its two or three levels. Figure 57 shows the graphical results of the effect analysis per each parameter with reference to the response in point C.

Some interesting observations can be drawn from these preliminary results. In general, the distributions are on average wider at high frequencies. This may be due to the inherent challenge of perfectly replicating the same experimental conditions when considering responses at high frequencies. Indeed, minor variations in the impact can result in significant differences in the plate response at high frequencies. Minor variations in the impact refer to, for example, inaccuracies in the excitation point, and direction and magnitude of the applied force. Specifically, the effects of each parameter are analyzed in the following list:

a) The **impact position** plays a visible influence on the SRS, particularly for some specific modes of vibration. In fact, a different point of impact excites the system with different modal participation factors. Consequently, while the general trend of the distributions remains consistent, the effects become statistically significant in alignment with specific modes. For a comprehensive examination, Figure 58 illustrates the outcomes of the modal analysis up to approximately 1 kHz, considering the free resonant plate. It is worth noting both the asymmetry of the mode shapes depending on the plate geometry, and the position of the nodes and the relevant modal contributions as the excitation and measurement positions vary.
b) The **velocity** of the impacting body does not significantly affect the shape of the distribution but primarily influences the magnitude of the resulting accelerations. This is shown by the shift in the magnitude of the distributions.
c) The choice of impact **hammer tips** significantly influences the trends observed in the SRS. In fact, the stiffer the material, the shorter the pulse duration, according to the Hertzian contact theory. Consequently, impacts

characterized by shorter durations in the time domain tend to excite higher frequencies. Conversely, less stiff materials produce pulses with longer durations, leading to a narrower excited frequency band. Specifically, the aluminum tip exhibits a higher cutoff frequency compared to Delrin, which, in turn, surpasses polyurethane. The variations in amplitude, on the other hand, likely derive from the necessity of maintaining energy balance, accounting for losses. Thus, the energy contained in the high frequencies of the aluminum case is redistributed to the low frequencies, characteristic of the polymeric cases.

d) The analysis of the **anvil plate** reveals no significant differences. When utilizing an aluminum alloy, impacts tend to cut off at lower frequencies, whereas those with a steel anvil plate appear to reach slightly higher frequencies. Notably, the configuration labeled "None" corresponds to direct impacts on the resonant plate, which is composed of an aluminum alloy. Interestingly, its behavior is similar to the configuration with the aluminum anvil plate, as depicted in Figure 57. However, the distinctions among the three analyzed cases lack statistical significance, as the distributions do not exhibit clear differences but rather overlap. This lack of differentiation may depend on the high elasticity values present in both materials.
e) The presence of the **anvil insulator** introduces a low-pass filter. Indeed, the distribution has the same shape from 2 kHz upwards but reaches smaller amplitudes.
f) Finally, it is worth noting that the behavior of the two setups in terms of **boundary conditions** may be similar. Indeed, the fixed boundary condition is equivalent to the free-free condition, since the two distributions are almost perfectly superimposable and do not show significant differences.

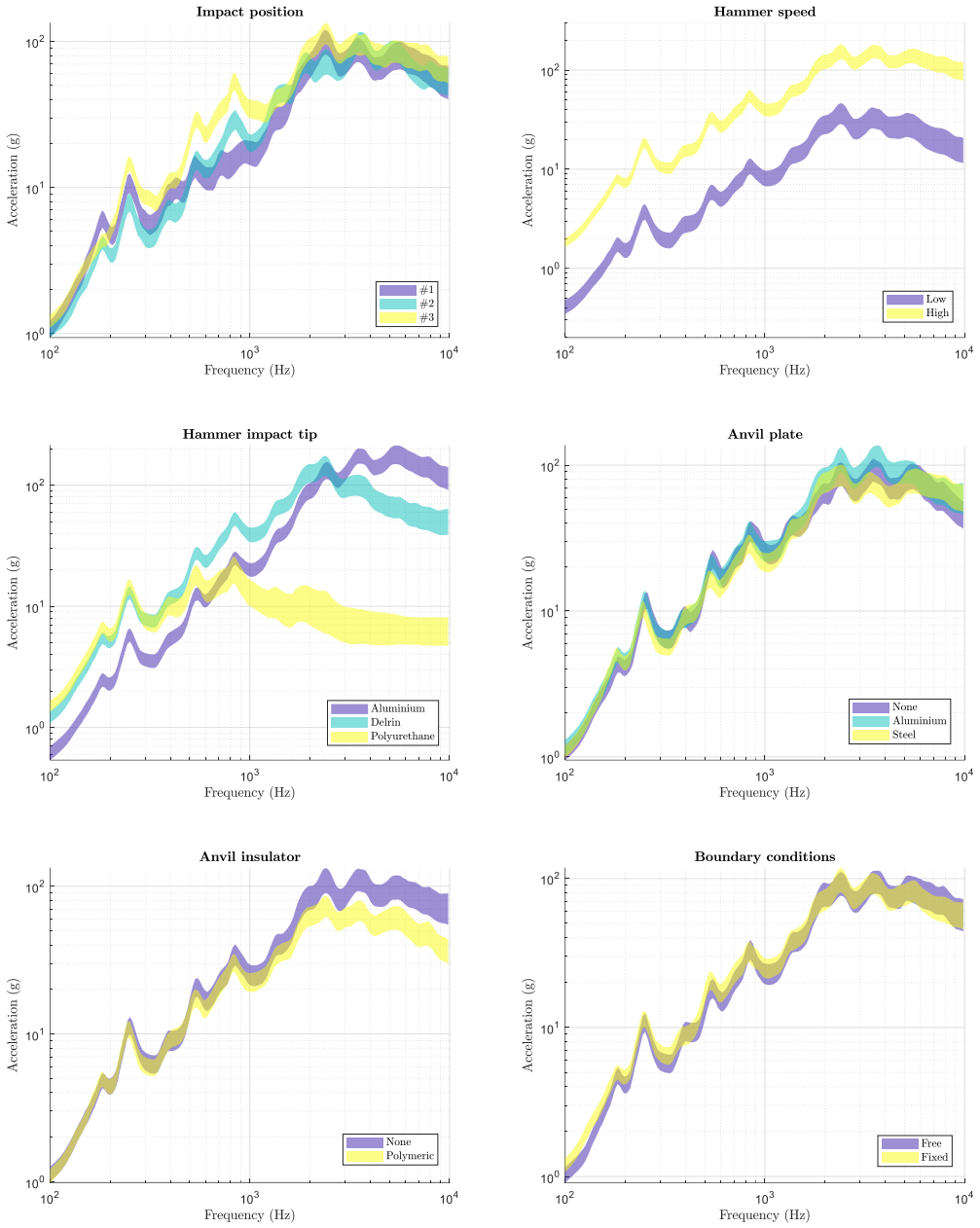

Figure 57. Analysis of the effects due to each individual parameter. Charts show the SRS distributions included in the range $\bar{X}_{SRS} \pm \sigma_{SRS}$.

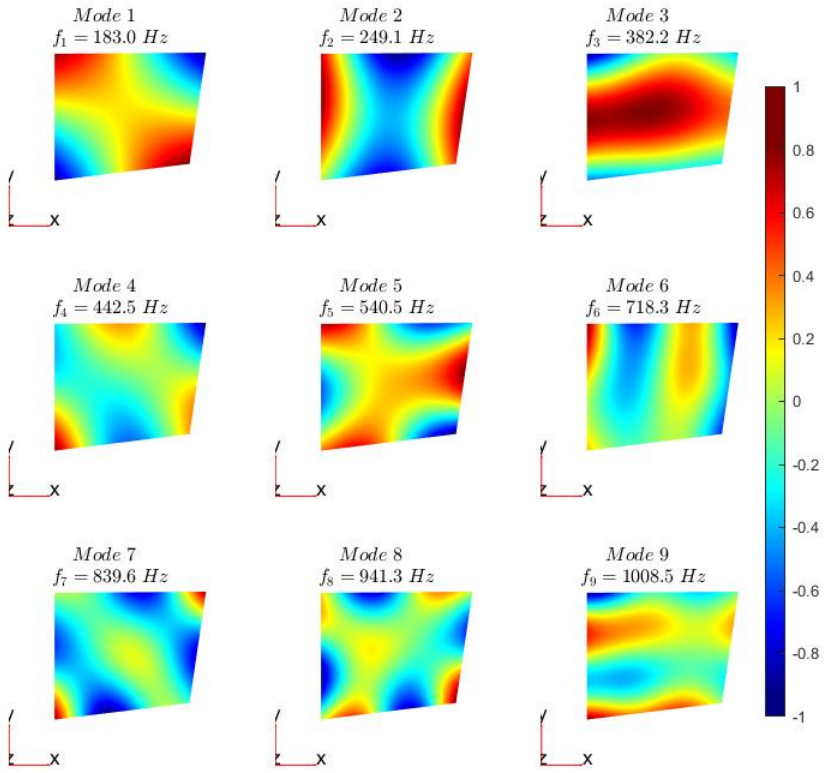

Figure 58. Modal analysis of the free resonant plate considering the modes up to 1 kHz.

7.3 Dataset Analysis

After detailing the proposed dataset and examining the individual effects of the considered parameters, this section proceeds with the validation of the shock test simulation model. Furthermore, an extensive analysis of the shock physics and its definition in the same predictive model are introduced. Given that the resonant plate used for data collection is defined, the validation outlined in this phase utilizes the model to solve the direct problem, i.e., to predict the momentum. Consequently, the results are shown as percentage errors with respect to the momentum which minimizes the established cost function (specifically, the RMSLE). On the other hand, the accuracy associated to the definition of the impulse force profile is evaluated by analyzing the percentage error of the impulse duration τ_{el} and of the restitution coefficient e. These two parameters are crucial in recreating the impulse force profile.

7.3.1 Numerical Model Validation

Using the aforementioned predictive model, it becomes feasible to derive the predicted SRS acceleration for each measurement point, assuming the mass of the impacting body m_s equal to that of the impact hammer plus the added accelerometer. The velocity v_s of the impacting body is estimated by identifying the portion of the signal associated with the impact and integrating the signal from the accelerometer positioned on the hammerhead after appropriate processing. Evaluating the numerical model through a simple cost function, such as RMSE, would not allow the outline of absolute conclusions about the goodness of the predictive model, except in relative terms through a comparison between different experimental conditions. Therefore, a different criterion was chosen for this evaluation. Specifically, since the main objective of the model for simulating pyroshock tests is to predict the momentum required to calibrate the test bench and meet the SRS requirements, the chosen cost function is the percentage error on this prediction, $\Delta p_{\%}$. This score is calculated based on the measured momentum (used to obtain the simulated curve) and the optimal momentum (i.e., the one that minimizes the error between the simulated and experimental curves). Consequently, the percentage errors of the momentum for each individual impact can be calculated, with the optimal momentum $\Delta p_{s,opt}$ serving as a reference. This optimal momentum can be obtained by minimizing the selected cost function RMSLE. Figure 59 shows two exemplary comparisons of the SRS obtained: experimental, predicted, and optimized. In the left graph (impact #1 of test #1, measured at point C) the percentage error of the model is 1.5%. In fact, the obtained curve is almost coincident with the optimal one and satisfactorily follows the experimental curve. In the right graph (impact #5 of test #1, measured at point C), the error is -16.1%. Indeed, the predicted SRS still faithfully follows the experimental curve but slightly underestimates it. It is worth noting that the tolerances on pyroshock test requirements defined by standards are usually defined in the range of +6 dB and -3 dB with respect to the nominal spectrum. In percentage terms, this could translate into the range of +100% and -50% of the nominal curve. This observation leads to consider the prediction with an error of -16.1% quite satisfactorily.

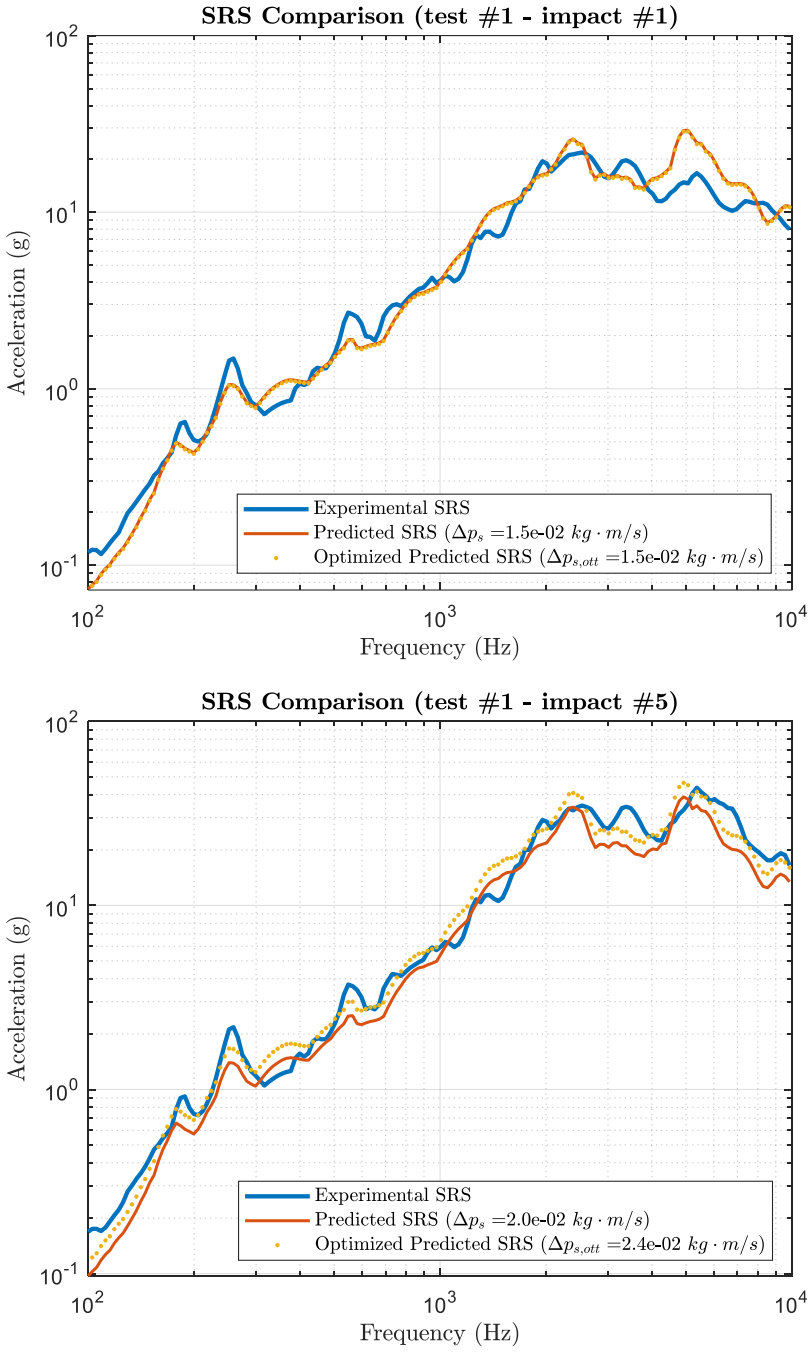

Figure 59. Comparison of the experimental, predicted and optimized SRS inherent to the measurement in point C. The percentage errors are respectively equal to 1.5% for the chart above and -16.1% for the one below.

The matrix in Figure 60 contains the absolute values of the percentage errors averaged for each recording and helps evaluate the average accuracy of the

predictive numerical model. It is thus possible to observe the accuracy as the measurement position and the experimental conditions vary. The simulations have satisfactory values lower than 27% on average.

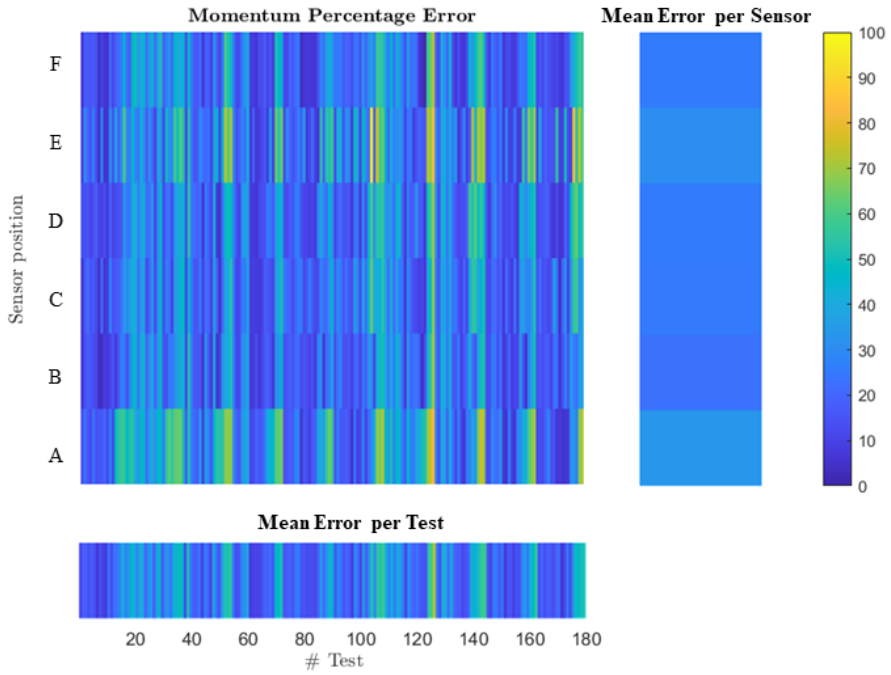

Figure 60. Percentage error matrix as the measurement position (sensors) and experimental conditions (# test) vary.

The highest errors seem to concentrate at positions A and E of the sensors. Additionally, periodicity in the error peaks becomes evident under the experimental conditions, indicating that the error (and consequently, the model accuracy) is particularly influenced by specific parameters. The periodicity concerning the number of tests becomes even more apparent when observing the experimental conditions of each test, as highlighted in Appendix A. In this instance, the critical parameter is identified as the hammerhead tip (Polyurethane), and the subsequent subsection offers insight into the causes of this error. By calculating the average percentage error while filtering the tests based on the critical parameter, values equal to 24% (aluminum tip), 18% (Delrin tip), and 39% (Polyurethane tip) are obtained. Figure 61 further validates this observation. Indeed, the optimized momentum values notably deviate from those applied, particularly for tests with the Polyurethane tip at high impact velocities.

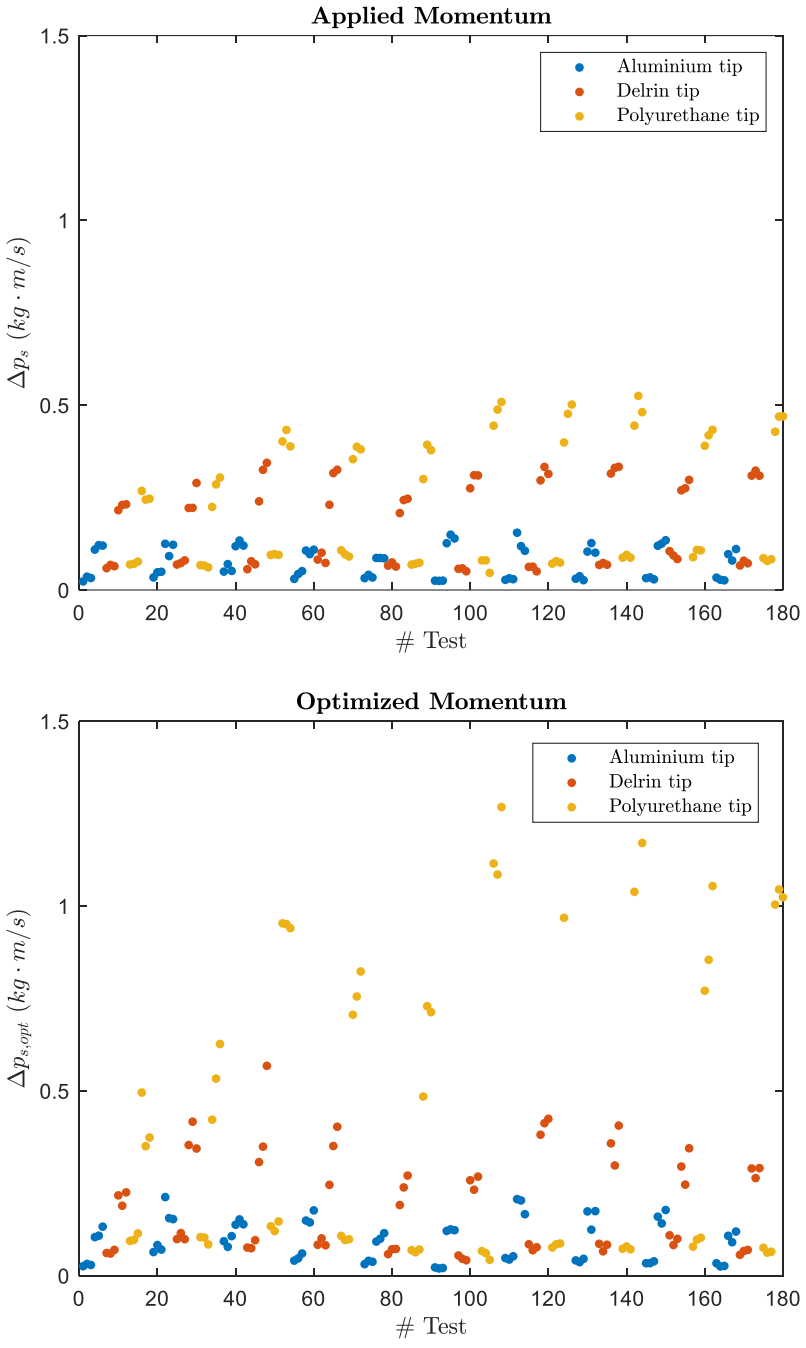

Figure 61. Applied (above) and optimized (below) momentum per each test by distinguishing the hammerhead tip.

It is further interesting to notice that the simulation error increases as the frequency increases, as is assumable in the case of numerical models such as the FEM. Indeed, by defining three frequency bands as low (100-500 Hz), middle (500-2000 Hz), and high (2000-10000 Hz), the average percentage errors may be respectively computed equal to 18%, 29%, and 38%. In fact, the accuracy of FEM is influenced by the mesh density. FEM tends to provide more accurate approximations at lower frequencies, as a relatively coarse mesh might be sufficient [113]. Please remember that the FE mesh is chosen in order to optimize the accuracy-computation times trade-off. This approach aims to cover a broader spectrum of frequencies of interest and their corresponding mode shapes.

7.3.2 Shock Physics Insight

The impulse serves a crucial role in pyroshock tests, and thus, its precise definition within the simulation model is fundamental for achieving accurate results. The provided dataset, comprising force signals from 1800 pulses, facilitates an investigation into the parameter influence on the resultant force profile. In the predictive model, the impulse is formulated as a signal in the time domain, and the function $F(\omega)$ is subsequently obtained in the frequency domain. Given its impulsive origin, the function $F(\omega)$ can behave approximately like a low-pass filter. Consequently, the shape and duration of the force profile greatly influence the results of the pyroshock tests. As previously described, the force-over-time signal is generated using three main parameters: (a) the impact duration, (b) the coefficient of restitution, and (c) the mathematical function describing the curve shape. It has been demonstrated that the von Hann window function, also known as the raised cosine function, faithfully follows the force signal generated during a real impact.

The predictive model exploits the Hertzian contact theory to estimate the duration of the collision. This theory considers an impact accompanied by a deformation and, consequently, the displacements of the bodies can be calculated as a function of the applied force. Hertz's theory lays its foundations on several assumptions, such as quasistatic and elastic contacts, spherical, isotropic, and homogeneous bodies [71–73]. Gugan proposes in [74] a simplified formulation of the Hertz contact theory, considering one of the two bodies with a flat surface (alternatively, the curvature radius of the plate tending to infinity). For a perfectly elastic collision, the total contact duration τ can be estimated as twice the time necessary to reach the maximum compression, as reported in Eq. (25). All these parameters involved in Eq. (25) have been considered in the acquired dataset, leading to a good level of investigation on the pulse definition.

Given the challenge of achieving a perfectly elastic collision in real-world scenarios, it becomes necessary to modify the estimation of the total contact duration, τ. In practice, real impacts are often characterized by inelastic behavior, resulting in a partial loss of energy. Therefore, the decision to divide the force profile into two phases was made, as shown in Figure 62. The behavior in the first compression phase can be considered as perfectly elastic, and its duration $\tau_{el} = \tau/2$ can be estimated using Eq. (25). Subsequently, the material plasticization is considered during the second phase of impact, with a duration, τ_{an}, dependent on the Coefficient Of Restitution, e. This coefficient, defined as the ratio between the relative speed of separation and approach (i.e., post- and pre-collision) of the bodies, serves as a measure of inelasticity [114]. Furthermore, the COR is used to adjust the momentum applied in the simulation model in accordance with the law of conservation of momentum, as described in (27).

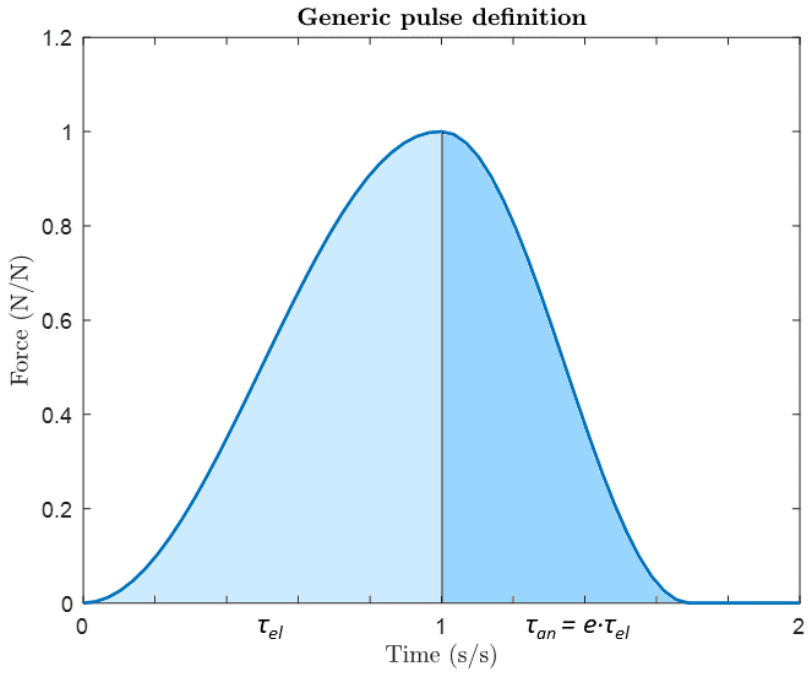

Figure 62. Generic pulse definition through its three main characteristics: shape of the curve, duration, and coefficient of restitution. The pulse is divided into a first elastic and a second inelastic phase, and the axes have been normalized.

In the literature, various models exist for estimating the COR. Among these, the theories proposed by Zener [85] and Weir-Tallon [86] are commonly cited, particularly for impacts between a sphere and a plate. A comparative analysis of these theories is presented in [99]. In particular, the COR calculated according to Zener's

theory varies with the ratio between the plate thickness and the sphere diameter (or equivalently, the curvature radius R_s). On the contrary, the latter ratio does not influence the value of e according to Weir-Tallon's formulation. Furthermore, Zener's theory constrains the COR in the range between 0 and 1, where 0 signifies a completely inelastic collision and 1 denotes a perfectly elastic collision. In fact, a value of e minor than 1 represents a loss of the initial kinetic energy. Only in the presence of an energy gain (e.g., due to chemical reaction during the collision) the COR may be exceed 1. Considering the nature of tests contained in the dataset, where e must lie within the range of $0 \leq e \leq 1$, the estimation of the COR based on Zener's theory was deemed appropriate for this specific scenario, as outlined in Eqs. (36)-(37).

$$\mathrm{e} = \exp\left(-1.7191 \cdot \lambda\right) \tag{36}$$

$$\lambda = \frac{1}{4\sqrt{3}}\left(\frac{\pi\rho_s}{\rho_p}\right)^{\frac{3}{5}}\left(\frac{2R_s}{z_p}\right)^{2}\left[\frac{u_s^2\rho_p(1-\nu_p^2)}{E_p}\right]^{\frac{1}{10}}\left[1+\frac{E_p(1-\nu_s^2)}{E_s(1-\nu_p^2)}\right]^{-\frac{2}{5}} \tag{37}$$

where ρ_s and ρ_p are respectively the density of the materials constituting the impacting body and the plate, while z_p is the plate thickness. In cases where the anvil plate and anvil insulator were used, the value of z_p was adapted to take into account the total thickness of the system during impacts.

As observed so far, the contact characterization is based on the extracted features from the time histories of the force signals. Consequently, three specific instants in the time signal for each pulse were identified to obtain the values of τ_{el} and e (and, by extension, τ_{an} and τ). These characteristic instances are the initial contact time, denoted as t_i, the time of peak force occurrence, referred to as t_{MAX}, and the final contact time, designated as t_f. Figure 63 illustrates the identification of these three temporal points with reference to the first impact of test #1. The calculation of the elastic collision time $\tau_{el} = t_{MAX} - t_i$ is straightforward. Furthermore, it can be proved that $e = \frac{t_f - t_{MAX}}{t_{MAX} - t_i} = \frac{\tau_{an}}{\tau_{el}}$ and, consequently, $\tau_{an} = e \cdot \tau_{el}$.

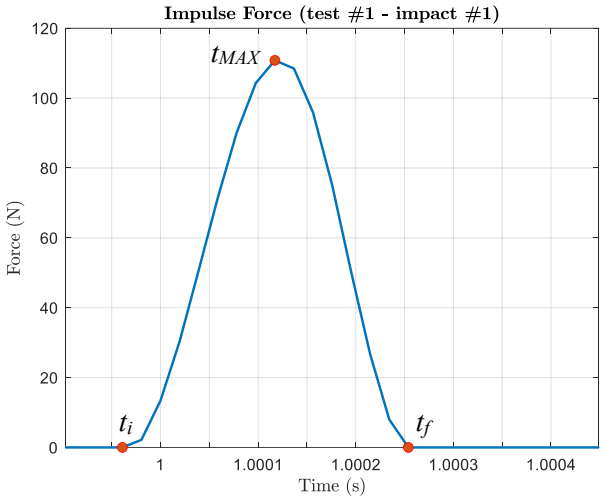

Figure 63. Time history of the force signal measured during impact #1 of test #1, highlighting the identification of t_i, t_{MAX} and t_f.

After acquiring all the experimental values of τ_{el} and e from each impact, the percentage errors of the same estimated values (during the momentum definition phase of the numerical model) were computed. Figure 64 illustrates the errors obtained, with a focus on the critical parameter for impact modeling, the hammerhead tip. While the error on the COR is approximately constant for all the impact tips and is underestimated on average by -25%, the error in estimating the contact duration varies depending on the impact tips parameter. Specifically, the average error for the aluminum tip is equal to 8%, rising to 15% for the Delrin tip, and reaching 33% for the Polyurethane tip.

The underestimation on the COR obtained by the model can be attributed to the fact that the experimental values exceed the maximum value of 1 in several circumstances. This discrepancy is evident in the comparison between experimental and estimated values depicted in Figure 65. The phenomenon of experimental values exceeding the threshold of 1 may partially depend on a low time resolution of the recorded signal. Although the sampling frequency $f_s = 51.2$ kHz is decisively high, the total pulse duration is in the order of magnitude of 10^{-4} s (as can be seen in Figure 63). This leads to errors in the recognition of t_i, t_{MAX} and t_f which accumulate in the estimates of τ_{el} and e. Moreover, experimental values of e exceeding 1 could result from actual energy release due to operator influence. Despite efforts to minimize grip influence during testing, its leverage may not be negligible and could affect the impulse force profile. Given the significant relevance of the pulse definition phase on the numerical model for simulating pyroshock tests, it is plausible

that the inaccuracies related to Δp_s obtained in Section 4.1 could be partially influenced by these errors.

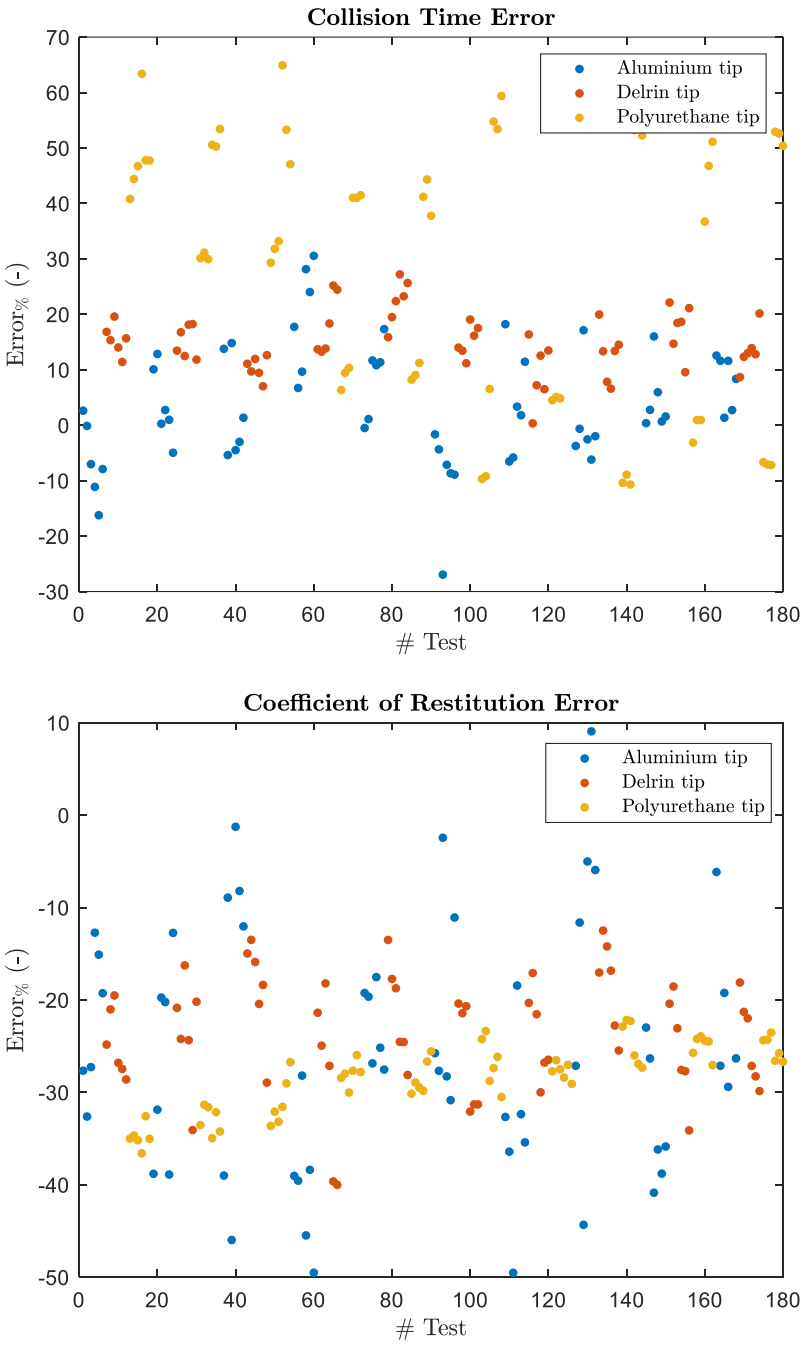

Figure 64. Percentage errors of the elastic collision duration τ_{el} (above) and of the coefficient of restitution e (below).

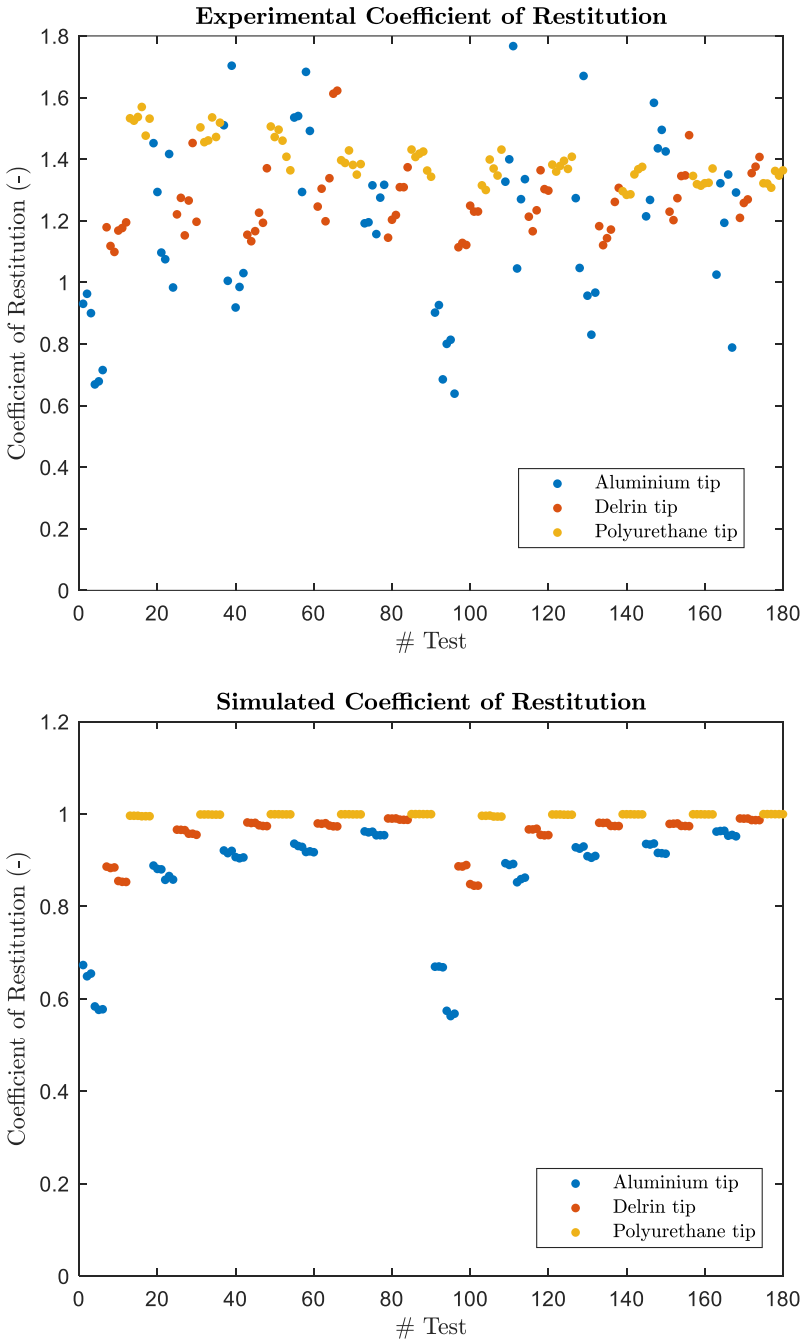

Figure 65. COR values obtained from the experimental tests (above) and estimated through the pulse definition of the predictive model (below).

In conclusion, this chapter introduced a comprehensive full factorials dataset for an exhaustive exploration of shock tests involving resonant plates. Alongside detailed descriptions of the experimental setup and data acquisitions, the analysis focused on investigating how experimental configurations influence test outcomes in terms of SRS. This examination sheds light on the physics and behavior of shock test facilities, offering valuable insights for enhancing empirical tuning techniques. Additionally, a validation of the numerical model for simulating pyroshock tests was presented, focusing on its strengths and limitations.

The predictive model exhibited particular sensitivity to the typology of hammerhead tip, demonstrating less accuracy with less stiff materials such as polyurethane. Notably, percentage errors in momentum were generally satisfactory when the contact involved materials with a high Young's modulus. However, errors increased up to 39% in cases involving the polyurethane tip. Furthermore, the analysis deepened contact mechanics, comparing measured and simulated force-time signals. It revealed higher errors in estimating contact duration and COR for tests involving the polyurethane tip. These errors in the impulse definition phase could potentially influence the overall accuracy of the model.

Chapter 8

Design of the Politecnico di Torino Test Facility

In this final chapter, a test bench design for the experimental simulation of pyroshock is proposed. Exploiting the acquired knowledge, predictive models, and experimental campaigns on impact tests, it has been possible to design a test bench capable of controlling all the significant parameters. In addition to the proposed design, calculations and decisions made to reach the final project are briefly presented.

The systematic literature analysis revealed that most test benches use a plate as a resonant fixture to reproduce pyroshock responses. However, within this broad set, numerous differences characterize the usage of adopted plates. These configurations vary, for example, based on the direction of the applied impulse with respect to the plate (IP or OOP), the type of plate connection or boundary conditions (e.g., fixed through threaded connections or free using chains or wires), the orientation of the plate (vertical or horizontal), and the presence of insulating materials to decouple the system from the supporting structure. While the theme concerning the geometry and dimensions of the resonant plate has already been addressed through optimization models described in Chapter 6, these other design choices are addressed and described in this chapter. Furthermore, despite these optimization models facilitate the definition of the plate design and provide some results, the design of the structure supporting the plate was carried out with the aim of ensuring

maximum flexibility and thus anticipating plate changes. For this reason, extreme cases were considered to define the project requirements.

While most works in the literature have adopted a resonant plate, no clear preference regarding the exciter typology has been observed. To be more precise, a large portion of studies uses mechanical exciters, but within this category, variability is high. The exciter described in this thesis consists of a pneumatic gun, considered more effective for pyroshock simulation and allowing the adjustment of many parameters for calibration. Alternatively, the implementation of a pendulum to excite the resonant plate has also been considered and may be part of future developments of this work, as it would allow for further investigation into impact mechanics. For this reason, the test bench, in its entirety, has been designed primarily with two elements: a structure to support the plate and an air gun. The two systems are decoupled to ensure possible future installation of different excitation systems (such as a pendulum) and, consequently, ensure higher flexibility.

8.1 Resonant Plate Structure

The structure serves primarily to support the plate. Indeed, in addition to the space constraints imposed by the laboratory dimensions, the main requirement concerns the structural resistance during shock tests. The design choices have also been made to facilitate the calibration and assembly of the plate as much as possible, with an easy access for an operator to mount the test object and sensors. For these reasons, it was decided to utilize a resonant plate suspended by chains or cables to simulate the free-free conditions of the plate as accurately as possible, arranged vertically and excited out-of-plane (OOP).

8.1.1 Structural Loads

Before presenting the final portal frame design, a brief overview of the calculations for defining the loads based on the extreme operating conditions is provided. For this purpose, two plates were considered as borderline cases in terms of dimensions. The two types of plates considered are an aluminum alloy plate with dimensions of $0.5 \times 0.5 \times 0.02$ m^3 and a mass of approximately 15 kg, and a steel plate with dimensions of $2 \times 1 \times 0.05$ m^3 and a mass of approximately 800 kg.

Since the plates are suspended from the structure using chains or ropes, the mechanical system can be modeled as a pendulum, with its initial conditions defined by the generated impact. Figure 66 depicts a simple representation of a generic

plate left free to oscillate after an impulsive excitation. The geometric parameters a and L represent, respectively, the distance from the center of gravity of the plate and the impact point to the hinge O around which the oscillation occurs.

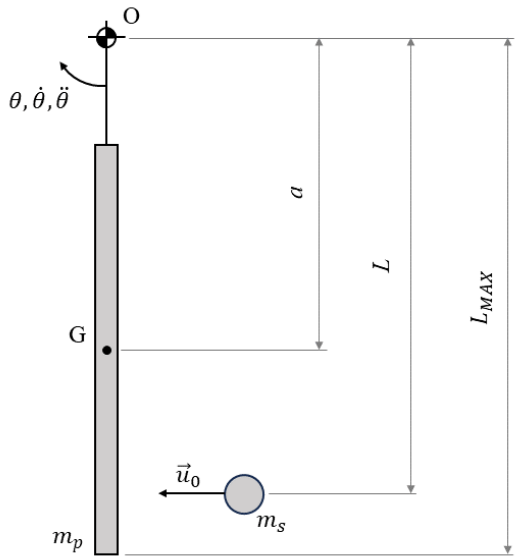

Figure 66. Diagram of a generic resonant plate left free to oscillate as it is suspended from hinge O.

The requirements expressed in terms of the projectile momentum are translated into initial conditions of the hanging plate, considering a perfectly elastic collision. Therefore, the angular velocity of the plate $\dot{\theta}_1$ and the projectile velocity u_1 right after the impact can be calculated by applying the conservation of energy and angular momentum:

$$\begin{cases} \frac{1}{2} m_s u_0^2 = \frac{1}{2} I_0 \dot{\theta}_1^2 + \frac{1}{2} m_s u_1^2 \\ m_s u_0 L = I_0 \dot{\theta}_1 - m_s u_1 L \end{cases} \tag{38}$$

where m_s represents the projectile mass, u_0 and u_1 are respectively the velocity of the projectile right before and after the impact, $I_0 = I_G + m_p a^2$ is the moment of inertia of the plate with respect to the hinge O, considering the barycentric moment of inertia I_G and its mass m_p. The initial conditions of the oscillating plate may be calculated as:

$$\begin{cases} u_1 = \dfrac{I_0 - m_s L^2}{I_0 + m_s L^2} u_0 \\ \dot{\theta}_1 = \dfrac{2 m_s L}{I_0 + m_s L^2} u_0 \end{cases} \tag{39}$$

The plate is considered to be in equilibrium before impact and, therefore, the initial angular position is set equal to $\theta_1 = 0$ rad.

In specific conditions, such as when a plate with reduced masses and dimensions is excited by significant impulsive forces, the plate may oscillate with large angular displacements. To limit the maximum oscillation of the plate, additional connections of the plate to the supporting structure can be contemplated using ropes, springs, or shock absorbers. For this reason, the dynamic model of the plate could be generalized by including a connection with generic tension springs with an equivalent stiffness k_{eq}, as shown in Figure 67. The definition of the stiffness k_{eq} allows for describing different applicable operating conditions.

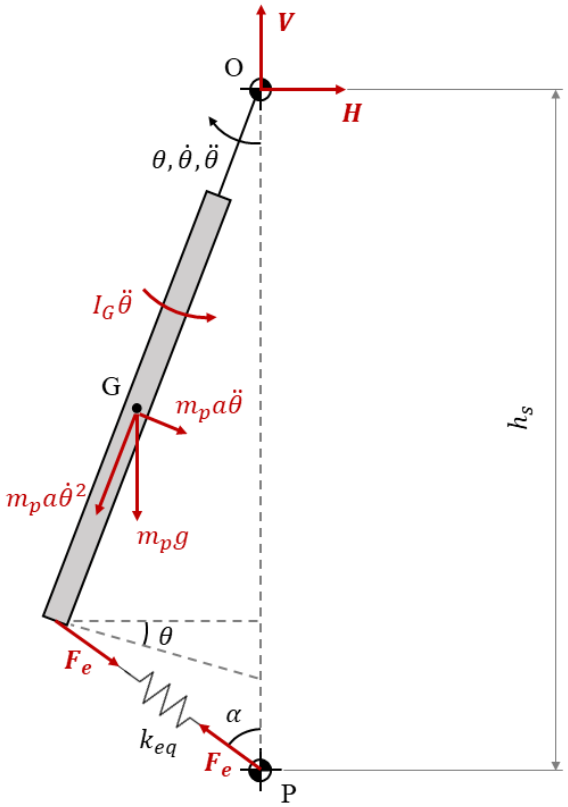

Figure 67. Free body diagram of a generic oscillating plate.

The equations that define the mechanical equilibrium of vertical and horizontal forces and moments with respect to O can be written as:

$$\begin{cases} V - m_p g - m_p a\ddot{\theta}\sin\theta - m_p a\dot{\theta}^2\cos\theta - F_e\cos\alpha = 0 \\ H + m_p a\ddot{\theta}\cos\theta - m_p a\dot{\theta}^2\sin\theta + F_e\sin\alpha = 0 \\ I_0\ddot{\theta} + Mga\sin\theta + F_e\cos(\alpha+\theta)\,L = 0 \end{cases} \tag{40}$$

Where the restoring force $F_e = k_{eq}(x(\theta) - x_0)$ is defined by using the equivalent stiffness k_{eq}, and the elongation of the generic spring is interpreted as the difference between $x(\theta)$ and the relaxed length x_0. When adopting pre-loaded springs or tensioned ropes was necessary, it would be enough to consider $x(0°) > x_0$ in the computation of the force F_e. Furthermore, by defining L_{MAX} as the farthest point from the hinge O to hit the plate (and also the point at which the equivalent spring is hinged) and h_s as the total height of the portal frame supporting the plate (crossbeam-base distance), then it is possible to determine $x(\theta)$ with the following geometric relationship (law of cosines):

$$x(\theta) = \sqrt{L_{MAX}^2 + h_s^2 - 2L_{MAX}h_s\cos\theta} \tag{41}$$

Finally, the angle α, which is the angle necessary to describe the direction of application of the force F_e, is defined by exploiting the geometry of the system (law of sines) and, therefore, as a function of the solely independent variable θ:

$$\alpha = \arcsin\left(\frac{L_{MAX}}{x(\theta)}\sin\theta\right) \tag{42}$$

Unable to adopt the small oscillation assumption, the equilibrium differential equations are numerically solved (e.g., explicit Runge-Kutta), and the values of the constraint reaction forces V and H applied at hinge O are determined. For instance, Figure 68 illustrates the numerical solutions obtained in an experimental condition with a steel plate of dimensions 2×1×0.05 m^3 and mass approximately 800 kg. By hitting the plate at its center of mass located at $a = L = 1.5$ m from the hinge O with a projectile of mass $m_s = 1$ kg and velocity $u_s = 80$ m/s and leaving it free to oscillate ($k_{eq} = 0$ N/m), it is observed that the maximum excursions of the plate

oscillations fall within about $\theta_{MAX} < 3°$, and the constraint reactions reach maximum values of approximately $V \approx 7800$ N and $H \approx 350$ N.

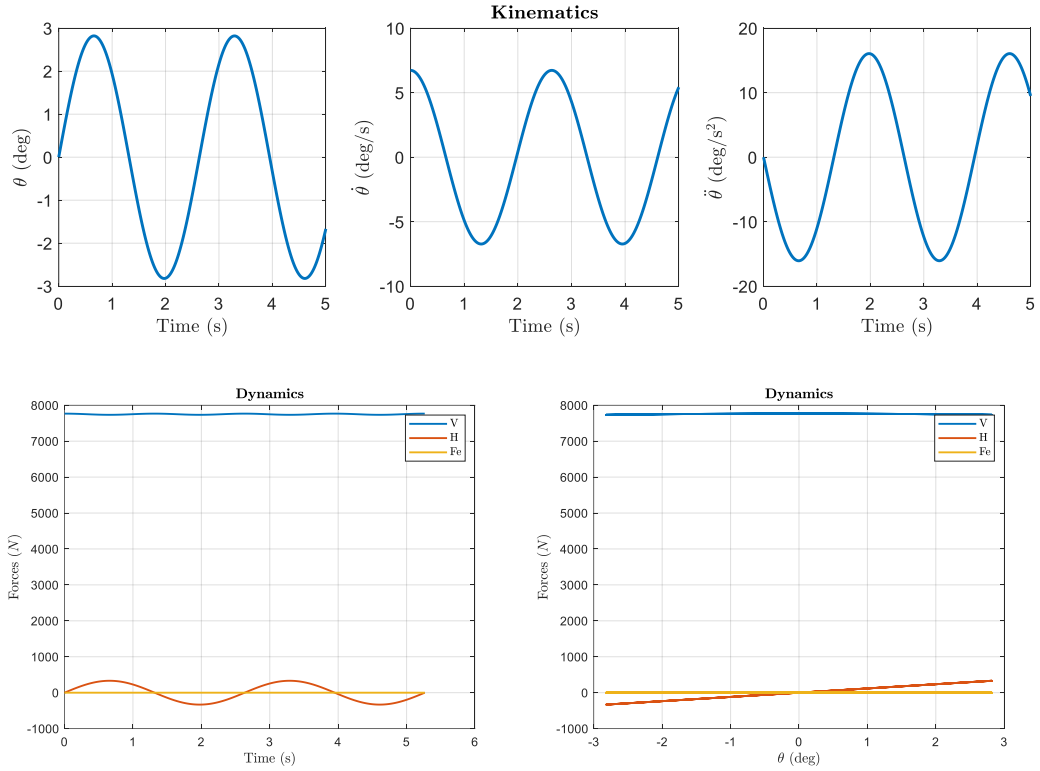

Figure 68. Numerical solutions regarding the dynamics of the borderline steel plate caused by the impact of the projectile. Specifically, the top graph illustrates the kinematic solutions. The other two graphs below depict the behavior of the constraint reaction forces in the time domain (on the left) and in the angular position domain (on the right).

This load distribution on the structure and the resulting reduced oscillations, despite the high momentum of the projectile, strongly depend on the inertia of the plate. Indeed, although the extreme case of the aluminum plate generates much lower static loads compared to the steel plate, the use of springs, ropes, or shock absorbers would be necessary to limit the angular excursions of the oscillations. To reduce these excursions, it is necessary to include the action of the force F_e, through an equivalent stiffness k_{eq}. This leads to the reduction of the maximum oscillation θ_{MAX} and the reduction of the horizontal load H, but significantly affects the vertical load V. For example, considering the impact between a typical projectile with mass $m_s = 0.5$ kg and velocity $u_s = 80$ m/s and an aluminum plate with dimensions of approximately 0.5×0.5×0.02 m^3 and mass about 15 kg, if the impact occurs at the center of mass of the plate located at $a = L = 1.5$ m from the hinge O, a system

with an equivalent stiffness of $k_{eq} = 123$ N/mm is required to limit the maximum oscillation $\theta_{MAX} < 9°$. In this case, the dynamic loads acting on the structure are shown in Figure 69 and reach maximum values of approximately $V \approx 7000$ N, $H \approx 700$ N and $F_e \approx 7400$ N.

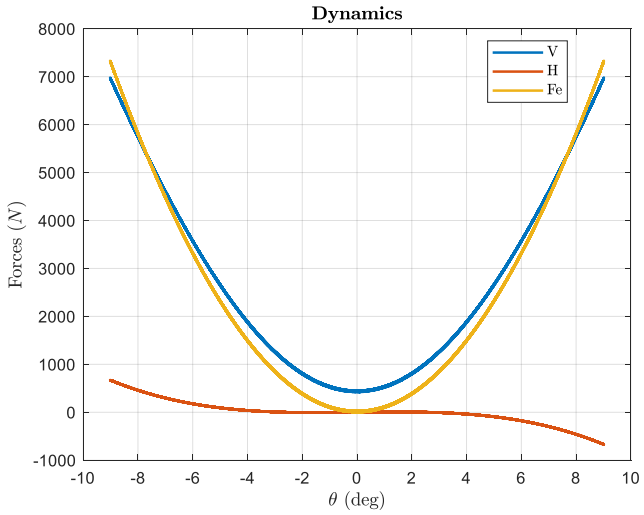

Figure 69. Trend of the constraint reaction forces as a function of the angular position of the plate in the borderline case employing a plate made of aluminum alloy.

Since ensuring maximum flexibility is desired and the feasible configurations would be too numerous to be fully analyzed, it was decided to apply a multiplicative correction coefficient for the simulated extreme cases, approximately $C_L \cong 2$ for V and F_e, and $C_L \cong 6$ for H to potentially consider cases with greater angular excursions of the plate. Thus, maximum reference loads were considered as $V = 15000$ N, $H = 4000$ N and $F_e = 15000$ N. These loads allow for tests with plates of significant mass, lightweight plates with wide oscillations, and plates constrained with rather rigid connections. Additionally, it is noted that the applied loads are dynamic rather than static, causing the structure to experience alternating fatigue. Therefore, as reported in [115], the admissible tension σ_{ams} was considered to be one-third of the material yield stress R_{p02}, ensuring a safety factor $SF > 3$. Generally, the structure may have been somewhat oversized for caution and to account for aspects that may have been overlooked in this analysis. However, it is possible to verify the feasibility of executing a considered critical test, given its specific operational characteristics.

8.1.2 Design Proposal

The different phases of the design process have led to the definition of the design shown in Figure 70. The portal frame has been entirely designed using standard steel section bars in structural steel S355 (ultimate tensile strength $R_m = 510$ MPa and yield strength $R_{p02} = 355$ MPa). Specifically, rectangular hollow section bars (UNI 7813) have been adopted for the bases and columns, and IPE/HEA beams with parallel flanges (UNI 5398 and UNI 5397) for the upper and lower crossbars. M20 threaded connections have been provided to join the different profiles together, and M20 chemical anchors to secure the structure to the laboratory floor. Some ribs welded in intervals have been arranged on the structure to increase its structural strength.

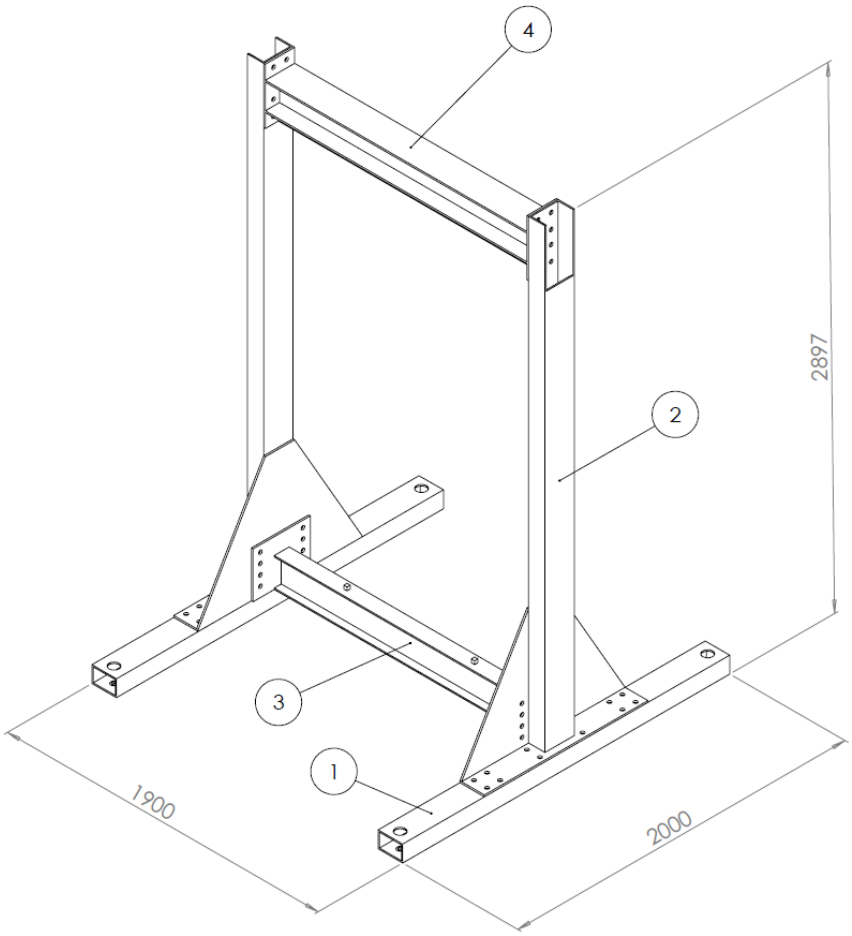

Figure 70. Isometric view of the portal frame designed to support the resonant plate composed of: (1) base rect.150x100, (2) column rect.180x100, (3) lower crossbar IPE180, and (4) upper crossbar HEA180 (dimensions in mm).

The structure provides a usable area for positioning plates up to maximum surface dimensions of 2×1 m^2, suspended by ropes or chains. The anchoring of these elements is made possible by a suitably perforated bar welded to the upper crossbar, illustrated in detail in Figure 71. The positioning of the plate can be adjusted by modifying the length and anchoring point of the chains themselves.

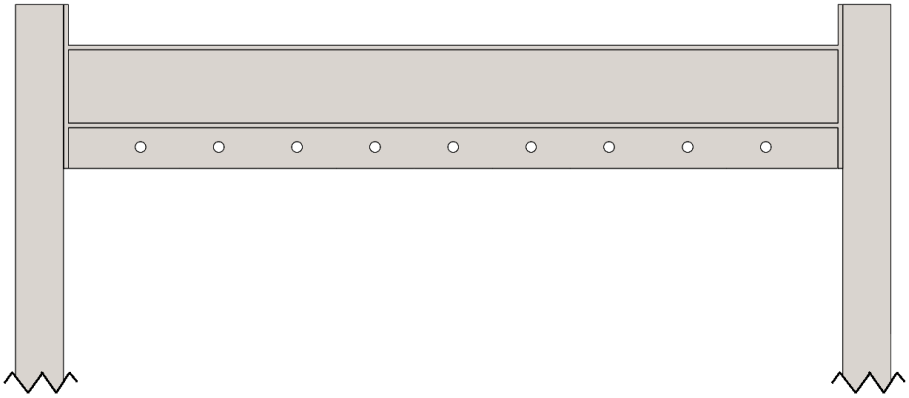

Figure 71. Detail of the perforated bar welded on the upper crossbar for mounting the resonant plate.

Table 16 lists the dimensions and the typology of each beam employed in the design, making reference to Figure 72 for the specific nomenclature. The total dimensions of the portal frame are approximately 2×2×3 m^3 and it is necessary to consider additional adjacent space to guarantee access to operators in the preparatory phases of the tests.

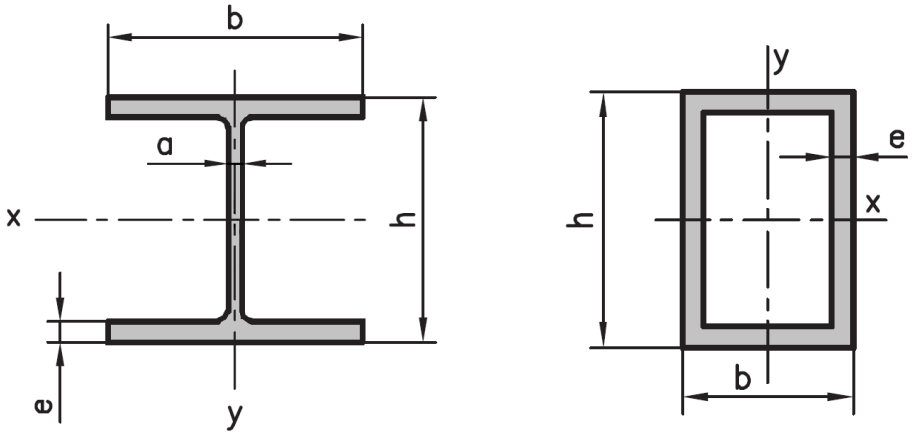

Figure 72. Nomenclature of the characteristic dimensions of the adopted section bars.

Table 16. Characteristic dimensions of the section bars adopted in the design.

	HEA180	**IPE180**	**Rect. 180×100**	**Rect. 150×100**
Marking	3	2	1	4
Length	1600 mm	1600 mm	2800 mm	2000 mm
h	171 mm	180 mm	180 mm	150 mm
b	180 mm	91 mm	100 mm	100 mm
e	9.5 mm	8 mm	8 mm	8 mm
a	6 mm	5.3 mm	-	-
$\mathbf{I_x}$	2510 cm^4	1317 cm^4	1598 cm^4	1008 cm^4
$\mathbf{I_y}$	925 cm^4	101 cm^4	638 cm^4	536 cm^4
$\mathbf{I_p}$	12 cm^4	12 cm^4	-	-

8.1.3 Structural Analysis

The structural design followed the guidelines of reference standards, such as the former CNR-UNI 10011 [116] and Eurocode 3 UNI EN 1993 [117,118]. These standards regulate the design, construction, testing, and maintenance of steel structures and their connections. The entire design process primarily focused on structural certification, verification of various connections (welded joints and threaded connections), and the bearing capacity check of the perforated bar on which the plate is suspended.

Structural analysis and reaction forces

The structural strength was verified both analytically, following the principles of structural mechanics, and numerically, through FEM analysis. In both cases, the loads V, H and F_e estimated in Subsection 8.1.1 were applied and distributed on two points, as shown in Figure 73. This approach aims to better reflect the operational conditions in which the plate will be suspended with at least two chains.

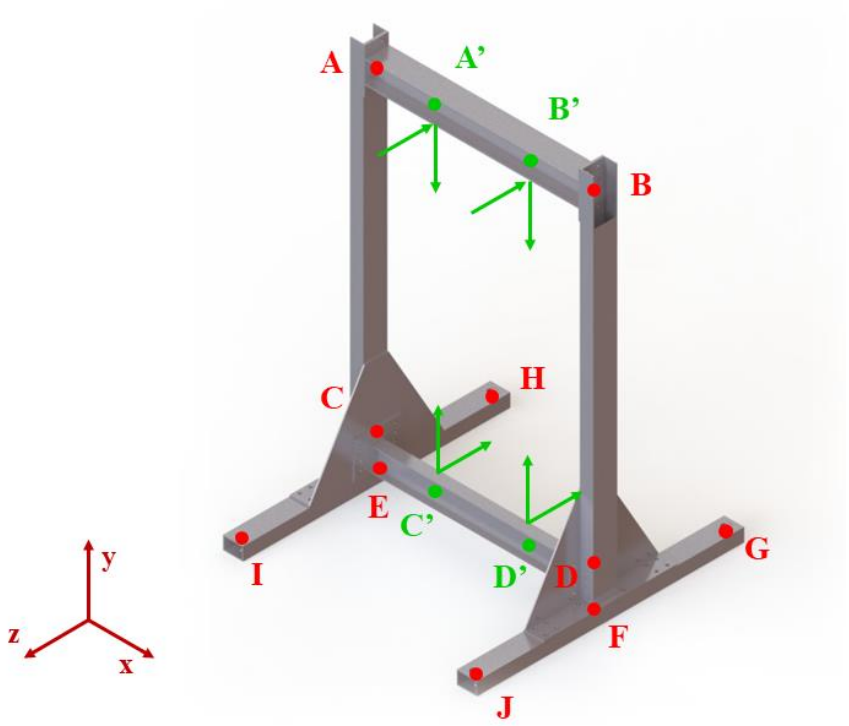

Figure 73. Definition of the reference system and connection points between the section bars.

Given these loading conditions, each element of the structure was modeled as a beam with its respective geometric and material characteristics. The connections between the beams were modeled as fixed joints, as a precautionary assumption. All critical sections were verified according to the von Mises criterion to ensure a safety factor $CS > 3$, as recommended in [115]. The analytical verification of the structure strength also allowed for the calculation of the reaction forces at each beam extremity, which is useful for subsequently verifying the size of the connections. Table 17 reports the obtained reaction forces. Table 18 presents the equivalent stresses obtained at the critical point, i.e., the most stressed point, of each beam. It can be observed that all safety factors meet the predetermined requirements. The reader can refer to Figure 73 for the nomenclature of the constraints and the identification of the global reference system.

Table 17. Absolute value of the reaction forces generated at each joint of the structure.

Joint	Reaction Force	Value	Joint	Reaction Force	Value
A, B	R_y	7780 N	**G, H**	R_x	990 N
	R_z	2000 N		R_y	3460 N
	M_x	500 Nm		R_z	1970 N
	M_y	800 Nm		M_x	1000 Nm
	M_z	3110 Nm		M_y	310 Nm
C, D	R_y	6980 N		M_z	130 Nm
	R_z	1940 N	**I, J**	R_x	990 N
	M_x	370 Nm		R_y	4560 N
	M_y	780 Nm		R_z	1970 N
	M_z	2890 Nm		M_x	1520 Nm
E, F	R_y	1620 N		M_y	310 Nm
	R_z	3940 N		M_z	130 Nm
	M_x	5260 Nm			
	M_y	1300 Nm			
	M_z	280 Nm			

Table 18. Summary of the structural verifications of each beam with identification of the critical point and the related equivalent tension values and Factor Of Safety (FOS).

Beam	Critical Section	σ_{VM}	FOS
HEA180	A, B	97 MPa	3.6
IPE180	C, D	56 MPa	6.4
Rect. 180×100	C, D	81 MPa	4.4
Rect. 150×100	E, F	24 MPa	14.9

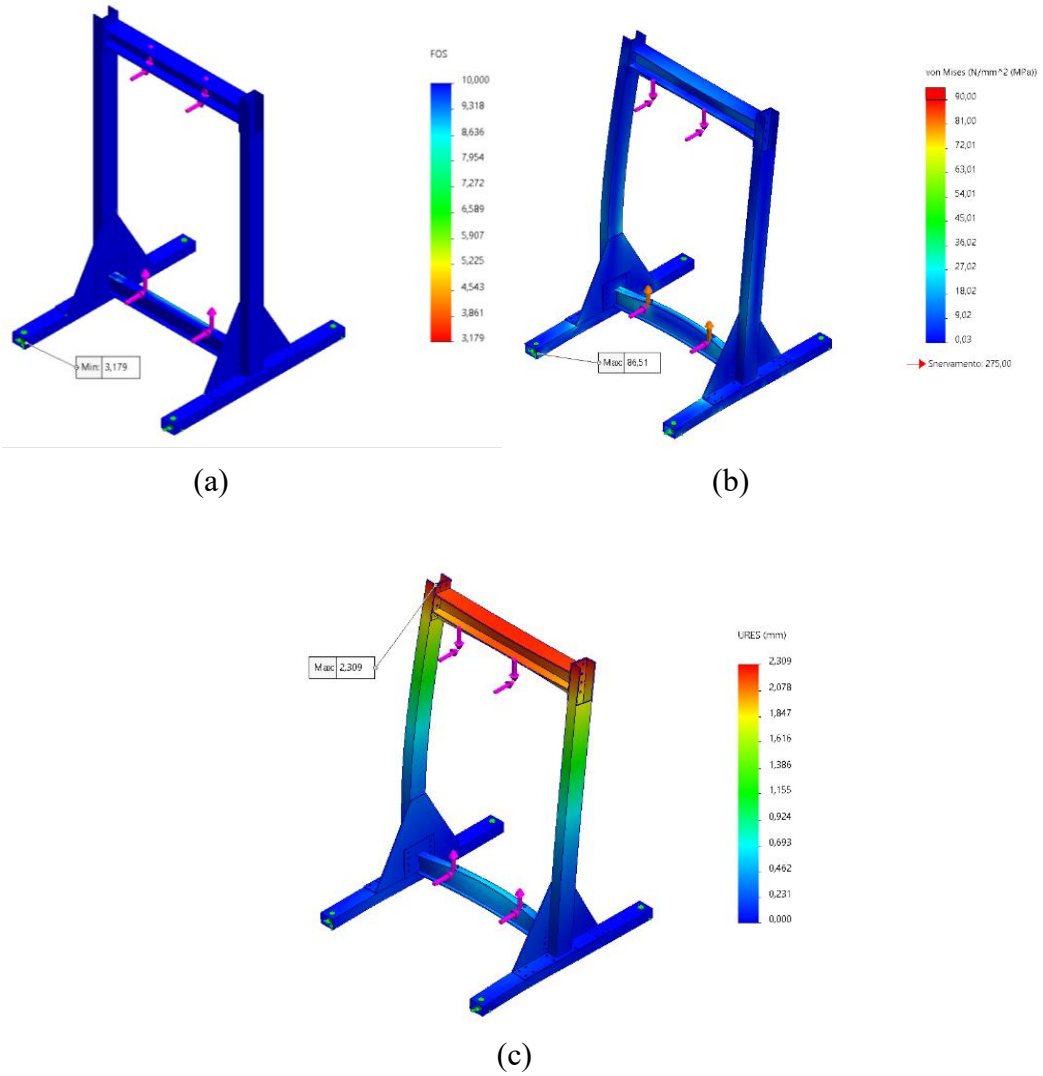

Figure 74. Results of the FEM structural analysis in terms of: (a) factor of safety; (b) equivalent stresses; (c) displacements.

In addition to this initial analytical verification, a further numerical check was conducted by setting up a FEM using the commercial software SolidWorks© 2022. Figure 74 depicts the analysis settings in the software and the numerical results obtained in terms of equivalent stresses, safety factors, and displacements. Once again, the structure was found to meet the criteria for $SF = 3$, satisfying the requirements in terms of allowable deformation. Indeed, the minimum FOS value equals 3.2 in correspondence with the hole prepared for fixing the chemical anchor. Therefore, the result could be particularly subject to the constraint conditions set in

the analysis. Regarding the displacements, the maximum value of just over 2 mm, considered acceptable, was obtained on the upper end of the column.

Welds verification

After verifying the structural strength of the section bars constituting the portal frame, the joints were checked, starting from the welds. The most critical weld is between the perforated bar and the upper beam (HEA 180). In addition to this, other welds were prepared to fix the connecting flanges to each beam and a double rib to reinforce the column at the base, where the bending moment stress is maximum. The verification was performed according to standards, thus deriving the minimum length of the welding bead. Indeed, according to EN1993-1-8, the strength of the weld must comply with both the following limitations:

$$\begin{cases} \sqrt{\sigma_{\perp}^2 + 3(\tau_{\perp}^2 + \tau_{\parallel}^2)} \leq \dfrac{f_u}{\beta_w \gamma_{M2}} \\ \sigma_{\perp}^2 \leq 0.9 \dfrac{f_u}{\gamma_{M2}} \end{cases} \tag{43}$$

where $\sigma_{\perp}$, $\tau_{\perp}$ and $\tau_{\parallel}$ are the normal and shear stresses parallel/perpendicular to the axis of the weld as shown in Figure 75, $f_u = 510$ MPa is the nominal ultimate tensile strength of the material, $\gamma_{M2} = 1.25$ is a safety factor, and $\beta_w = 0.9$ is an appropriate correlation factor dependent on the material.

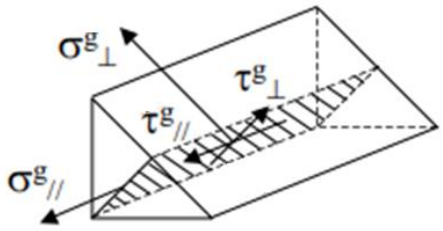

Figure 75. Definition of the stresses on the throat section of a fillet weld.

All weld fillets have been verified according to the required limitations. However, the minimum length required for the verification of the weld beads has been increased as a precaution, considering the impulsive nature of the loads and the possible simplifications adopted. At the same time, it was necessary to remain within reasonable values to avoid excessive distortions of the beam during the

welding process (which generates heat and therefore thermal stresses). For this reason as well, intermittent fillet welding has been provided.

Threaded connections verification

The typology of threaded connections shown in Figure 76 have been provided to connect the different elements of the portal frame. The threaded connections include anti-loosening washers and lock nuts to ensure correct operation even under dynamic load conditions.

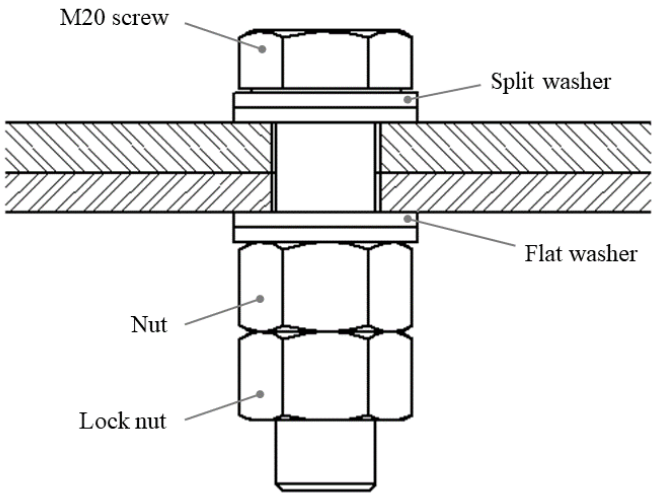

Figure 76. Section view of a bolted connection prepared with split washers and lock nuts to prevent loosening.

Although the analytical calculation of the forces and moments transmitted through the joints may be complex, making it difficult to determine the rotational stiffness of the connections, a straightforward but conservative way to verify bolted connections is to assume them as ideal fixed connections. Firstly, the position of the neutral axis was assumed at the center of the connection. In this manner, the maximum tensile force on the most stressed bolt was determined to verify the sizing of the M20 bolts according to regulations. Taking the connection between the HEA180 upper beam and one of the two uprights as an example, the reaction forces acting on the connection can be illustrated in Figure 77. By distributing the loads on each bolt, as shown in Figure 78, it was possible to identify the bolt subjected to the highest load, as well as the magnitude of this combined load. By combined load,

it is meant that all bolts are subjected to shear stresses and bending moments, which generate tensile stresses.

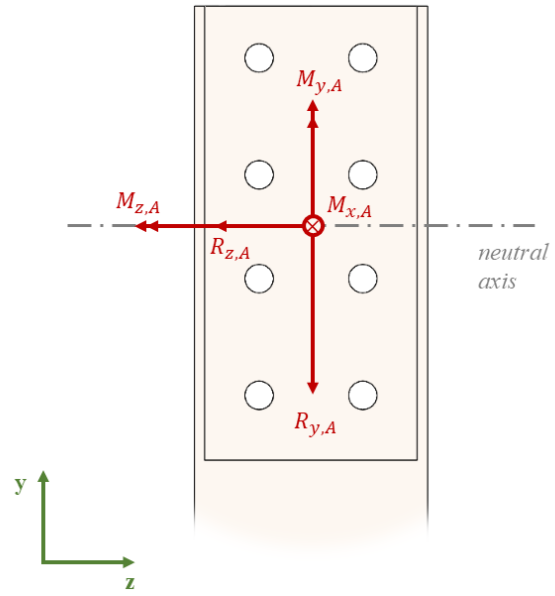

Figure 77. Loads generated on the connection between the upper crossbar and the column.

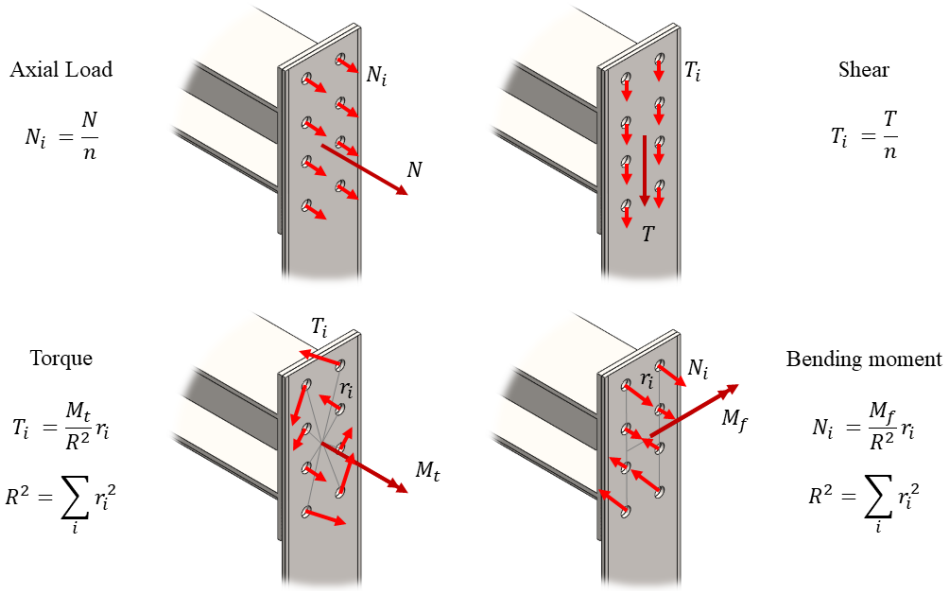

Figure 78. Distribution of loads on the bolts due to different stresses.

Since the bolts are subjected to shear and traction forces, a combined check of the two stresses present must be carried out. According to the regulations, it is performed by applying the following formula:

$$\frac{F_{v,Ed}}{F_{v,Rd}} + \frac{F_{t,Ed}}{1.4\,F_{t,Rd}} \leq 1 \tag{44}$$

where $F_{v,Ed}$ and $F_{t,Ed}$ are respectively the shear and traction forces on the bolt under project conditions, while $F_{v,Rd}$ and $F_{t,Rd}$ are respectively the shear and traction strength of the bolt, calculated as:

$$F_{v,Rd} = \frac{\alpha_v f_{ub} A_s}{\gamma_{M2}} \tag{45}$$

$$F_{t,Rd} = \frac{k_2 f_{ub} A_s}{\gamma_{M2}} \tag{46}$$

where $\alpha_v = 0.6$ is a coefficient dependent on the class 8.8 of the screw, $f_{ub} = 800$ MPa is the ultimate tensile strength of the material, $A_s = 245$ mm^2 is the area of the resistant section of the screw M20, $\gamma_{M2} = 1.25$ is the safety factor for bolts and, finally, $k_2 = 0.9$ is a coefficient established in the standard.

Bearing verification

Finally, the last verification concerns the bearing of the perforated bar for supporting the resonant plate. In case of abnormal operation, the pressure on the hole contour could lead to an increase in stresses at the contact surface between the bolt shank and the hole. Therefore, it is necessary to verify that the pressure generated by the force V on the contact area, assumed to be equal to the hole diameter D times the plate thickness t, is less than the allowable stress. This verification can be performed by adhering to the following condition:

$$\sigma_b = \frac{V}{tD} \leq \sigma_{b,ams} = \alpha \sigma_{ams} \tag{47}$$

where $\alpha = \min(\frac{a}{D}; 2.5)$ with $\frac{a}{D}$ equal to the ratio between the distance of the hole from the edge and the hole diameter. Alternatively, a more conservative

condition can be assumed, i.e. that the behavior of the connection with the chain is similar to a bolt inserted into a larger hole. The resistance can then be calculated following EN 1993-1-8 Table 3.4 as:

$$F_{b,Rd} = 0.8\frac{k_1 \alpha_b f_u D t}{\gamma_{M2}} \tag{48}$$

where $k_1 = 2.5$ and $\alpha_b = 0.67$ are coefficient defined in the standard, $D = 22$ mm is the hole diameter, $t = 20$ mm is the thickness of the bar, $f_u = 510$ MPa is the ultimate tensile strength, and $\gamma_{M2} = 1.25$ is a safety factor. In both cases, the bearing verification of the bar supporting the plate is valid.

Chemical anchors verification

Once the final design of the portal was reached, the assembly and fixation process to the laboratory floor was verified and envisaged through M20 chemical anchors. For the sizing of the chemical anchors, the most stressed one was considered, corresponding to points I and J in Figure 73. The resulting load can be divided into a tensile and a shear component, estimated about $R_n \approx 6$ kN, $R_t \approx 3$ kN. From commercial catalogs, such as the one proposed by Würth-Gruppe [119], it can be observed that an anchor with M20 threaded bars in zinc-coated steel class 8.8 can ensure an admissible tensile strength of $R_{n,ams} = 38.1$ kN and a shear strength of $R_{t,ams} = 67.2$ kN. In addition to this, further checks were necessary, such as the design tensile resistance for anchor pullout and the design tensile resistance for conical concrete breakage. The allowable values obtained mainly depend on the reference strength of the type of concrete, corrected by coefficients. These coefficients take into account the presence of other anchors placed nearby, rather than the anchoring depth. The correction of the admissible resistances with coefficients derived from the project conditions has enabled the validation of the combined shear/tensile strength verification for the selected chemical anchors.

8.2 Pneumatic Gun

This section aims to investigate a projectile launcher taking advantage of compressed air for pyroshock tests with resonant plates. This type of excitation may offer several advantages over other techniques as it could help avoid issues such as secondary impacts. The first part describes the model used to determine the velocity of the projectile right before the impact, while the second part focuses on the design

of the launcher structure to withstand the stresses generated during the projectile launch.

The design of the air cannon aims at launching a projectile with a mass up to 2 kg and a maximum velocity of 70 m/s. In addition to these requirements, the cannon must be capable of generating impacts at different points on the surface of the vertical metal plate, allowing for vertical excursions of approximately 1 m and a horizontal movement of about 0.5 m. Since the launcher must be installed in a specific laboratory, some dimensional limits are also imposed. Specifically, the maximum length is limited to 5 m, and the width is approximately 1 m, ensuring adequate space for operators to work on the test bench (test preparation, experimental setup calibration, and equipment assembly). The projectile, on the other hand, is assumed to be cylindrical with a diameter of 30-50 mm and with an interchangeable head to allow variation of parameters for calibration purposes.

To meet these requirements, the projectile velocity will be determined by studying the expansion of a compressed ideal gas in a chamber. Consequently, the main parameters considered in the analysis are the volume of the tank, the gas pressure, the dimensions of the cannon, and the dimensions of the projectile. After establishing the optimal parameters, the mechanical structure of the launcher is designed, and the structural integrity of each component is verified under the forces caused by the launch. Also in this case, the analyses are based on the guidelines of Eurocode 3 for the design of steel structures and FEM numerical simulations.

8.2.1 Exit Velocity Predictive Model

In this section, the entire system is modeled to understand the internal dynamics of the compressed air cannon and consequently predict the exit velocity of the projectile. This model, integrated with the prediction of dynamic loads and the simulation of the behavior of the resonant plate, allows for the accurate calibration of the pyroshock test bench. The automation of these processes and the precision of predictive models could lead to significant improvements in terms of reducing calibration times and costs.

The compressed air launcher system primarily consists of the components depicted in Figure 79: (1) a tank with a volume V_1 containing compressed air at pressure p_1; (2) a pneumatic or solenoid-activated valve with a flow section diameter d_v; (3) a barrel with internal diameter d and length L; and (4) a cylindrical projectile with diameter d equal to that of the barrel, length l, and mass m. The tubes

connecting all these components must ensure the necessary flow rate. This conceptualization of the launcher may include additional elements, such as a pre-chamber directly connected to the valve. This pre-chamber would eliminate the pressure loss due to the connecting tubes and would replace the tank in the simulation model.

By combining the equations that model each of the components constituting the launcher system, it is possible to estimate the projectile exit velocity given the design variables, such as the volume and pressure of the tank, the size and type of the valve, and the length of the barrel. In the literature, some studies show calculations related to the ballistics of an air cannon [120,121]. However, a specific model has been developed to simulate the designed system since the cited studies neglect some components.

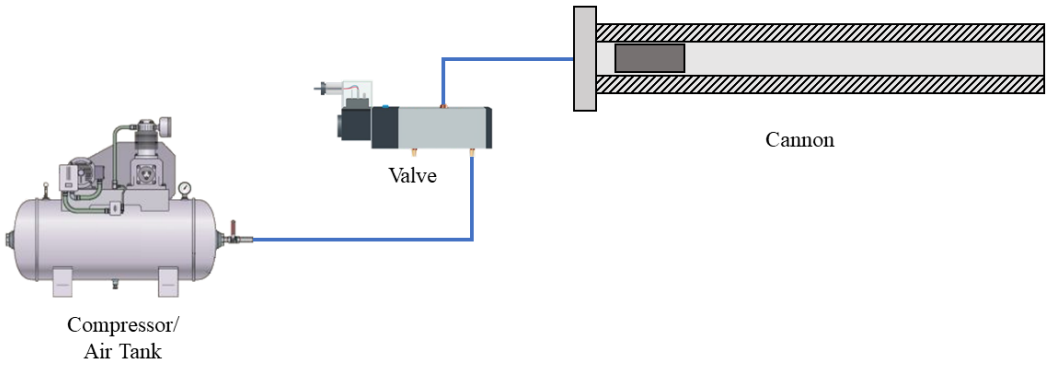

Figure 79. Scheme of the system constituting the launcher, mainly composed of a tank, a valve, and a cannon.

Starting from the dynamics of the projectile, its motion is regulated by the expansion of the gas inside the barrel. The expansion of pressurized gas inside the cannon thus generates a force on the projectile along the entire length L of the barrel, i.e., until the projectile exits the barrel itself. Since the open end of the barrel interfaces with the environment, the atmospheric pressure is acting on the other face of the projectile, negligible with calculations set in terms of relative pressures. The equation of motion of the projectile is therefore:

$$m_s \frac{d^2x}{dt^2} = Ap_2(t) - \mu_d m_s g \tag{49}$$

where $x(t)$ represents the position of the projectile along the barrel, $A = \frac{\pi d^2}{4}$ is the surface of the projectile face, $p_2(t)$ is the relative upstream pressure of the valve,

coincident with the internal pressure of the cannon, and finally μ_d is the dynamic friction coefficient. Initially, the friction between the projectile and the barrel can be neglected, especially if it is assumed that any leakage allows the projectile to behave like an aerostatic bearing [122]. Describing the internal dynamics of the cannon can be challenging due to the modeling of the expansion of the compressed gas. This expansion could be described as either adiabatic or isothermal. Assuming an initial isothermal expansion of air, considered a perfect diatomic gas, it is possible to derive the formula describing this expansion from the perfect gas law:

$$\frac{dp_2(t)}{dt}Ax(t) + \frac{dx(t)}{dt}Ap_2(t) = G(t)R^*T \tag{50}$$

where $G(t)$ is the mass flow rate of air regulated by the valve, R^* is the universal gas constant expressed in $\frac{J}{kg \cdot K}$, and T is the ambient temperature assumed to be equal to 20 °C. In particular, the mass flow rate of air depends on the valve characteristics, whose activation accelerates the projectile. A valve with a non-adjustable flow can be modeled as a nozzle, and its theoretical mass flow rate of air can be calculated according to ISO 6358 [123]. The formula for calculating the flow rate varies based on the ratio of downstream p_2 and upstream p_1 pressures of the valve. When the $\frac{p_2}{p_1} > b$, where b is the critical ratio, the efflux curve enters the sonic region, and the flow rate no longer increases. Defining K as:

$$K = 0.868 \cdot c_d \cdot \frac{\pi d_v^2}{4} \cdot \sqrt{\frac{293}{T^2 R}} \tag{51}$$

where T is the temperature upstream of the nozzle, equal to the ambient temperature (and, for the assumption of isothermal expansion, equal to the temperature downstream of the nozzle), and c_d is the conductance of the valve, experimentally determined. Then, the mass flow rates under sonic and subsonic conditions can be derived as follows:

$$\begin{cases} G(t) = K \cdot p_1(t) & if\ \frac{p_2}{p_1} \leq b \\ G(t) = K \cdot p_1(t) \cdot \sqrt{1 - \left(\frac{\frac{p_2}{p_1} - b}{1 - b}\right)^2} & if\ \frac{p_2}{p_1} > b \end{cases} \tag{52}$$

Finally, it is necessary to consider that the tank does not have infinite capacity and, therefore, cannot guarantee a constant flow rate. For this reason, starting again from the ideal gas law, there will be a decrease in pressure in the tank due to the flow rate $G(t)$ regulated by the following formula:

$$\frac{dp_1(t)}{dt} = -\frac{G(t) \cdot nR^*T}{V_1} = -\frac{G(t)}{C_t} \tag{53}$$

where n is the exponent of the polytropic process ($n = 1$ for an isothermal process, $n = 1.4$ in the case of an adiabatic process), and C_t represents the thermal capacity of the tank. To solve the differential equation system composed by Eqs. (49), (50), (52), and (53), a forward Euler numerical method has been applied. For the sake of completeness, the same system of equations discretized for the application of the aforementioned calculation method is written below:

$$\begin{cases} G(t_{i-1}) = K \cdot p_1(t_{i-1}) & if\ \frac{p_2(t_{i-1})}{p_1(t_{i-1})} \leq b \\ G(t_{i-1}) = K \cdot p_1(t_{i-1}) \cdot \sqrt{1 - \left(\frac{\frac{p_2(t_{i-1})}{p_1(t_{i-1})} - b}{1 - b}\right)^2} & if\ \frac{p_2(t_{i-1})}{p_1(t_{i-1})} > b \end{cases} \tag{54}$$

$$p_1(t_i) = p_1(t_{i-1}) - \frac{G(t_{i-1})}{C_t}\Delta t \tag{55}$$

$$p_2(t_i) = p_2(t_i) + \frac{G(t_{i-1})R^*T - p_2(t_{i-1})A\frac{x(t_i) - x(t_{i-1})}{\Delta t}}{Ax(t_{i-1})}\Delta t \tag{56}$$

$$x(t_{i+1}) = 2x(t_i) - x(t_{i-1}) + \frac{p_2(t_i)A}{m}\Delta t^2 \tag{57}$$

where t_i represents the i-th instant with $i > 1$, and $\Delta t = 1 \cdot 10^{-7}$ s the time step set for the application of the forward Euler method. To numerically solve these equations, it is necessary to define the following initial conditions: initial position of the projectile $x(t_0) \ll 1$ m (not exactly equal to 0, otherwise Eq. (56) would not be solvable with a zero denominator division); initial velocity of the projectile $u(t_0)$ =0 m/s; initial relative pressure of the tank $p_1(t_0)$, and initial relative pressure of the air in the barrel $p_2(t_0) = 0$ bar. At this point, it is possible to study the exit velocity of the projectile $u = \frac{dx}{dt}$ when the projectile has traveled a distance $x = L$, coincident with the length of the cannon. With this model, it is possible both to study how different design parameters influence the exit velocity of the projectile for an appropriate sizing of the system, and to predict the same velocity to adjust the tank pressure and calibrate the test bench during pyroshock tests.

Charts in Figure 80 show the velocity trends as the barrel length, and initial pressure of the tank vary. These curves were obtained by iterating simulations and varying one parameter at a time to understand its influence on the final velocity. A cylindrical projectile with a diameter $d = 50$ mm, length $l = 200$ mm made of aluminum was assumed, thus having a mass $m_s \approx 1$ kg.

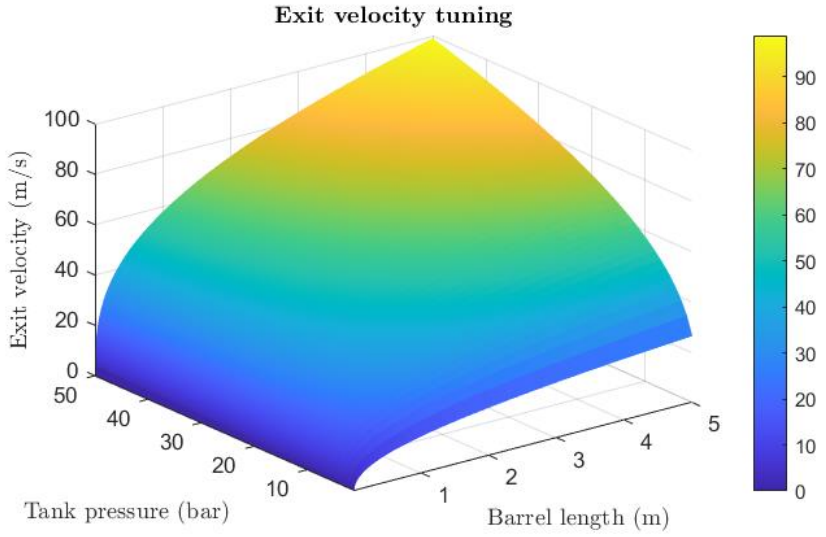

Figure 80. Trend of the exit velocity of the projectile as a function of the initial pressure of the tank and the barrel length.

Based on the results obtained from this analysis, with a simple pressure tank excluded from compliance for commissioning and utilization (for example, initial pressure and initial volume of the tank equal to $p_1 = 12$ bar and $V_1 = 50$ l, respectively), it is conceivable to achieve an exit velocity $v \approx 60$ m/s with a barrel length $L = 4$ m. Figure 81 depicts the trend of the velocity estimated by the numerical model under the specified conditions. It is worth noting that the increase in velocity due to the barrel length becomes less significant for higher length values. This is also the reason why a barrel length of $L = 4$ m was chosen.

If the accuracy of the model will prove inadequate for the application, some aspects, previously neglected, could be included in the analysis, such as potential leaks, pressure drops, and friction. Additionally, alternative thermodynamic transformations could be evaluated, such as replacing isothermal transformations with adiabatic ones.

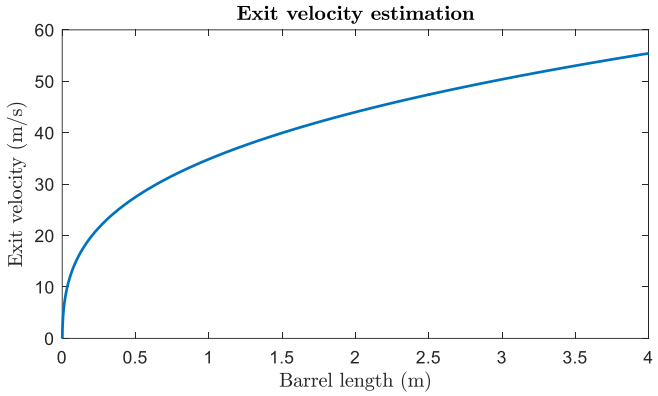

Figure 81. Exit velocity trend with respect to the barrel length.

8.2.2 Design Proposal

Thanks to the estimation of the exit velocity of the projectile, it was possible to define the excitation system of the resonant plate as composed of a 50-liter compressed air tank at 12 bar, connected to the barrel with a removable cover to facilitate reloading in multiple launch tests. As depicted in Figure 82, a 3-way, 2-position valve is interposed between the tank and the barrel to regulate the air flow. In addition to accelerating the projectile, this valve must allow the barrel to be discharged once the projectile has exited (approximately at the time of impact). This is achievable with a valve that connects the barrel to the environment when normally closed and connects the tank to the barrel when activated (pneumatically or electrically). The valve can be activated through a system controlled by a pair of photocells that

detect the passage of the projectile near the barrel exit. This process prevents the projectile from oscillating around the end of the barrel and generating multiple impacts on the plate. Additionally, the photocells allow the projectile exit velocity to be determined.

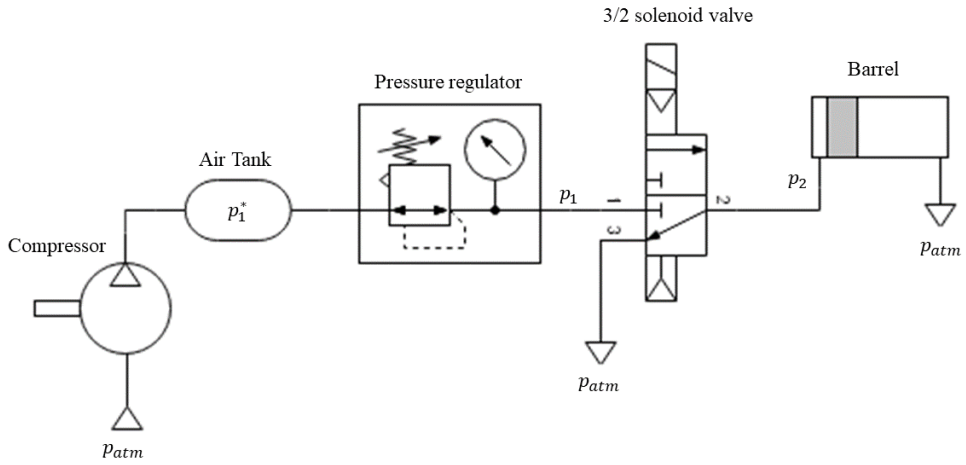

Figure 82. Pneumatic scheme foreseen for the pneumatic gun launcher.

Figure 83 illustrates the conceptualization of the barrel system with its corresponding support structure. The structure supporting the barrel was initially designed with equidistant vertical supports to ensure the most linear possible path for the projectile. The barrel, with an inner diameter of 50 mm and a wall thickness of 2.5 mm, is made of seamless steel tubes regulated by the ISO EN 10305-4 [124] standard. These tubes, manufactured without welding and cold drawn, are specifically designed for hydraulic and pneumatic systems, offering low roughness values and precise tolerances on diameter and straightness. The barrel is connected to the vertical supports via semi-circular clamps, allowing for interchangeability and providing the flexibility required for pyroshock tests. The vertical supports are L-shaped brackets made of 10 mm thick steel sheet, reinforced with ribs for increased lateral rigidity. Each support provides holes for discrete height adjustment of the barrel and, consequently, the impact application position. The base of the brackets is designed to couple with the lower part of the structure and allow lateral movement of the barrel using linear guides. Alternatively, this design of vertical supports can be replaced with pantograph lifting platforms. With its interconnected arms, this system would allow continuous lifting of the barrel, enabling better adjustment of the force application position.

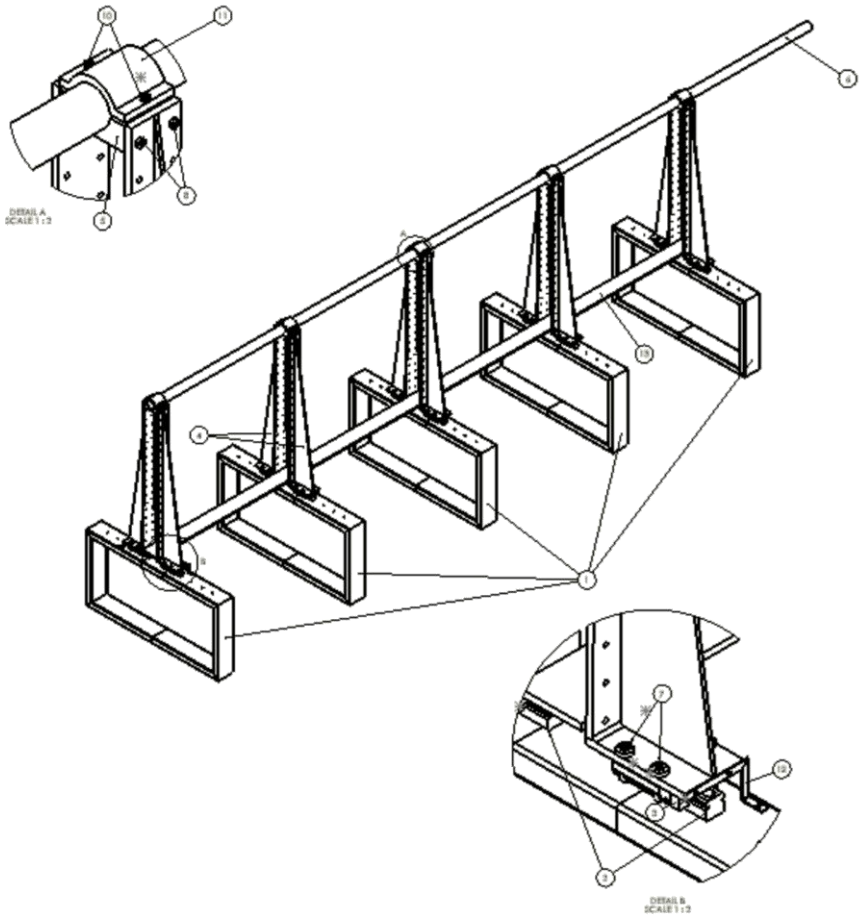

Figure 83. Design of the structure constituting the launcher.

In addition to the barrel weight, the structure is subjected to the force exerted by the expanding gas during the projectile launch. To conservatively verify the structure, the maximum pressure achievable in the barrel has been assumed to be equal to the maximum pressure reachable in the tank, $p_2 = 12$ bar. The maximum force that can be generated is therefore equal to the pressure that the expanding gas applies to the closed end of the barrel, with an area $A = \frac{\pi D^2}{4} = 1963$ mm^2. Consequently, the force that the barrel horizontally exerts on the supports can be estimated as $F = Ap_2 = 2160$ N. The entire structure has been verified again following the guidelines outlined in Eurocode 3 [117,118], concerning the design of steel structures. Specifically, the barrel was first verified in terms of guaranteed straightness and resistance to internal pressure. Subsequently, all components of the support structure and their respective connections (threaded and welded) were verified.

The current state of the experimental test bench design for pyroshock testing has reached a sufficient level of development to realize experimental tests. However, this part of the work foresees further future developments and applicable improvements. Once the entire experimental setup is realized, it will be possible to characterize the actual installed components, deriving, for example, the specific values of c_d and b related to the pneumatic valve. Therefore, measuring the actual projectile exit velocities will allow validating or correcting the developed model, as well as enabling appropriate design of the pressure control system. The final experimental system envisages complete integration of the developed numerical models for the setup and calibration of the test bench and the control of all involved parameters.

Chapter 9

Conclusions

This PhD thesis aims to advance the field of pyroshock tests by filling the gaps in both numerical and experimental simulations. The novel contributions of the present work may be grouped into four macro-categories: (1) numerical models for simulating pyroshock tests and (2) for optimizing the design of pyroshock test facilities; (3) investigation of impact tests thanks to the collection of a comprehensive experimental dataset; and (4) the proposal of a test bench for experimental pyroshock simulation.

The developed numerical models, operating in the frequency domain, have demonstrated promising results in accurately predicting experimental SRS. Their computational efficiency allows for rapid adjustments of test parameters, thereby reducing downtime and costs associated with experimental setup. Emphasis on facing the inverse problem alongside the development of simulation models for pyroshock tests involving resonant plates represent significant advancements in the field. This progress offers practical solutions for the design, calibration, and optimization of test benches, enhancing efficiency and effectiveness in pyroshock testing procedures.

9.1 Conclusions

In summary, the main objectives and original contributions of this doctoral thesis have been faced independently in each chapter.

After an initial overview of pyroshock tests, Chapter 3 presented a systematic analysis of the literature to identify key studies on experimental and numerical simulations of pyroshock in aerospace applications. This comprehensive review highlights existing gaps and sets the stage for the thesis objectives. The same systematic review integrated the narrative reviews present in the literature, providing a detailed analysis of the current state of the art.

A novel semi-analytical approach to describe pyroshock tests entirely in the frequency domain was proposed in Chapter 4, while Chapter 5 presented the numerical models developed for the simulation of pyroshock tests. In general, these models provided novel solutions to simulate the SRS acceleration of the resonant plate with a high degree of precision without requiring considerable computational effort. Their prompt calculation times and flexibility led to on-demand applications consisting in the tuning of the test facility as the requirements of each test may vary. This translates to a noteworthy reduction in downtime and costs for setting up the experimental system.

Chapter 6 presented an in-depth analysis germane to the design and optimization of the experimental setup, which could be considered as the inverse problem addressed by the pyroshock simulation methods. In particular, techniques to optimize the plate design, its shape and dimensions, and the measurement-impact positions are presented. Given the complexity of a pyroshock test facility, the results obtained in this chapter showed improvements in the SRS accuracy, providing the configuration that better meets the requirements.

A large dataset fully exploring shock tests with a resonant plate was described in Chapter 7. Data were acquired on an operating pyroshock test bench located at the sound and vibration research laboratory of the KTH Royal Institute of Technology. This dataset allowed the investigation on the influence of the experimental configurations, a further and general validation of the predictive model, and an in-depth analysis of the contact mechanics inherent to the shock tests.

Finally, the acquired knowledge and the proposed models led to the design of a test bench to perform pyroshock tests at Politecnico di Torino, described in Chapter 8. The project mainly includes a structure to support the resonant plate and a pneumatic gun to launch projectiles. The combination of these systems could allow an easy adjustment of the numerous parameters involved in the impact mechanics.

9.2 Future Perspectives

The potential advancements in the field of pyroshock test simulation are so extensive that the current state of research represents an early stage of its development. The existing literature highlights several gaps that pose challenges for future research. Some of these have been addressed in this thesis, trying to propose new solutions. Despite the advances obtained, certain aspects presented require further investigation.

In particular, despite significant progress in simulation methods, there remains room for improvement in certain areas to enhance result accuracy. One such area is the definition of the impulse, which deserves more detailed exploration to characterize the physical phenomenon with greater precision. Errors in the impulse definition phase can have a substantial impact on the overall accuracy of the model, as proved by the analysis of the dataset presented in this thesis.

Therefore, future research efforts could focus on refining the estimation of parameters for impulse definition and conducting new acquisitions using different excitation techniques for the resonant plate, such as the pneumatic gun designed for the proposed test bench. This approach would provide valuable insights and contribute to advancing the state of the art in pyroshock test simulation.

Another area of interest is the damping coefficient utilized in the frequency analysis of the resonant plate. Currently, this coefficient is typically assumed to be constant across frequencies and derived from material properties available in the literature. However, a more detailed understanding of how damping varies with frequency could enhance the accuracy of simulations.

Additionally, the analytical definition of stiffness within the MDOF model deserves careful examination. At the moment, stiffness values are often determined through tuning with an equivalent FEM model. While effective, this approach somewhat diminishes the advantages and flexibility inherent in the MDOF model. Exploring alternative methods for analytically defining stiffness could lead to more robust and efficient simulations.

Many advancements can be sought on the experimental front. In fact, the implementation of the test rig could lead to a deeper understanding of the physics behind pyroshock tests and potentially study corrections and improvements to the experimental setup. The tests themselves will be beneficial to further investigate

the impact mechanics, and the system behavior, as well as validate or provide insights for improving current predictive models.

Looking ahead to the future, one of the long-term goals is to establish a comprehensive framework for pyroshock tests, aiming to define a standardized approach for simulating pyroshocks. This framework would encompass both optimal experimental test bench setups and reliable, efficient numerical simulation models. Such advancements would enable aerospace equipment to undergo qualification rapidly and with a high degree of precision.

By standardizing the testing process, reducing both time and costs, and enhancing performance, the aerospace sector might benefit significantly. Accelerating the development of aerospace technologies would not only drive innovation but also produce economic advantages for industries associated with this sector.

Further developments concern calibration techniques for the test rig. For the sake of completeness, it would be interesting to investigate even more the dynamics of the resonant plate, including the analysis of potential non-isotropic properties. For instance, including the adoption of local stiffeners or ribs to compensate for the presence of the test object could be effective.

Lastly, acquiring real measurements from pyroshock tests could lead to understanding whether the SRS reliably represents reality with sufficient precision. If this is not the case, potential development could involve the exploration and definition of a novel substituting method for calculating shock effects.

Appendix A

Dataset Description

This Appendix fully reports the parameters combinations per each test and the associated filename. It is worth noting that the run order does not totally match the standard order used to name the files. Indeed, the tests have been partially randomized to reduce the effects associated with time-dependent variables, potentially affecting the test results. Filenames consist of the first three digits of the standard order identification number followed by an underscore. The following part corresponds to the typical file logging generated by the NI FlexLogger software, in which the acquisition date-time is inserted. For example, the file named "001_LogFile_2023-03-02-15-33-14.tdms" refers to the test identified with standard order #1 and was acquired on 15/02/2023 at 15.33. The reference conditions can be obtained from Table A1. All experimental files have TDMS extension, a standard used by National Instruments which contains both raw data and metadata. These files can be opened with special software or converted into alternative formats (for instance, they have been converted into MAT files in the present work).

An automatic data quality check was performed to verify the acquisition validity and exclude any accidental errors. In particular, the following conditions were verified:

- Correct acquisition of all channels for each test (no overload, no corrupted data, channel synchronism, acquisition duration);
- Recording of 10 impulses per file at regular intervals of about 6 seconds;
- Lack of double-peaked pulses (i.e., force profiles with multiple peaks) due to the impact of the excited plate on the hammer.

Table A1. File names and related configurations.

Standard order (Filename)	Impact Position	Hammer Speed	Hammer Tip	Anvil Plate	Anvil Insulator	Boundary Conditions
1	#1	Low	Aluminium	None	None	Free
2	#2	Low	Aluminium	None	None	Free
3	#3	Low	Aluminium	None	None	Free
4	#1	High	Aluminium	None	None	Free
5	#2	High	Aluminium	None	None	Free
6	#3	High	Aluminium	None	None	Free
7	#1	Low	Delrin	None	None	Free
8	#2	Low	Delrin	None	None	Free
9	#3	Low	Delrin	None	None	Free
10	#1	High	Delrin	None	None	Free
11	#2	High	Delrin	None	None	Free
12	#3	High	Delrin	None	None	Free
13	#1	Low	Polyurethane	None	None	Free
14	#2	Low	Polyurethane	None	None	Free
15	#3	Low	Polyurethane	None	None	Free
16	#1	High	Polyurethane	None	None	Free
17	#2	High	Polyurethane	None	None	Free
18	#3	High	Polyurethane	None	None	Free
19	#1	Low	Aluminium	Aluminium	None	Free
20	#2	Low	Aluminium	Aluminium	None	Free
21	#3	Low	Aluminium	Aluminium	None	Free

Standard order (Filename)	Impact Position	Hammer Speed	Hammer Tip	Anvil Plate	Anvil Insulator	Boundary Conditions
22	#1	High	Aluminium	Aluminium	None	Free
23	#2	High	Aluminium	Aluminium	None	Free
24	#3	High	Aluminium	Aluminium	None	Free
25	#1	Low	Delrin	Aluminium	None	Free
26	#2	Low	Delrin	Aluminium	None	Free
27	#3	Low	Delrin	Aluminium	None	Free
28	#1	High	Delrin	Aluminium	None	Free
29	#2	High	Delrin	Aluminium	None	Free
30	#3	High	Delrin	Aluminium	None	Free
31	#1	Low	Polyurethane	Aluminium	None	Free
32	#2	Low	Polyurethane	Aluminium	None	Free
33	#3	Low	Polyurethane	Aluminium	None	Free
34	#1	High	Polyurethane	Aluminium	None	Free
35	#2	High	Polyurethane	Aluminium	None	Free
36	#3	High	Polyurethane	Aluminium	None	Free
37	#1	Low	Aluminium	Steel	None	Free
38	#2	Low	Aluminium	Steel	None	Free
39	#3	Low	Aluminium	Steel	None	Free
40	#1	High	Aluminium	Steel	None	Free
41	#2	High	Aluminium	Steel	None	Free
42	#3	High	Aluminium	Steel	None	Free
43	#1	Low	Delrin	Steel	None	Free
44	#2	Low	Delrin	Steel	None	Free
45	#3	Low	Delrin	Steel	None	Free
46	#1	High	Delrin	Steel	None	Free
47	#2	High	Delrin	Steel	None	Free
48	#3	High	Delrin	Steel	None	Free
49	#1	Low	Polyurethane	Steel	None	Free
50	#2	Low	Polyurethane	Steel	None	Free

Standard order (Filename)	Impact Position	Hammer Speed	Hammer Tip	Anvil Plate	Anvil Insulator	Boundary Conditions
51	#3	Low	Polyurethane	Steel	None	Free
52	#1	High	Polyurethane	Steel	None	Free
53	#2	High	Polyurethane	Steel	None	Free
54	#3	High	Polyurethane	Steel	None	Free
55	#1	Low	Aluminium	Aluminium	Polymeric	Free
56	#2	Low	Aluminium	Aluminium	Polymeric	Free
57	#3	Low	Aluminium	Aluminium	Polymeric	Free
58	#1	High	Aluminium	Aluminium	Polymeric	Free
59	#2	High	Aluminium	Aluminium	Polymeric	Free
60	#3	High	Aluminium	Aluminium	Polymeric	Free
61	#1	Low	Delrin	Aluminium	Polymeric	Free
62	#2	Low	Delrin	Aluminium	Polymeric	Free
63	#3	Low	Delrin	Aluminium	Polymeric	Free
64	#1	High	Delrin	Aluminium	Polymeric	Free
65	#2	High	Delrin	Aluminium	Polymeric	Free
66	#3	High	Delrin	Aluminium	Polymeric	Free
67	#1	Low	Polyurethane	Aluminium	Polymeric	Free
68	#2	Low	Polyurethane	Aluminium	Polymeric	Free
69	#3	Low	Polyurethane	Aluminium	Polymeric	Free
70	#1	High	Polyurethane	Aluminium	Polymeric	Free
71	#2	High	Polyurethane	Aluminium	Polymeric	Free
72	#3	High	Polyurethane	Aluminium	Polymeric	Free
73	#1	Low	Aluminium	Steel	Polymeric	Free
74	#2	Low	Aluminium	Steel	Polymeric	Free
75	#3	Low	Aluminium	Steel	Polymeric	Free
76	#1	High	Aluminium	Steel	Polymeric	Free
77	#2	High	Aluminium	Steel	Polymeric	Free
78	#3	High	Aluminium	Steel	Polymeric	Free
79	#1	Low	Delrin	Steel	Polymeric	Free

Standard order (Filename)	Impact Position	Hammer Speed	Hammer Tip	Anvil Plate	Anvil Insulator	Boundary Conditions
80	#2	Low	Delrin	Steel	Polymeric	Free
81	#3	Low	Delrin	Steel	Polymeric	Free
82	#1	High	Delrin	Steel	Polymeric	Free
83	#2	High	Delrin	Steel	Polymeric	Free
84	#3	High	Delrin	Steel	Polymeric	Free
85	#1	Low	Polyurethane	Steel	Polymeric	Free
86	#2	Low	Polyurethane	Steel	Polymeric	Free
87	#3	Low	Polyurethane	Steel	Polymeric	Free
88	#1	High	Polyurethane	Steel	Polymeric	Free
89	#2	High	Polyurethane	Steel	Polymeric	Free
90	#3	High	Polyurethane	Steel	Polymeric	Free
91	#1	Low	Aluminium	None	None	Fixed
92	#2	Low	Aluminium	None	None	Fixed
93	#3	Low	Aluminium	None	None	Fixed
94	#1	High	Aluminium	None	None	Fixed
95	#2	High	Aluminium	None	None	Fixed
96	#3	High	Aluminium	None	None	Fixed
97	#1	Low	Delrin	None	None	Fixed
98	#2	Low	Delrin	None	None	Fixed
99	#3	Low	Delrin	None	None	Fixed
100	#1	High	Delrin	None	None	Fixed
101	#2	High	Delrin	None	None	Fixed
102	#3	High	Delrin	None	None	Fixed
103	#1	Low	Polyurethane	None	None	Fixed
104	#2	Low	Polyurethane	None	None	Fixed
105	#3	Low	Polyurethane	None	None	Fixed
106	#1	High	Polyurethane	None	None	Fixed
107	#2	High	Polyurethane	None	None	Fixed
108	#3	High	Polyurethane	None	None	Fixed

Standard order (Filename)	Impact Position	Hammer Speed	Hammer Tip	Anvil Plate	Anvil Insulator	Boundary Conditions
109	#1	Low	Aluminium	Aluminium	None	Fixed
110	#2	Low	Aluminium	Aluminium	None	Fixed
111	#3	Low	Aluminium	Aluminium	None	Fixed
112	#1	High	Aluminium	Aluminium	None	Fixed
113	#2	High	Aluminium	Aluminium	None	Fixed
114	#3	High	Aluminium	Aluminium	None	Fixed
115	#1	Low	Delrin	Aluminium	None	Fixed
116	#2	Low	Delrin	Aluminium	None	Fixed
117	#3	Low	Delrin	Aluminium	None	Fixed
118	#1	High	Delrin	Aluminium	None	Fixed
119	#2	High	Delrin	Aluminium	None	Fixed
120	#3	High	Delrin	Aluminium	None	Fixed
121	#1	Low	Polyurethane	Aluminium	None	Fixed
122	#2	Low	Polyurethane	Aluminium	None	Fixed
123	#3	Low	Polyurethane	Aluminium	None	Fixed
124	#1	High	Polyurethane	Aluminium	None	Fixed
125	#2	High	Polyurethane	Aluminium	None	Fixed
126	#3	High	Polyurethane	Aluminium	None	Fixed
127	#1	Low	Aluminium	Steel	None	Fixed
128	#2	Low	Aluminium	Steel	None	Fixed
129	#3	Low	Aluminium	Steel	None	Fixed
130	#1	High	Aluminium	Steel	None	Fixed
131	#2	High	Aluminium	Steel	None	Fixed
132	#3	High	Aluminium	Steel	None	Fixed
133	#1	Low	Delrin	Steel	None	Fixed
134	#2	Low	Delrin	Steel	None	Fixed
135	#3	Low	Delrin	Steel	None	Fixed
136	#1	High	Delrin	Steel	None	Fixed
137	#2	High	Delrin	Steel	None	Fixed

Standard order (Filename)	Impact Position	Hammer Speed	Hammer Tip	Anvil Plate	Anvil Insulator	Boundary Conditions
138	#3	High	Delrin	Steel	None	Fixed
139	#1	Low	Polyurethane	Steel	None	Fixed
140	#2	Low	Polyurethane	Steel	None	Fixed
141	#3	Low	Polyurethane	Steel	None	Fixed
142	#1	High	Polyurethane	Steel	None	Fixed
143	#2	High	Polyurethane	Steel	None	Fixed
144	#3	High	Polyurethane	Steel	None	Fixed
145	#1	Low	Aluminium	Aluminium	Polymeric	Fixed
146	#2	Low	Aluminium	Aluminium	Polymeric	Fixed
147	#3	Low	Aluminium	Aluminium	Polymeric	Fixed
148	#1	High	Aluminium	Aluminium	Polymeric	Fixed
149	#2	High	Aluminium	Aluminium	Polymeric	Fixed
150	#3	High	Aluminium	Aluminium	Polymeric	Fixed
151	#1	Low	Delrin	Aluminium	Polymeric	Fixed
152	#2	Low	Delrin	Aluminium	Polymeric	Fixed
153	#3	Low	Delrin	Aluminium	Polymeric	Fixed
154	#1	High	Delrin	Aluminium	Polymeric	Fixed
155	#2	High	Delrin	Aluminium	Polymeric	Fixed
156	#3	High	Delrin	Aluminium	Polymeric	Fixed
157	#1	Low	Polyurethane	Aluminium	Polymeric	Fixed
158	#2	Low	Polyurethane	Aluminium	Polymeric	Fixed
159	#3	Low	Polyurethane	Aluminium	Polymeric	Fixed
160	#1	High	Polyurethane	Aluminium	Polymeric	Fixed
161	#2	High	Polyurethane	Aluminium	Polymeric	Fixed
162	#3	High	Polyurethane	Aluminium	Polymeric	Fixed
163	#1	Low	Aluminium	Steel	Polymeric	Fixed
164	#2	Low	Aluminium	Steel	Polymeric	Fixed
165	#3	Low	Aluminium	Steel	Polymeric	Fixed
166	#1	High	Aluminium	Steel	Polymeric	Fixed

Standard order (Filename)	Impact Position	Hammer Speed	Hammer Tip	Anvil Plate	Anvil Insulator	Boundary Conditions
167	#2	High	Aluminium	Steel	Polymeric	Fixed
168	#3	High	Aluminium	Steel	Polymeric	Fixed
169	#1	Low	Delrin	Steel	Polymeric	Fixed
170	#2	Low	Delrin	Steel	Polymeric	Fixed
171	#3	Low	Delrin	Steel	Polymeric	Fixed
172	#1	High	Delrin	Steel	Polymeric	Fixed
173	#2	High	Delrin	Steel	Polymeric	Fixed
174	#3	High	Delrin	Steel	Polymeric	Fixed
175	#1	Low	Polyurethane	Steel	Polymeric	Fixed
176	#2	Low	Polyurethane	Steel	Polymeric	Fixed
177	#3	Low	Polyurethane	Steel	Polymeric	Fixed
178	#1	High	Polyurethane	Steel	Polymeric	Fixed
179	#2	High	Polyurethane	Steel	Polymeric	Fixed
180	#3	High	Polyurethane	Steel	Polymeric	Fixed

References

[1] J.-R. Lee, C.C. Chia, C.-W. Kong, Review of pyroshock wave measurement and simulation for space systems, Measurement 45 (2012) 631–642. https://doi.org/10.1016/j.measurement.2011.12.011.

[2] N.T. Davie, V.I. Bateman, Pyroshock simulation for satellite components using a tunable resonant fixture, phase 1, NASA STIRecon Tech. Rep. N 93 (1992) 22975.

[3] N.T. Davie, V.I. Bateman, Pyroshock simulation for satellite components using a tunable resonant fixture-phase 2, Sandia National Labs., Albuquerque, NM (United States), 1997.

[4] A. Calvi, G. Aglietti, J. Albus, M. Bellini, D. Burtin, E. Cavro, J. Dupré, C. Fabriés, S. Fransen, D. Gangloff, A. Girard, N. Gualtieri, A. Itta, G. Kerschen, W. Konrad, R. Morisset, P. Nali, A. Newerla, G. Quagliotti, A. Rittweger, N. Roy, G. Sinnema, R. Ullio, J. Vergniaud, R. Veul, J. Wijker, ECSS-E-HB-32-26A Spacecraft Mechanical Loads Analysis Handbook, Undefined (2013).

[5] H. Himelblau, J.E. Manning, D.L. Kern, A.G. Piersol, S. Rubin, Dynamic environmental criteria, NASA Tech. Handb. 7005 (2001) 249.

[6] MIL-STD-810F, Dep. Def. Test Method Stand. Environ. Eng. Consid. Lab. Tests Version F US Gov. Print. Off. (2000).

[7] A.P. One, Pyroshock Testing Techniques, (2009).

[8] H. Himelblau, Pyroshock Test Criteria, NASA-STD-7003A, 2011.

[9] J.E. Alexander, Shock response spectrum-a primer, Sound Vib. 43 (2009) 6–15.

[10] C. Sisemore, Defining Resonant Plate Shock Test Specifications in the Time Domain., Sandia National Lab.(SNL-NM), Albuquerque, NM (United States), 2019.

[11] E.S.A. ECSSSecretariat, R. ESTEC, ECSS-E-ST-10-03C, Space Eng.-Test. ESA Publ. Div. Noordwijk Neth. (2012).

[12] ECSS-E-HB-32-25A, Space engineering, Mech. Shock Des. Verification Handb. (2015).

[13] ISO 18431-4:2007(en), Mechanical vibration and shock — Signal processing — Part 4: Shock-response spectrum analysis, (n.d.). https://www.iso.org/obp/ui/#iso:std:iso:18431:-4:ed-1:v1:en (accessed December 12, 2022).

[14] S.D. Stearns, D.R. Hush, Digital signal processing with examples in MATLAB, CRC Press, 2016. https://books.google.com/books?hl=it&lr=&id=AWXRBQAAQBAJ&oi=fnd&pg=PP1&dq=stearns+digital+signal+processing+with&ots=8MyYMejb5Z&sig=3MiwT-vajs2WKlYY_0V1_EpH7N_c (accessed March 3, 2024).

[15] D.O. Smallwood, An improved recursive formula for calculating shock response spectra, Shock Vib. Bull. 51 (1981) 211–217.

[16] K. Ahlin, Shock response spectrum calculation-an improvement of the smallwood algorithm, in: 70th Shock Vib. Symp., SAVIAC, 1999.

[17] K. Ahlin, On the use of digital filters for mechanical system simulation, in: Proc Shock Vib. Symp., 2003.

[18] K. Ahlin, M. Magnevall, A. Josefsson, Simulation of forced response in linear and nonlinear mechanical systems using digital filters, in: Int. Conf. Noise Vib. Eng. ISMA2006, KATHOLIEKE UNIV LEUVEN, DEPT WERKTUIGKUNDE, 2006. https://www.diva-portal.org/smash/record.jsf?pid=diva2:835808 (accessed March 3, 2024).

[19] J. Tuma, M. Babiuch, P. Koci, Calculation of a shock response spectra, Acta Montan. Slovaca 16 (2011) 66.

[20] S.D. Stearns, Digital Signal Analysis, Hayden Book Company, Inc Rochelle Park NJ (1975).

[21] D.O. Smallwood, Improved recursive formula for calculating shock response spectra, Sandia National Labs., Albuquerque, NM (USA), 1980.

[22] R.D. Kelly, G. Richman, Principles and techniques of shock data analysis, MEASUREMENT ANALYSIS CORP LOS ANGELES CA, 1969.

[23] L. Viale, A.P. Daga, L. Garibaldi, A. Fasana, Numerical Modeling of a Pyroshock Test Plate for Qualification of Space Equipment, in: P. Rizzo, A. Milazzo (Eds.), Eur. Workshop Struct. Health Monit., Springer International Publishing, Cham, 2023: pp. 990–999. https://doi.org/10.1007/978-3-031-07322-9_100.

[24] A.P. Daga, L. Viale, L. Garibaldi, A. Fasana, S. Marchesiello, Frequency domain convolutional model of a pyroshock plate for qualification of space equipment, AIP Conf. Proc. 2872 (2023) 120011. https://doi.org/10.1063/5.0164212.

[25] L. Viale, A.P. Daga, A. Fasana, L. Garibaldi, On pyroshock tests for aerospace equipment qualification: A comprehensive parametric model for the simulation and the design of pyroshock test facilities, Int. J. Impact Eng. 180 (2023) 104697. https://doi.org/10.1016/j.ijimpeng.2023.104697.

[26] L. Viale, A.P. Daga, L. Garibaldi, Design of a Resonant Plate for Pyroshock Testing based on Shape and Size Heuristic Optimization, Survishno 2023 Conf. Proc. (2023).

[27] A.P. Daga, L. Viale, A. Fasana, Optimization of the Energy Input and Output Parameters for Pyroshock Testing, Survishno 2023 Conf. Proc. (2023).

[28] S.H. Abbas, J.-R. Lee, J.-K. Jang, Z. Kim, FPGA-based multipoint shock wave measurement system using LDVs for aerospace applications, in: 2016 IEEE Aerosp. Conf., IEEE, 2016: pp. 1–6. https://ieeexplore.ieee.org/abstract/document/7500864/?casa_token=it2vwEOh0GMAAAAA:zmImwG0Qq4OmpyhAeFgXGynZfiQHjrF6WaO6gn1JnMjmLXhb1eeQOZmzHAX2nIaLitXqjAj (accessed January 3, 2024).

[29] M. Choi, Experimental prediction of shock response spectra of point-wise explosive pyroshock in a space launcher composite structure using laser pulse excitation and in-line filtering, SAE Int. J. Aerosp. 6 (2013) 65–69.

[30] D. Dilhan, A. Piquereau, L. Bonnes, J. Van de Veire, Definition and manufacturing of the pyroshock bench, in: 7th ESACNES Int. Workshop Space Pyrotech. ESTEC, 2008.

[31] A. García-Pérez, A. Ravanbakhsh, F. Sorribes-Palmer, G. Alonso, Structural shock verification by numerical analysis of the EPD payload units on board Solar Orbiter spacecraft, Acta Astronaut. 168 (2020) 282–292.

[32] M. Gherlone, D. Lomario, M. Mattone, R. Ruotolo, Application of wave propagation to pyroshock analysis, Shock Vib. 11 (2004) 145–156.

[33] B. Houshmand, A. Lacher, N. Juengel, L. Prasol, U. Von Wagner, E. Uhlmann, A novel excitation method for pyroshock simulation, J. Vib. Control 22 (2016) 4247–4258. https://doi.org/10.1177/1077546315573904.

[34] J.H.-J. Hwang, A. Duran, Stochastic shock response spectrum decomposition method based on probabilistic definitions of temporal peak acceleration, spectral energy, and phase lag distributions of mechanical impact pyrotechnic shock test data, Mech. Syst. Signal Process. 76 (2016) 424–440.

[35] M. Iadevaia, B. Van Hal, J.L. Riobbo, P. Sas, Using statistical energy analysis for shock pulse predictions, in: Proc. ISMA, Citeseer, 2002: p. 2342. https://citeseerx.ist.psu.edu/document?repid=rep1&type=pdf&doi=499a983d0c3afc8e84af03e1675303480b184732 (accessed January 3, 2024).

[36] T. Iwasa, Q. Shi, Simplified Analysis Model for Predicting Pyroshock Responses on Composite Panel, J. Space Eng. 1 (2008) 79–90.

[37] J. Jeong, K. Kim, J. Lee, Development of a point pyroshock source simulator, Shock Vib. 2017 (2017).

[38] B.-S. Kim, J. Lee, Development of Impact Test Device for Pyroshock Simulation Using Impact Analysis, Aerospace 9 (2022) 407.

[39] S. Kiryenko, G. Piret, J. Kasper, ESA/ESTEC shock bench presentation, in: Spacecr. Struct. Mater. Mech. Test. 2005, 2005.

[40] A. Lacher, N. Jüngel, U. von Wagner, A. Bäger, Analytical calculation of in-plane response of plates with concentrated masses to impact and application to pyroshock simulation, J. Sound Vib. 331 (2012) 3358–3370.

[41] J.-R. Lee, J.-K. Jang, M. Choi, C.-W. Kong, Visualization and simulation of a linear explosive-induced pyroshock wave using Q-switched laser and phased array transducers in a space launcher composite structure, Opt. Laser Technol. 67 (2015) 12–19.

[42] B. Li, Q. Li, B. Liu, Z. Niu, Z. Nangong, C. Zhao, Critical shock response spectrum of a beam under shock loading, in: Int. Conf. Offshore Mech. Arct. Eng., American Society of Mechanical Engineers, 2016: p. V009T12A019. https://asmedigitalcollection.asme.org/OMAE/proceedings-abstract/OMAE2016/V009T12A019/280559?casa_token=LBtaXrrsVn4AAAAA:dbcbeqc4HWpZjtiSeEEf2RDOJL3Tngb651YE3lt2SDIat6HCZ_yPKnthujzd1j7kR4RMY7Q (accessed January 3, 2024).

[43] X. Lu, K. Jiang, S. Cheng, D. Su, H. Wang, Prediction and isolation of pyroshock in typical pyrotechnic device based on coupled modeling technique, Thin-Walled Struct. 177 (2022) 109393.

[44] V. Mittal, M. Patnaik, S. Narayan, D. Premkumar, Development of Pyroshock Simulation Device (PSSD) for spacecraft application, J Spacecr. Technol 29 (2018) 11–18.

[45] R. Monti, P. Gasbarri, Dynamic load synthesis for shock numerical simulation in space structure design, Acta Astronaut. 137 (2017) 222–231.

[46] O.M.F. Morais, C.M.A. Vasques, Shock environment design for space equipment testing, Proc. Inst. Mech. Eng. Part G J. Aerosp. Eng. 231 (2017) 1154–1167.

[47] M. Remedia, G. Aglietti, M. Appolloni, A. Cozzani, A. Kiley, Virtual testing: a pre-and post-test tool for base-driven spacecraft testing, in: Aerosp. Test. Semin., 2017. https://www.researchgate.net/profile/Marcello-Remedia/publication/317560496_Virtual_Testing_A_Pre-_and_Post-Test_Tool_for_Base-Driven_Spacecraft_Testing/links/5b6318e2458515298ce0a889/Virtual-Testing-A-Pre-and-Post-Test-Tool-for-Base-Driven-Spacecraft-Testing.pdf (accessed January 3, 2024).

[48] Y. Sadkin, Spacecraft Quasi-Static Test Performed on a Shaker, in: Environ. Test. Space Programme, 2004: pp. 203–208. https://adsabs.harvard.edu/full/2004ESASP.558..203S (accessed January 3, 2024).

[49] P. Seefeldt, T. Spröwitz, J.T. Grundmann, E. Ksenik, E. Mikulz, S. Reershemius, K. Sasaki, M. Sznajder, Special Testing and Test Strategies for Unique Space Hardware Developments, in: Proc. Int. Astronaut. Congr. IAC, 2018. https://elib.dlr.de/127438/ (accessed January 3, 2024).

[50] M. Sutra, D. Mesnier, A. Berlioz, B. Combes, Development of a simulation process of the behaviour of space equipment subjected to pyrotechnic shocks, based on characterization and environmental tests, in: Spacecr. Struct. Mater. Mech. Test. 2005, 2005. https://adsabs.harvard.edu/full/2005ESASP.581E.126S (accessed January 3, 2024).

[51] X. Wang, W. Liu, X. Li, Y. Sun, The Shock Response Prediction of Spacecraft Structure Based on Hybrid FE-SEA Method, Appl. Sci. 11 (2021) 8490.

[52] X. Wang, W. Liu, J. Ding, Y. Sun, Y. Dang, Pyroshock Response Prediction of Spacecraft Structure in Wide Frequency Domain Based on Acceleration FRF, Aerospace 9 (2022) 54.

[53] D. Wattiaux, O. Verlinden, C. Conti, C. De Fruytier, Prediction of the vibration levels generated by pyrotechnic shocks using an approach by equivalent mechanical shock, (2008). https://asmedigitalcollection.asme.org/vibrationacoustics/article-abstract/130/4/041012/439248?casa_token=9zTkuq4_Rk0AAAAA:87wccCAev_vSDv-zoIKdmbzvmOcAwf6jp1VKzGIjrX2BOULWOJ8zMk7TKom8jRABwNI-HuojA (accessed January 3, 2024).

[54] T. Yalçinkaya, B. Gürsoy, Numerical Validation of a Pyroshock Test System and Application to Qualification Tests, Aerospace 9 (2022) 400. https://doi.org/10.3390/aerospace9080400.

[55] Z. Hongda, D. Jifeng, L.I.U. Wei, H.A.O. Zhiwei, S.U.N. Yi, Q. Zhang, L.I.U. Yizhi, Simulator of pyroshock environment and effect rules of its adjustable parameters, Chin. J. Aeronaut. 33 (2020) 609–620.

[56] C. Sisemore, M.A. Spletzer, Design of a Resonant Plate Shock Fixture to Attenuate Excessive High-Frequency Energy Inputs., Sandia National Lab.(SNL-NM), Albuquerque, NM (United States), 2017.

[57] J.M. McGlaun, S.L. Thompson, M.G. Elrick, CTH: A three-dimensional shock wave physics code, Int. J. Impact Eng. 10 (1990) 351–360.

[58] M. Jonsson, Development of a shock test facility for qualification of space equipment, Dep. Appl. Mech. Göteb. Swed. (2012).

[59] C. Qian, Simulation of Mechanical Shock with Finite Element Analysis and Estimation of Shock Attenuation, (2021).

[60] A.İ. Küçükbayram, Analysis and verification of a pyroshock test system, Master's Thesis, Middle East Technical University, 2021. https://open.metu.edu.tr/handle/11511/89644 (accessed January 3, 2024).

[61] N. Siam, Development of an efficient analysis method for prediction and structural dimensioning of space structures subjected to shock loading, (2010). https://www.diva-portal.org/smash/record.jsf?pid=diva2:1023156 (accessed January 3, 2024).

[62] E. Gomez, Dynamic Response Predictions of Structures Subjected to Pyroshock Excitation, KTH Royal Institute of Technology, 2005.

[63] E. Dalton, B. Chambers, I.I. Chambers, Analysis and validation testing of impulsive load response in complex, multi-compartmented structures, in: 36th Struct. Struct. Dyn. Mater. Conf., 1995: p. 1243.

[64] B. Troclet, B. Hiverniau, M.N. Ichchou, L. Jezequel, K. Kayvantash, T. Bekkour, J.B. Mouillet, A. Gallet, FEM/SEA hybrid method for predicting mid and high frequency structure-borne transmission, Open Acoust. J. 2 (2009). https://benthamopen.com/ABSTRACT/TOACOJ-2-45 (accessed January 3, 2024).

[65] R. Ullio, P.C. Marucchi-Chierro, A. Spazio, Utilization of prediction methods in the shock environment evaluation, in: Spacecr. Struct. Mater. Mech. Test., 2001: p. 239.

[66] D.-O. Lee, J.-H. Han, H.-W. Jang, S.-H. Woo, K.-W. Kim, Shock response prediction of a low altitude earth observation satellite during launch vehicle separation, Int. J. Aeronaut. Space Sci. 11 (2010) 49–57.

[67] J. Liu, L. Yang, X. Zhang, R. Yan, X. Chen, Intelligent time-domain parameters matching for shock response spectrum and its experimental validation in active vibration control systems, Shock Vib. 2019 (2019) 1–16.

[68] R.J. Pinnington, D. Lednik, Transient statistical energy analysis of an impulsively excited two oscillator system, J. Sound Vib. 189 (1996) 249–264.

[69] B.Y. Mao, S.L. Xie, M.L. Xu, X.N. Zhang, G.H. Zhang, Simulated and experimental studies on identification of impact load with the transient statistical energy analysis method, Mech. Syst. Signal Process. 46 (2014) 307–324.

[70] A. García-Pérez, F. Sorribes-Palmer, G. Alonso, A. Ravanbakhsh, Overview and application of FEM methods for shock analysis in space instruments, Aerosp. Sci. Technol. 80 (2018) 572–586.

[71] A.E.H. Love, A treatise on the mathematical theory of elasticity, Dover Publications, N. Y. 1 (1944).

[72] L.D. Landau, E. Lifshitz, Course of theoretical physics, n.d.

[73] B. Leroy, Collision between two balls accompanied by deformation: a qualitative approach to Hertz's theory, Am. J. Phys. 53 (1985) 346–349.

[74] D. Gugan, Inelastic collision and the Hertz theory of impact, Am. J. Phys. 68 (2000) 920–924.

[75] H. Ghaednia, X. Wang, S. Saha, Y. Xu, A. Sharma, R.L. Jackson, A review of elastic–plastic contact mechanics, Appl. Mech. Rev. 69 (2017) 060804.

[76] A.D. Kerr, Elastic and viscoelastic foundation models, (1964). https://asmedigitalcollection.asme.org/appliedmechanics/article-abstract/31/3/491/386992 (accessed January 6, 2024).

[77] D. Younesian, A. Hosseinkhani, H. Askari, E. Esmailzadeh, Elastic and viscoelastic foundations: a review on linear and nonlinear vibration modeling and applications, Nonlinear Dyn. 97 (2019) 853–895.

[78] E. Winkler, Die Lehre von der Elasticitaet und Festigkeit: mit besonderer Rücksicht auf ihre Anwendung in der Technik, für polytechnische Schulen, Bauakademien, Ingenieure, Maschinenbauer, Architecten, etc, H. Dominicus, 1867. https://books.google.com/books?hl=it&lr=&id=i2kSAAAAIAAJ&oi=fnd&pg=PR1&dq=Winkler,+E.:+Die+Lehre+von+der+Elasticitaet+und+Festigkei.+Prag,+Dominicus+(1867)&ots=GaOjS0-lP1&sig=nQOZU_GgtLkA__scyQLDm0UnQG0 (accessed January 6, 2024).

[79] M.M. Filonenko-Borodich, Some approximate theories of elastic foundation, Uchenyie Zap. Mosk. Gos. Univ. Mekhanika 46 (1940) 3.

[80] M. Hetenyi, A general solution for the bending of beams on an elastic foundation of arbitrary continuity, J. Appl. Phys. 21 (1950) 55–58.

[81] P.L. Pasternak, On a new method of analysis of an elastic foundation by means of two foundation constants, Gos Izd Lit Po Strait Arkh (1954). https://cir.nii.ac.jp/crid/1573950399307292288 (accessed January 6, 2024).

[82] W. Flügge, Viscoelasticity; Blaisdell Publ, Co Walth. Mass USA (1967) 127.

[83] K.H. Hunt, F.R.E. Crossley, Coefficient of restitution interpreted as damping in vibroimpact, (1975). https://asmedigitalcollection.asme.org/appliedmechanics/article-abstract/42/2/440/387758 (accessed January 6, 2024).

[84] W.J. Stronge, Unraveling paradoxical theories for rigid body collisions, (1991). https://asmedigitalcollection.asme.org/appliedmechanics/article-abstract/58/4/1049/423404 (accessed January 8, 2024).

[85] C. Zener, The intrinsic inelasticity of large plates, Phys. Rev. 59 (1941) 669.

[86] G. Weir, S. Tallon, The coefficient of restitution for normal incident, low velocity particle impacts, Chem. Eng. Sci. 60 (2005) 3637–3647.

[87] C.M. Harris, A.G. Piersol, Harris' shock and vibration handbook, McGraw-Hill New York, 2002.

[88] S. Timoshenko, S. Woinowsky-Krieger, Theory of plates and shells, McGraw-hill New York, 1959. https://cds.cern.ch/record/102847/files/0070858209_TOC.pdf (accessed March 3, 2024).

[89] Ö. Yilmaz, Seismic Data Analysis: Processing, Inversion, and Interpretation of Seismic Data, Society of Exploration Geophysicists, 2001. https://doi.org/10.1190/1.9781560801580.

[90] A. Fasana, Modal parameters estimation in the Z-domain, Mech. Syst. Signal Process. 23 (2009) 217–225.

[91] N.M.M. Maia, J.M.M. e Silva, Theoretical and experimental modal analysis, Research Studies Press, 1997.

[92] S.W. Smith, The scientist and engineer's guide to digital signal processing, (1997). http://www.dspguide.com/CH28.PDF (accessed October 17, 2023).

[93] V. Giovanni, A. Fasana, Identification of Modal Parameters in Frequency Domain with Emphasis on Output Only Cross-Spectral Density Functions, SAE Trans. (2007) 1959–1965.

[94] A. Fasana, S. Marchesiello, Meccanica delle vibrazioni, Clut, 2006.

[95] J.O. Smith III, Spectral audio signal processing, No Title (2011). https://cir.nii.ac.jp/crid/1130282272703449216 (accessed March 1, 2024).

[96] K. PAVEL, S. David, G. Ruiz, J.A. Michell, Design and Architecture is for Digital Signal Processing, (2013).

[97] L. Meirovitch, Principles and techniques of vibrations, No Title (1997). https://cir.nii.ac.jp/crid/1130000797075151232 (accessed February 29, 2024).

[98] OpenSCAD, (n.d.). https://openscad.org (accessed July 22, 2022).

[99] D. Patil, C. Fred Higgs, Experimental investigations on the coefficient of restitution for sphere–thin plate elastoplastic impact, J. Tribol. 140 (2018) 011406.

[100] H. Li, W. Chen, H. Hao, Factors influencing impact force profile and measurement accuracy in drop weight impact tests, Int. J. Impact Eng. 145 (2020) 103688. https://doi.org/10.1016/j.ijimpeng.2020.103688.

[101] P. Peng, C. Di, L. Qian, G. Chen, Parameter identification and experimental investigation of sphere-plane contact impact dynamics, Exp. Tech. 41 (2017) 547–555.

[102] K.-Y. Ahn, B.-J. Ryu, A modeling of impact dynamics and its application to impact force prediction, J. Mech. Sci. Technol. 19 (2005) 422–428.

[103] D. Chicco, M.J. Warrens, G. Jurman, The coefficient of determination R-squared is more informative than SMAPE, MAE, MAPE, MSE and RMSE in regression analysis evaluation, PeerJ Comput. Sci. 7 (2021) e623.

[104] C.J. Willmott, K. Matsuura, Advantages of the mean absolute error (MAE) over the root mean square error (RMSE) in assessing average model performance, Clim. Res. 30 (2005) 79–82.

[105] D. Whitley, A genetic algorithm tutorial, Stat. Comput. 4 (1994) 65–85.

[106] Stanford University and California Polytechnic Institute, CubeSat Design Specifications Document, Revision 14, (2020). https://static1.squarespace.com/static/5418c831e4b0fa4ecac1bacd/t/5f24997b6deea10cc52bb016/1596234122437/CDS+REV14+2020-07-31+DRAFT.pdf.

[107] S.G.P. Castro, Impact hammer test of an Aluminium 6082 T6 plate, 260 x 246 x 1.5 mm, free boundary conditions, (2022). https://doi.org/10.5281/zenodo.6813857.

[108] L. Viale, G. Tibert, A Full Factorial Open-Access Dataset for Aerospace Shock Testing, (2024). https://doi.org/10.5281/zenodo.10371545.

[109] J. Antony, Design of experiments for engineers and scientists, Elsevier, 2014.

[110] M.J. Anderson, P.J. Whitcomb, DOE simplified: practical tools for effective experimentation, CRC press, 2017.

[111] L. Viale, A.P. Daga, L. Garibaldi, S. Caronia, I. Ronchi, Books Trimmer Industrial Machine Knives Diagnosis: A Condition-Based Maintenance Strategy Through Vibration Monitoring via Novelty Detection, in: American Society of Mechanical Engineers Digital Collection, 2023. https://doi.org/10.1115/IMECE2022-94547.

[112] V. Czitrom, One-Factor-at-a-Time versus Designed Experiments, Am. Stat. 53 (1999) 126–131. https://doi.org/10.1080/00031305.1999.10474445.

[113] K.-J. Bathe, Finite element procedures, Klaus-Jurgen Bathe, 2006.

[114] M. Ahmad, K.A. Ismail, F. Mat, Impact models and coefficient of restitution: A review, ARPN J Eng Appl Sci 11 (2016) 6549–6555.

[115] L. Caligaris, S. Fava, C. Tomasello, Manuale di meccanica: matematica, antinfortunistica e impatto ambientale, fisica tecnica, chimica, disegno e tecniche di progettazione, tecnologia dei materiali, tecnologia meccanica, meccanica, costruzione di macchine, meccanica dell'auto, elettrotecnica ed elettronica, sistemi automatici, controllo e regolazione automatica, sensori e trasduttori, robotica industriale, termotecnica, macchine a fluido e impiani, organizzazione industriale, manutenzione, Hoepli, 2016.

[116] CNR UNI 10011:1988 - UNI Ente Italiano di Normazione, (n.d.). https://store.uni.com/en/cnr-uni-10011-1988 (accessed February 21, 2024).

[117] UNI EN 1993-1-1:2022 - UNI Ente Italiano di Normazione, (n.d.). https://store.uni.com/uni-en-1993-1-1-2022 (accessed February 19, 2024).

[118] UNI EN 1993-1-8:2005 - UNI Ente Italiano di Normazione, (n.d.). https://store.uni.com/uni-en-1993-1-8-2005 (accessed February 19, 2024).

[119] La progettazione dei sistemi di ancoraggio Wuerth, (n.d.). https://fs.wuerth.it/media/downloads/pdf/brochure_1/tasselli_ancoranti/la_progettazione_dei_sistemi_di_ancoraggio_wuerth.pdf (accessed February 27, 2024).

[120] M. Denny, The internal ballistics of an air gun, Phys. Teach. 49 (2011) 81–83.

[121] Z.J. Rohrbach, T.R. Buresh, M.J. Madsen, Modeling the exit velocity of a compressed air cannon, Am. J. Phys. 80 (2012) 24–26.

[122] T. Raparelli, V. Viktorov, F. Colombo, L. Lentini, Aerostatic thrust bearings active compensation: Critical review, Precis. Eng. 44 (2016) 1–12.

[123] ISO 6358-2:2019(en), Pneumatic fluid power — Determination of flow-rate characteristics of components using compressible fluids — Part 2: Alternative test methods, (n.d.). https://www.iso.org/obp/ui/#iso:std:iso:6358:-2:ed-2:v1:en (accessed February 18, 2024).

[124] UNI EN 10305-4:2016 - UNI Ente Italiano di Normazione, (n.d.). https://store.uni.com/uni-en-10305-4-2016 (accessed February 19, 2024).